ABSTRACT

Chemical Kinetics and Dynamics of M^+(organic) Molecules Using Single Photon Initiated Dissociative Rearrangement Reactions (SPIDRR) Measurements

Zachry C. Theis, Ph.D.

Mentor: Darrin J. Bellert, Ph.D.

Gas-phase studies are important to many areas of science and technology. The ability to prepare molecular species in an environment devoid of complexities present in the condensed phase allows for high resolution measurement of molecular level details. This is particularly important when studying ion-molecule reactions where transition metals are involved. The open-shell, radical nature of the transition metal in combination with its charge promotes a host of low-energy chemical transformations with multiple reactive pathways open within a few eV of the zero point level of the encounter complex ground state. Moreover, barriers along these pathways are often submerged with respect to the separated reactant limit making both temporal and energetically resolved kinetic measurement challenging. However, it is precisely these qualities of a transition metal cation (a chemically reactive center that mediates low energy chemical transformations) that make it a desired catalytic active site and thus demands high resolution study. To this end, the single photon initiated dissociative rearrangement reaction (SPIDRR) technique was developed. This dissertation details the use of this novel tool toward measurement of

the kinetics and dynamics of the Ni^+ and Co^+ mediated decomposition of several organic molecules.

Ab initio quantum chemical calculations were performed to compliment these experimental studies. The potential energy surface has been determined at the DFT level to suggest the mechanistic features that occur during the metal mediated decomposition of an organic molecule. The combination of experiment and theory has permitted a far deeper understanding of the reaction dynamics and has proven integral towards explaining experimental observation. For example, emerging concepts that guide hydrogen transfers on Ni^+ centered catalytic reactions have evolved from this synergistic combination.

Chemical Kinetics and Dynamics of M^+(organic) Molecules Using Single Photon Initiated Dissociative Rearrangement Reaction (SPIDRR) Measurements

by

Zachry C Theis, B.S.

A Dissertation

Approved by the Department of Chemistry and Biochemistry

_____

Patrick J. Farmer, Ph.D., Chairperson

Submitted to the Graduate Faculty of
Baylor University in Partial Fulfillment of the
Requirements for the Degree
of

Doctor of Philosophy

Approved by the Dissertation Committee

_____

Darrin J. Bellert, Ph.D., Chairperson

_____

Carlos Manzanares, Ph.D.

_____

Kevin Shuford, Ph.D.

_____

Touradj Solouki, Ph.D.

_____

Zhenrong Zhang, Ph.D.

Accepted by the Graduate School

August 2018

_____

J. Larry Lyon, Ph.D., Dean

Page bearing signatures is kept on file in the Graduate School.

TABLE OF CONTENTS

LIST OF FIGURES

ACKNOWLEDGMENTS

I would like to thank the members of my committee Dr. Carlos Manzanares, Dr. Kevin Shuford, Dr. Touradj Solouki and Dr. Zhenrong Zhang for their time, energy and encouraging thoughts. This could not have been achieved without my lab mates and colleagues. Tucker, thank you for steadfast optimism in the last year of my graduate career. Paul, I could not have asked for a better day one friend for this long and adventurous journey. Michael, I will never have the words to adequately describe what our relationship has meant to me in the last four years. Thank you. Finally, I thank my mentor and friend Darrin J. Bellert, Ph.D. Without you none of this would have been possible. I seek to represent you well in the next step of my journey.

To my mother and father

ATTRIBUTIONS

The work detailed in Chapter Four has been entirely reproduced from a publication by multiple authors with the permission of The American Chemical Society journal, Organometallics. As such it is appropriate to detail the contribution of each co-author. The author of this dissertation (Zachry Theis) contributed to the collection of experimental data, kinetic analysis of the SPIDDR kinetic waveforms, the identification of stationary points along the ground state potential energy surfaces, and writing of the manuscript. Carlos Silva López and Olalla Nieto Faza calculated single point energy corrections, the bonding analysis for presented in Figure 4.5, vertical excitation energies for the potential energy surface and contributed to writing the manuscript. Darrin J. Bellert assisted in the kinetic analysis of SPIDRR kinetic waveforms and writing of the manuscript. Adam Mansell contributed to the experimental data collection.

CHAPTER ONE

Introduction

Motivation for Studies

The use of catalysts for chemical transformation contributes greatly to the production of manufactured goods.[1] Wide spread use of transition metal species in catalytic processes has prompted numerous investigations which seek mechanistic understanding of catalytic transformations in organometallic reactions.[2-6] Despite many targeted efforts, tunable catalysts for even basic processes such as activation of small alkanes remain elusive. Over the last thirty years however, these efforts have taken advantage of improvements in experimental physical techniques to gain knowledge and insight as to how such processes may occur. Furthermore, a wealth of thermochemical data has been reported which allows greater scrutiny of the computational methods that must often be relied upon to fully understand the nature of metal mediated chemical transformation. A more complete understanding of reaction intermediates and energy requirements of transition states that allow C-C and C-H activation is no doubt an important endeavor if only to exploit naturally abundant chemical feed stocks. Gas phase studies are then an indispensable tool because the gas phase environment reduces the number of variables which must be accounted for when interpreting results.

The preparation of atomic transition metal ion species under high vacuum conditions creates an ideal model to uncover the metal's reactive properties. Ion chemistry is of particular interest based on the experimental control that can be exacted.

Ion dipole interactions also lead to stronger binding energies, which increases the probability (when compared to neutral metal/organic clusters) that reaction barriers exist below the separated reactant limit. Though such idealized systems do not directly correlate with exact mechanistic details of their bulk phase counterparts, the ability to build a conceptual framework in the absence of solvent and counter ion effects is a natural step towards a comprehensive understanding of important organometallic reaction dynamics. The use of metal ions as model systems is further supported when considering that defect sites on surfaces often serve as catalytic active sites.[7]

Finally, the relatively modest size of these idealized systems makes them excellent candidates for rigorous theoretical treatments. An attempt to accurately describe a range of chemical reactions and their properties has resulted in a large variety of computational methods aimed at this task. The economic computational cost of DFT methods alone has given rise to a plethora of functionals which vary in their success to accurately describe nuclear configurations, electronic properties and thermochemical quantities.[8] The transition metal ion chemical reactions described in this dissertation possess only 10-20 nuclei. However, transient bonding that occurs during chemical reactions coupled with open shell electronic configuration of the metal ion make it extremely challenging to confidently assess the accuracy of computational techniques in the absence of experimental benchmarks. Organometallic ion reactions studied in the absence of the condensed phase are the ideal platform to guide continued development of theoretical methods which are ultimately needed to understand the subtleties of chemical reaction dynamics as applied to catalysis.

The many benefits this avenue of research provides has resulted in several techniques specifically used to investigate transition metal ion activation of small organic substrates. Several common examples of these techniques include, ion cyclotron-resonance mass spectrometry (ICR-MS),[9] guided-ion beam tandem mass spectrometry (GIBMS),[10,11] selected ion-flow tube (SIFT),[12-14] and kinetic energy release distribution (KERD).[6] GIBMS has made significant contributions to the wealth of thermochemical data available on transition metal ion reactions. GIBMS is capable of inducing well controlled collisions with reactant molecules and as such can monitor dissociative reactions over a wide energy range. The resultant collisional energy cross section can then be used to extract thermochemical properties for the interrogated dissociative reaction. This method relies on the conversion of kinetic energy to internal energy through collision and extrapolation to a zero collisional energy limit. Bimolecular collision methods are ideal for studying endothermic processes, where reaction barriers lie in excess of the separated reactant limit.

Measurement of reaction barriers which exist below the separated reactant limit is challenging and has only been reported using techniques such as state specific activation or metastable decay of activated precursors. Selected-ion flow tube (SIFT) techniques have been successfully employed to make measurements of details of the potential energy surface below the separated reactant limit. However, SIFT is limited to studying thermal systems and the reported kinetics rely on pseudo first order assumptions in addition to extensive kinetic modeling. Kinetic energy release distributions (KERD) have also been used to make measurements of submerged barriers. KERD monitors kinetic energy release of products following metastable decay of a precursor. Phase space theory is often

used to then calculate a KERD that is then matched to the experimental data. This requires a rigorous use of statistical kinetic theory.

The variety of experimental techniques used to examine the kinetics, dynamics and thermochemical properties of gas phase ion mediated chemistry is evidence to the importance of such studies. The novel single photon initiated dissociative rearrangement reaction (SPIDRR) technique seeks to complement existing experimental methods by examining the microcanonical decomposition kinetics of ion molecule species with well-defined internal energies.[15,16] This is achieved through the preparation of supersonically cooled precursors which are activated through photoabsorption using a high-resolution laser. SPIDRR energizes reactants from within the precursor energy well, making it suited for studying submerged reaction barriers. Fragment intensity of the resulting decomposition is then temporally monitored by varying the time at which the precursor is energized. Microcanonical rate limiting rate constants are extracted directly from time dependent decay waveforms.

The ability of SPIDRR to measure microcanonical rate constants at well resolved activating energies (± 250 cm^{-1} for ~15 atom sized systems) allows the assessment of statistical behavior in a reaction. Extracted SPIDRR rate constants are plotted against activating photon energy and compared with RRKM predictions. In the case that RRKM agrees with experimental observation, the activation energy of the reaction can be predicted by extrapolation of the calculated RRKM curve. Furthermore, SPIDRR provides an upper limit to rate limiting barrier energies that can be over-estimated by ab initio calculations. Finally, studies of these species under well controlled conditions may

reveal unique reactivity which may be exploited in the future to guide the development of future reagents and catalysts.

CHAPTER TWO

Methods

Single Photon Initiated Dissociative Rearrangement Reactions

Molecular Beam Apparatus

Single Photon Initiated Dissociative Rearrangement Reaction (SPIDRR) measurements are carried out in a high-vacuum expansion chamber which is coupled to a Wiley-McLaren style time-of-flight mass spectrometer (TOFMS).[17] The expansion chamber consists of a laser vaporization (LaVa) cluster source in which cold precursor fragments are prepared before drifting through a field free region towards the TOFMS.[18] The resultant molecular beam is skimmed twice before entering an orthogonal accelerator (OA). The OA then extracts the ion packet and sends it through a second field free region before it passes through a hemispherical kinetic energy analyzer and strikes a dual chevron microchannel plate detector (MCP). A picture of the apparatus is shown in Figure 2.1.

Specifically, the 120 L expansion chamber is vacuum pumped by a 400 mm diffusion pump at a rate of 10,000 L s^{-1}. The TOFMS consists of two five-way crosses connected by a 1.5 m tube. Each cross is pumped on by a 150 mm cryotrap diffusion pump at a rate of 1915 L s^{-1}. Base pressures for the expansion chamber and TOFMS are 2.0×10^{-7} Torr and 2.0×10^{-8} Torr respectively, while operating pressures are generally an order of magnitude higher.

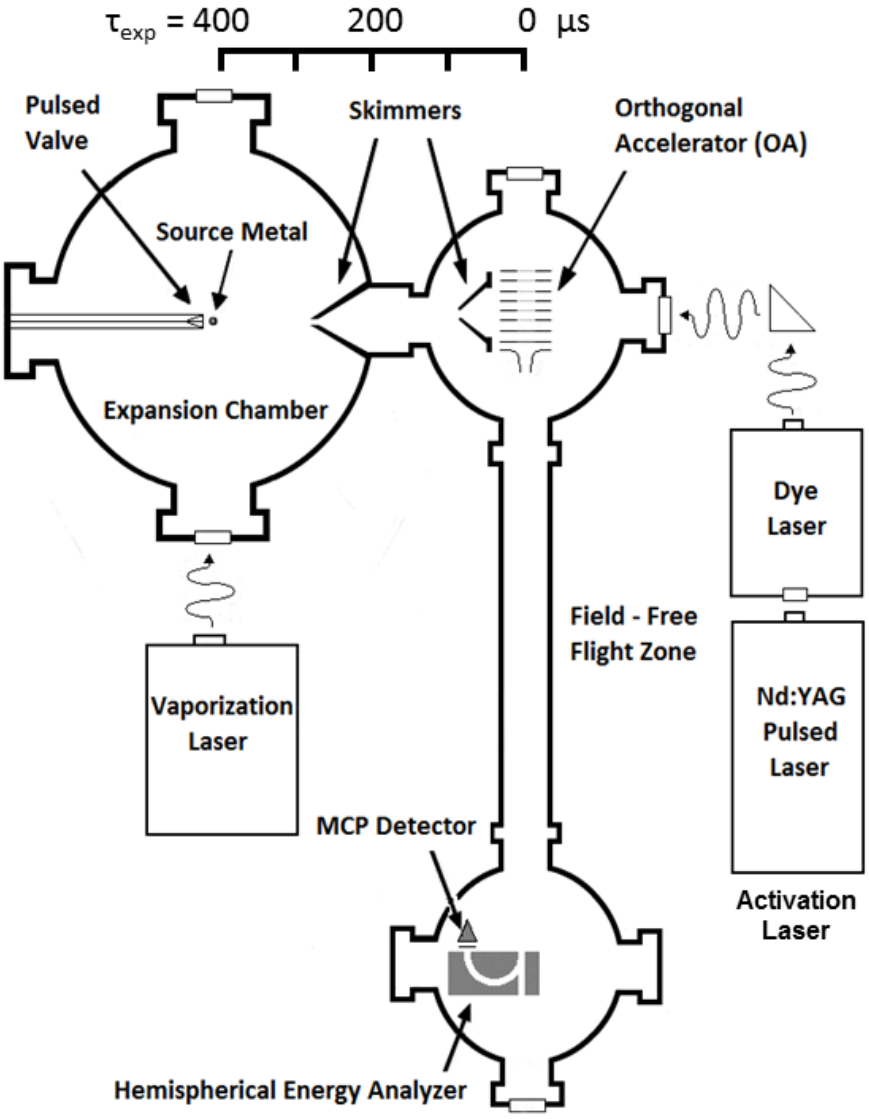

Figure 2.1. A diagram of the instrumental apparatus in which SPIDRR experiments are carried out. The instrument is comprised of a laser vaporization supersonic expansion chamber coupled to a custom time of flight mass spectrometer. At the end of the TOMS is a hemispherical kinetic energy analyzer. Adapted from Ref [19].

A small LaVa style source block is held in place by a flange that mounts on top of the expansion chamber. The source block is designed to accommodate a Parker series 9 pulse valve and a metal source rod such that the vaporization point of a rotating metal rod (~1.2 rpm) is at the center of the chamber. Typically, the radiation for LaVa is supplied

by a pulsed Nd:YAG (532 nm) or a pulsed KrF excimer laser (248 nm) and is focused onto the metal rod. The resultant plume is entrained by a helium carrier gas (~2.5 x 10^3 Torr) doped with the vapor pressure of the desired organic molecule. This results in M^+(organic) precursors which are cooled through collisions in supersonic expansion. The molecular beam then traverses the 79 cm field free expansion region at nearly the terminal velocity of helium (1.77 x 10^3 m s^{-1}) (Mach 70) and passes through two skimmers before entering the acceleration region.

Situated at the entrance to the TOFMS, the accelerator is built from seven parallel capacitor plates with a 2.54 cm central channel for ions to pass through. The first six plates are coupled by 3 kΩ resistors while the final plate is connected through a 13.33 – 20.33 kΩ variable resistor and is also at instrument ground. The molecular beam enters the accelerator stack through the second skimmer. When it reaches the center channel, a 1.75 kV potential is dropped onto the first plate and resistively divided between the remaining plates. Based on the Wiley-McLaren design, this causes high and low field potentials which focus the resultant ion beam onto the plane of the detector. In addition, a 50V deflector plate is used to focus the ions in the direction of expansion.

Ions exiting the OA now have a well-defined kinetic energy corresponding to the 1.75 kV pulse. All particles with the same kinetic energy must travel 1.86 m of field free space and are therefore mass separated before entering the hemispherical sector which transmits based on kinetic energy. Ions which transmit through the sector strike the chevron MCP resulting in a signal that is amplified and recorded on a fast digitizer. The sector is composed of two halves. The potential difference across these halves which allows a fragment to transmit is referred to as the transmission voltage. When the

transmission voltage is tuned to transmit the full kinetic energy of the acceleration event, precursor mass spectra are acquired.

Experimental Trigger Sequence

The following section describes the sequence of triggering events which lead to a single data point in a SPIDRR experiment. Figure 2.2 shows a schematic representation of the instrumental sequence from left to right. The sequence is initiated when a 200 – 300 μs wide pulse is used to open the series 9 valve. The Q-switch trigger pulse for the LaVa source is fired after and timed to optimize the intensity of precursor formation by maximizing overlap of the gas pulse with the metal vapor plume. The delay between the valve and LaVa trigger pulses is generally 300 – 500 μs.

At nearly the terminal velocity of helium, the molecular beam requires 400 μs to travel the field free region before reaching the OA. It is in this 400 μs time that the Q-switch trigger pulse for the activation laser is fired. The activation laser can be triggered at any point along this interval, but if it is fired after the OA, the laser pulse will miss the molecular beam. For this reason, the time component of a SPIDRR experiment, τ, is equal to zero when the trigger pulses for the OA and activation laser are initiated simultaneously. Negative values of τ represent the activation laser being fired prior to the OA trigger pulse. If the activation trigger is fired at $\tau = 0$, the maximum number of decomposing molecules will survive the acceleration event and decompose in the TOFMS. Any fragments that dissociate in the TOFMS will have the same arrival time as the precursor but can be selectively monitored by tuning the transmission voltage to the lower kinetic energy resulting from a mass change following dissociation. The ion travel time through the acceleration grid is defined as α. This is appropriate because any

molecules with a decay lifetime shorter than α will receive the full potential of the OA and will not be sampled. Typical cluster flight times through the TOFMS range from 30 – 50 μs. The final trigger pulse is that of the digital scope to record the arrival of clusters at the detector.

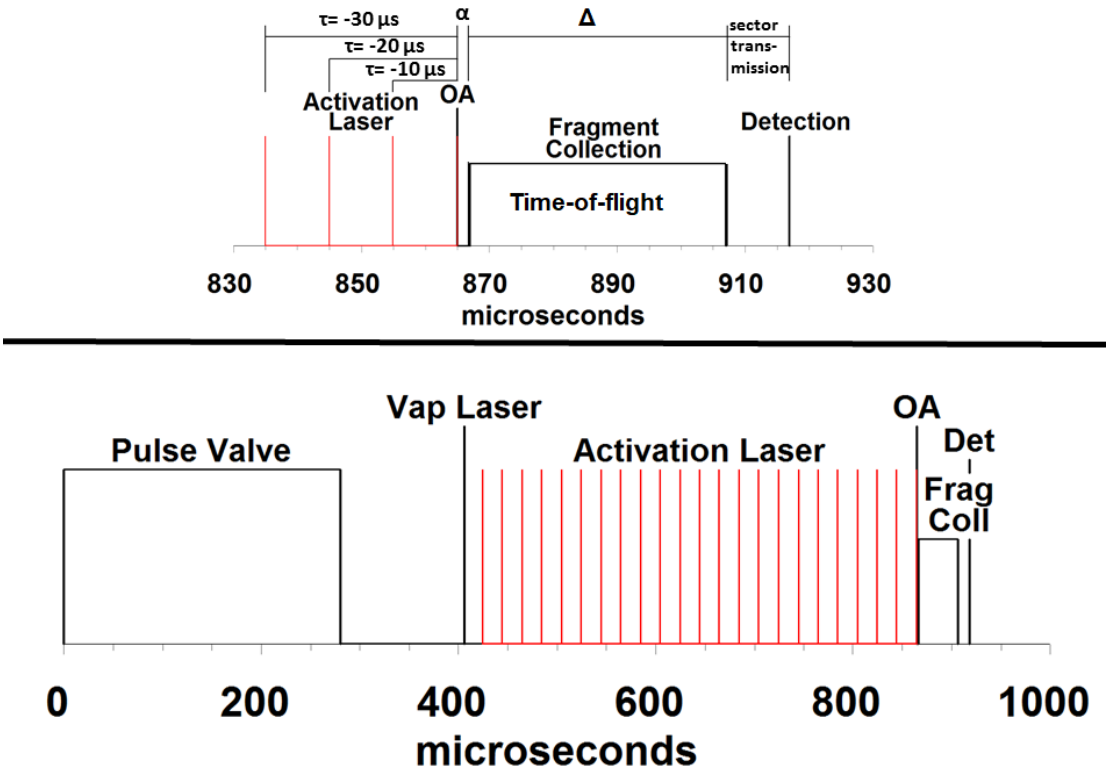

Figure 2.2. The experimental sequence of a SPIDRR experiment. The bottom panel shows a detailed depiction of the photoinitiation event. The red bars in each panel represent the various laser timing delays that result in a single kinetic waveform through the course of a SPIDRR experiment. Adapted from Ref [19].

The described sequence takes approximately 1 ms. In practice, this sequence is repeated 100 or more times and averaged together in real time to yield a single data point corresponding to the intensity of daughter fragment production at $\tau = 0$. A SPIDRR experiment consists of many of these averaged data points at increasingly negative values

of τ. The resultant waveform gives the temporal response of daughter fragment production at a given activating photon wavelength.

Photon Absorption and Unimolecular Decay

Dissociative rearrangement reactions in SPIDRR occur after photon absorption. It should be noted that in all the following studies, the M^+(organic) decomposition is induced using visible light. Typically, ultraviolet radiation is required to induce electronic excitation in organics such as those studied with SPIDRR. Though the electronic structure may be slightly altered upon clustering with the metal, it is not likely that the organic fragment acts as the chromophore. In this case, it must be the low-lying d←d and s←d transitions available to the metal which facilitate the photoabsorption event. These parity forbidden transitions have zero oscillator strength in the bare metal. However, the electrostatically bound organic fragment inductively lowers the electronic symmetry, making the transition weakly allowed. The photoabsorption event leading to rearrangement decomposition is illustrated in Figure 2.3.

If the available energy is greater than insertion and rearrangement barriers without exceeding the adiabatic cluster bond dissociation energy, the molecule will undergo unimolecular decomposition into charged daughter fragments. If a photon in excess of the cluster bond energy is absorbed or if a multiphoton absorption occurs, fast bond cleavage will yield M^+ + (organic). This event likely occurs on the nanosecond timescale and as such will not survive the acceleration event. This prevents multiphoton events from contaminating the observed SPIDRR signal. The energetic limits described above show that SPIDRR is uniquely equipped to assess the reaction kinetics and dynamics of barriers that are submerged with respect to the separated reactant limit.

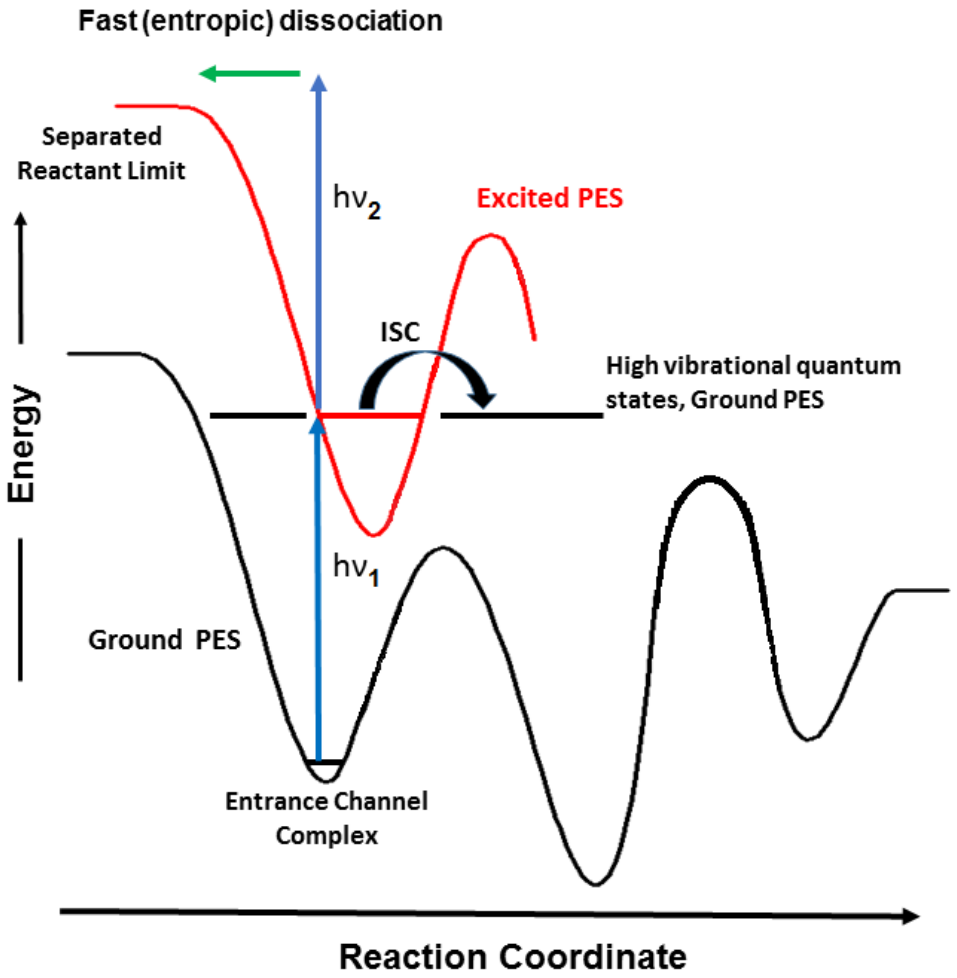

Figure 2.3. A graphical representation of the proposed activation mechanism in SPIDDR. Absorption of a single photon drives the M^+(organic) cluster to an excited state. Intersystem crossing then deposits energy into high vibrational modes of the ground state potential surface. Rearrangement then occurs on the μs timescale. Two photon absorption causes energy absorption in excess of the cluster bond dissociation threshold, causing fast dissociation (ns timescale) which is not observable by SPIDRR. Adapted from Ref [19].

When a precursor molecule absorbs a visible photon from the activation laser, it is promoted to an excited electronic state. Once in this state, it can relax via photon emission or intersystem crossing (ISC). Time-dependent density functional theory calculations predict that ISC occurs on the nanosecond timescale for similar systems.[20] It

is unlikely that photon emission outcompetes this process due to the optical selection rules which result in very weak coupling between the excited and ground state surfaces. It can therefore be concluded that ISC leads to the photon energy being deposited in the high vibrational states of the ground state potential.

This vibrational energy will then randomize through internal vibrational energy redistribution (IVR). Since IVR is much faster than the unimolecular decomposition rate, it is assumed the prepared species are well described by the microcanonical ensemble. Subsequent metal cation insertion and rearrangement occurs on the microsecond timescale and therefore is not subject to competition from blackbody infrared radiation dissociation (BIRD).[21,22] Therefore, the unimolecular decay reactions observed by SPIDRR are controlled by the first order microcanonical rate constant which will be a function of the activating laser photon energy.

Acquisition of SPIDRR Data

Figure 2.4 shows the results of various SPIDRR kinetic experiments. As stated previously, this type of scan is acquired by activating precursor molecules at various points along their flight towards the OA. The maximum intensity signal is generally seen when the activation laser is fired simultaneously with the OA or $\tau = 0$. Once again, positive values of τ indicate the activation laser is fired after the molecular beam has been accelerated and negative values of τ correspond to the activation laser intersecting the molecular beam prior to the acceleration event. SPIDRR waveforms are plotted vs τ and as such appear in negative relative time.

When M+(organic) fragments are fully accelerated before decay, they receive the full 1.75 kV potential of the OA. If they subsequently decay in the field free region of the

TOF however, the mass change from precursor to daughter fragment will result in fragments that have a fraction of the kinetic energy of the precursor but the same arrival time. This allows SPIDRR to discriminate from unactivated precursor molecules by tuning the hemispherical sector. The transmission voltage of the daughter species is given as follows:

$$V_D = V_P \left(\frac{m_D}{m_P}\right)$$

Where V is transmission voltage, m is the mass and the subscripts D and P denote the daughter and precursor respectively. It should be noted that any daughter formation that occurs prior to the acceleration event will not be sampled as the fragment will receive the precursor kinetic energy. Therefore, it will arrive at the detector earlier in time based on mass separation and will only be observed when the sector is set to observe the precursor mass spectrum. The acquisition method of firing the activation laser farther from the OA can be viewed as decreasing the probability of a fragment surviving past the OA. We can then interpret the SPIDRR waveforms as a direct measurement of a precursor lifetime after photoactivation of the cluster. Stated briefly, a SPIDRR waveform is a measure of product fragment intensity resultant from the decay of a photoactivated precursor plotted as a function of the relative timing delay, τ.

To interpret and analyze SPIDRR waveforms, we can relate them to simple unimolecular decay reaction mechanisms. Assuming the waveform is well modeled by a single exponential decay function, we can use the simplest case to develop the functional form of a SPIDRR measurement. For an example, we will consider the mechanism A→B governed by the rate constant k. The integrated rate equations for this mechanism are well known and are as follows:

$$(\mathbf{1}) \quad A(t) = A_0 e^{-kt}$$

$$(\mathbf{2}) \quad B(t) = A_0(1 - e^{-kt})$$

where A(t) represents the number of dissociated precursor molecules at time *t* and B(*t*) is the number of daughter fragments the have been produced at time t. As such, an initial population, A_0, is the number of precursor fragments which are excited by the photoinitiation laser. For this example, we will assume $A_0 = 100$ precursor molecules. Finally, a decay rate constant of 5.0 x 10^4 s^{-1} is chosen because it results in a decay lifetime which is well within the observable window of the apparatus.

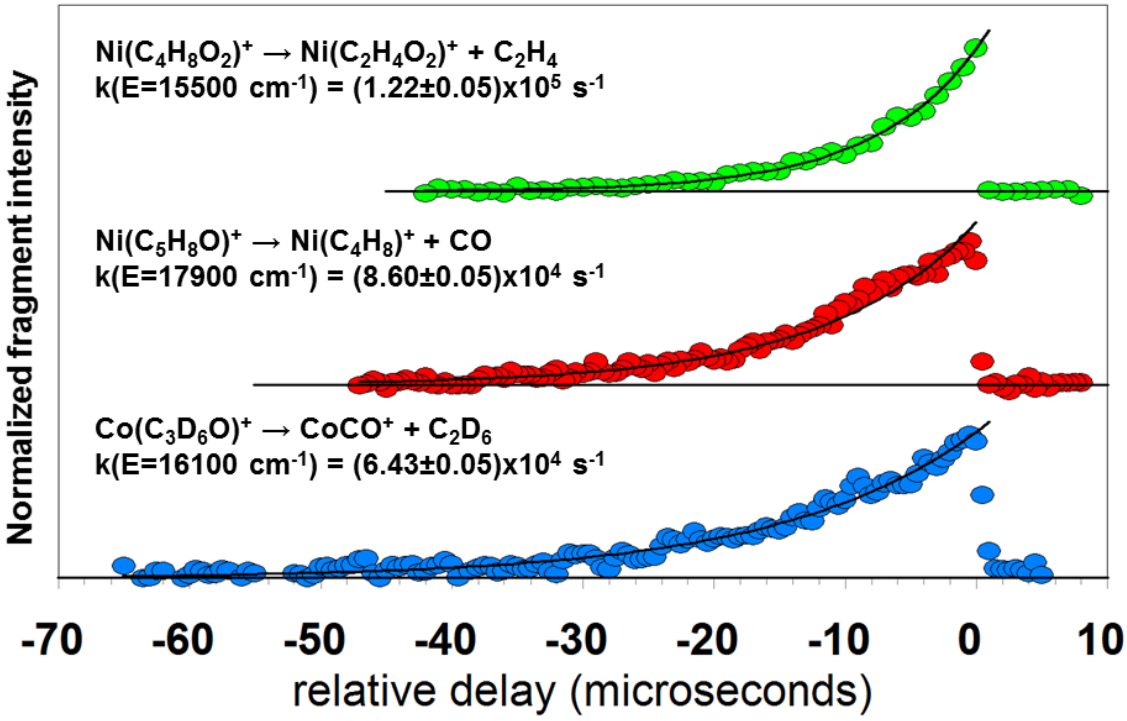

Figure 2.4. Typical SPIDRR kinetic results from three different M^+(organic) decomposition rearrangement reactions. The top panel shows the Ni^+ assisted decomposition of ethyl acetate, Ni^+ assisted decomposition of cyclopentanone is seen in the middle panel, and the bottom panel shows the Co^+ assisted decomposition of d_6-acetone. Adapted from Ref [19].

Once again, the SPIDRR technique measures the time evolution of the reaction by sampling the number of daughter fragments produced over the length of the TOFMS. The SPIDRR signal can hence be interpreted as:

$$(\mathbf{3}) \quad S(\tau) = B\left(t_f\right) - B(t_i)$$

In this case, S(τ) is the SPIDRR signal as a function of the relative laser timing delay, τ. $B(t_f)$ corresponds to the time at which the ion packet reaches the hemispherical sector and $B(t_i)$ is the time at which the ion packet exits the OA. It then follows that insertion of an appropriate rate law into Equation 3 will yield the number of daughter fragments that decay and subsequently dissociate in the TOFMS.

To develop a more general statement of the SPIDRR intensity, we can evaluate the product rate law in terms of specific experimental timing parameters. We must define our reaction times with respect to the initiation time of the reaction (t = 0) so it is convenient to specify them in terms of τ as follows:

$$t_i = \tau + \alpha$$

$$t_f = \tau + \alpha + \Delta$$

In this case, the absolute magnitude of τ is used and simply represents the time it takes the activated molecular beam to reach the OA. The transit times through the OA and TOFMS are α and Δ respectively. Based on the above formulation, a change in τ will result in new evaluation limits of the product rate law. This will cause a change in the measured daughter fragment population. This shows how SPIDRR samples the time dependent population simply by changing τ. This explanation is illustrated by Figure 2.5. As stated previously, A_0 is assumed to be equal to 100 precursor molecules, representing

an initial population of 100 photoactivated precursor molecules whose decay rate is governed by the rate constant $k = 5 \times 10^4\ s^{-1}$.

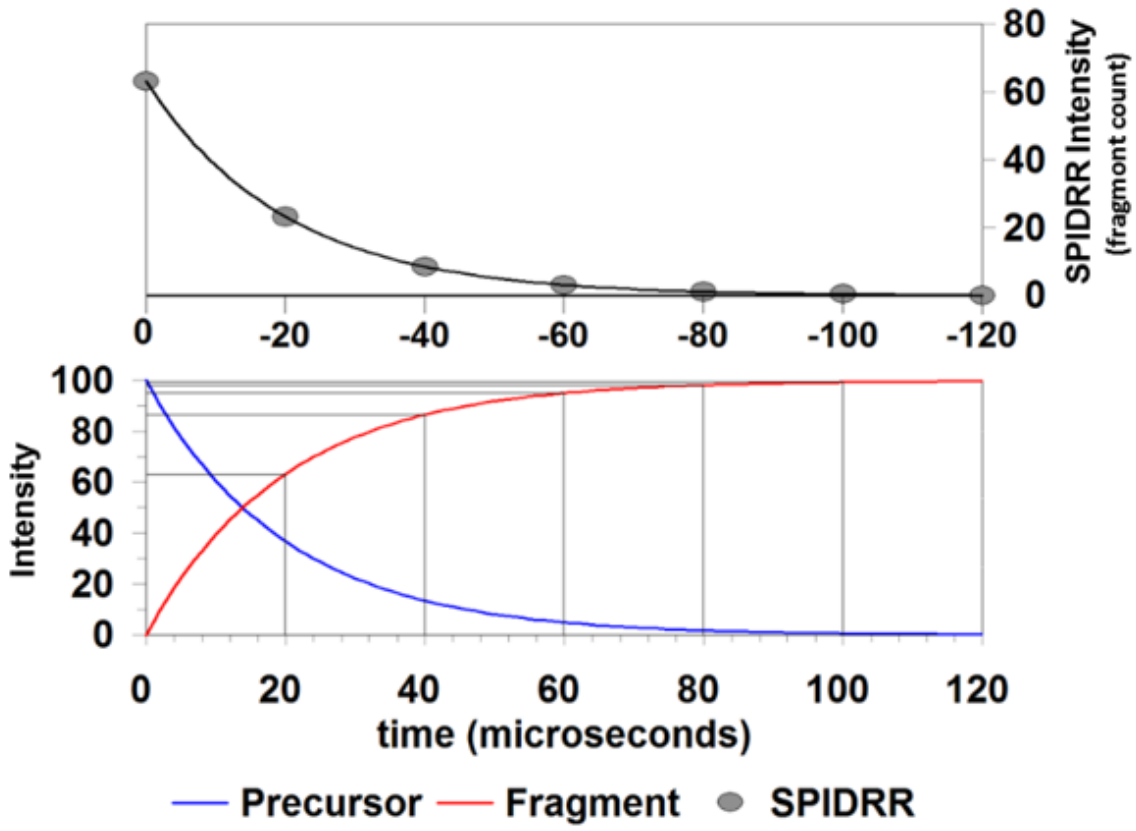

Figure 2.5. An illustration of SPIDRR data acquisition. The bottom panel shows A(t) in red and B(t) in blue. The grey bars represent sampling intervals which result in the grey data points seen in the upper panel. The upper panel is simulated SPIDRR data fit to a single exponential function which reproduces the functional form of precursor decay.

To further simplify the mathematics, we assume $\alpha = 0$ and $\Delta = 20\ \mu s$. This allows us to evaluate to product rate law from $t_f = \tau + \Delta$ to $t_i = \tau$. The assumption of $\alpha = 0$ will only shift the starting time of the resultant wave form and therefore will cause no change when plotted in relative time. Evaluation of Equation 3 at $\tau = 0$ gives:

$$S(\tau = 0) = \left[B\left(t_f = 20\ \mu s\right) - B(t_i = 0\ \mu s)\right] = 63 \text{ daughter fragments}$$

A similar evaluation of Equation 3 for τ = -20, using the absolute magnitude of τ yields an intensity of:

$$S(\tau = -20) = \left[B\left(t_f = 40\ \mu s\right) - B(t_i = 20\ \mu s)\right] = 23 \text{ daughter fragments}$$

When this process is repeated for τ = -40, -60, -80, -100 and -120 μs, a series of fragment populations is measured which decrease with increasingly negative τ. This results from the product rate law being sampled at later and later time intervals. The lower panel of Figure 2.5 shows these intervals as the grey bars. Each sampling interval yields the population data point plotted in the upper panel. Firing the activation laser at earlier times allows more time for the precursor to decay before entering the acceleration region. Subsequently leading to fewer daughter fragments being produced and measured in the TOFMS.

It is clear from Figure 2.5 that the SPIDRR waveform reproduces the functional form of the precursor rate law A(*t*). This is consistent with the interpretation of SPIDRR waveforms representing the lifetime of activated precursors in the molecular beam. This can be formalized with a general derivation when we recall that the difference in daughter fragment population at two times is also given by the following integral:

$$\int_{t_i}^{t_f} dB = k \int_{t_i}^{t_f} A(t)dt$$

This is the solution to the differential rate equation for B(t) written as a definite integral for the time interval t_i to t_f. Evaluation of this this integral with respect to the previously used time domain gives:

$$B\left(t_f\right) - B(t_i) = k \int_{t_i = \tau + \alpha}^{t_f = \tau + \alpha + \Delta} A_0 e^{-kt} dt$$

$$= A_0(e^{-k\alpha})(1 - e^{-k\Delta})e^{-k\tau}$$

The number of photoactivated precursors is still represented by A_0. The fractions of A_0 that decay in the OA and TOFMS are $e^{-k\alpha}$ and $(1 - e^{-k\Delta})$ respectively. Finally, $e^{-k\tau}$ is the functional dependence of the precursor rate law. From a mechanistic perspective, one can see that the SPIDRR waveform will in general reproduce the rate law preceding product formation, multiplied by a constant which is defined by instrumental timing parameters. This interpretation shows the unique ability of SPIDRR to sample the kinetic behavior based on the rate limiting lifetime of an activated molecular species.

SPIDDR Kinetic Range

The kinetic range of the SPIDRR apparatus is illustrated by the plot in Figure 2.6. SPIDRR signal $S(\tau)$ is plotted for a range of rate constants at maximum signal intensity, $\tau = 0$. To generate the plot A_0, α, and Δ were set to 100 precursor molecules, 3 μs, and 37 μs respectively. SPIDRR is most sensitive at a reaction rate constant of 7×10^4 s^{-1}, but rate constants between 2×10^3 and 1×10^6 s^{-1} are expected to be observable. In this range, a large portion of the total activated precursors decay completely in the 40 μs flight time which results in a larger number of detectable fragments for each SPIDRR data point. Longer lifetimes are limited by the flight time from the source block to the OA. Shorter lifetimes become unobservable as more of the fragment population decays completely during the acceleration event. The variation of signal intensity as a function of fragment decomposition rate must be considered when looking at relative branching ratios for metal/organic decomposition reactions that result in multiple exit channels.

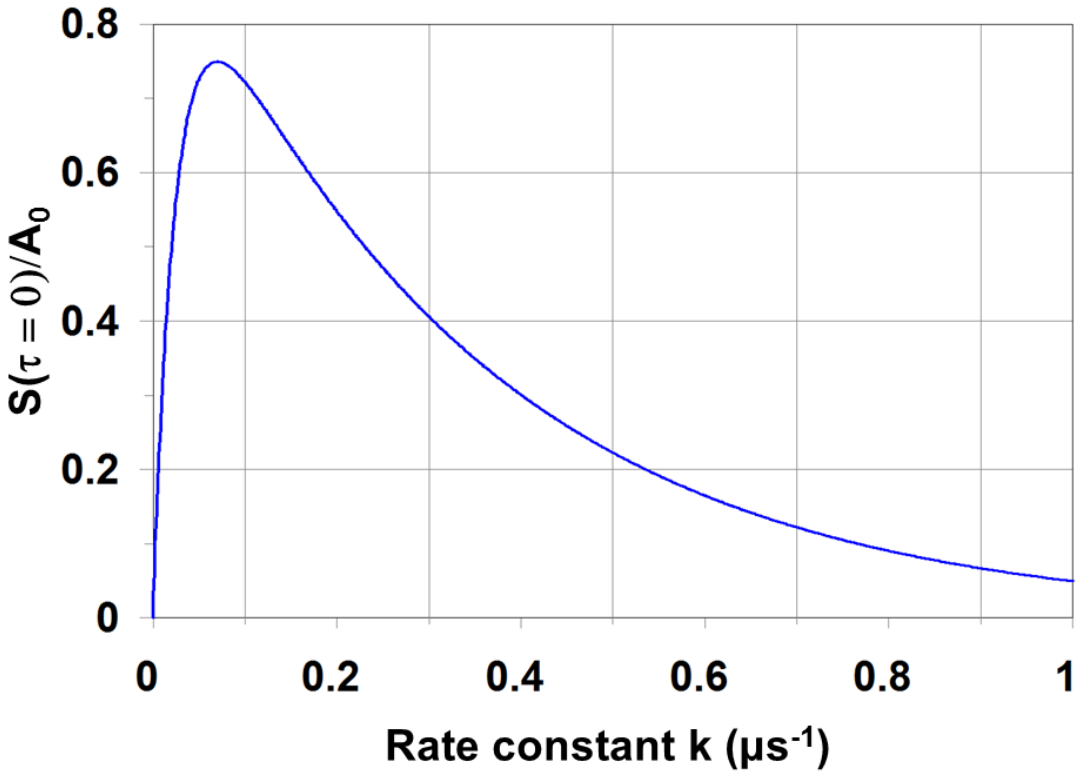

Figure 2.6. The sensitivity of the SPIDRR technique at various reaction rates is shown above. The plot was generated using $A_0 = 100$, $\alpha = 3\mu s$, and $\Delta = 37\mu s$. Adapted from Ref [19]

In the case that two distinct fragments share a rate limiting transition state and consequently a rate limiting rate constant, a direct comparison of fragment intensities can be made. However, when two daughter fragments have distinctly different decay lifetimes, a correction must be made before determining the relative branching between two pathways.

Energetic Range and Resolution

SPIDDR can measure microcanonical rate constants when the excited precursor internal energy is sufficient to overcome the rearrangement barriers leading to daughter fragments within the residence time of the expansion chamber (~400 μs). In the absence

of a tunneling event, it is the highest energy barrier along the reaction coordinate that defines the lower energy limit of a SPIDRR experiment. The upper energy limit of SPIDRR is determined by the adiabatic cluster dissociation energy. That is to say, rearrangement is not likely to more competitive than direct dissociation if the absorbed photon energy is greater than the cluster bond dissociation limit. The energy resolution of SPIDRR over this range is limited by the thermal population of the prepared molecular beam following the supersonic expansion event.

While photodissociation action spectroscopy can be used to measure the vibrational and rotational populations, no attempts to do so on previous SPIDRR systems have been successful. Instead however, the resulting signal is simply a featureless profile with intensity that scales with the laser photon fluence. The SPIDRR apparatus is capable of making such measurements,[23] however it should be noted that no electronic spectra have been reported with resolved measurements on open shell transition metal species of this size. The largest transition metal/organic electronic spectrum with this resolution was that of $Zn^+(CH_3CHO)$ reported by Kleiber.[24] This success is owed to the relatively sparse electronic structure of Zn^+ when compared to Ni^+. The spectrum measured by Klieber is likely built on a $^2P^o(3d^{10}4p) \leftarrow (3d^{10}4s)$ electronic transition. The $^2P^o$ spin orbit components lie roughly 6 eV above the ground state. For comparison, Ni^+ has seven spin orbit split states below 6 eV.[25] This increased density of states in Ni^+ combined with the large number of vibrations from the organic partner likely causes congested and therefore unresolvable PD spectra for molecules studied via SPIDRR.

SPIDRR must then resort to secondary measurements to infer the thermal population of the molecular beam. The energy resolution for systems of this size can be

determined by examining the calculated reaction barriers in the Ni^+ mediated decomposition of propionaldehyde .[26] Reaction pathways were observed leading to the daughter fragment $Ni^+(CO)$ predicted via RRKM theory to have activation barriers separated by only 1000 cm^{-1}. RRKM also predicted that the lower energy path, C-C activation, should form products at a rate too fast for SPIDDR to observe above 18,200 cm^{-1}. These predictions were reflected in experimental observation. Initially, the reaction rate scaled with energy in good agreement with RRKM. Just after 18,200 cm^{-1}, the observed rate decreased dramatically before resuming congruence with the RRKM prediction for C-H activation above 19,000 cm^{-1} (Figure 2.7).

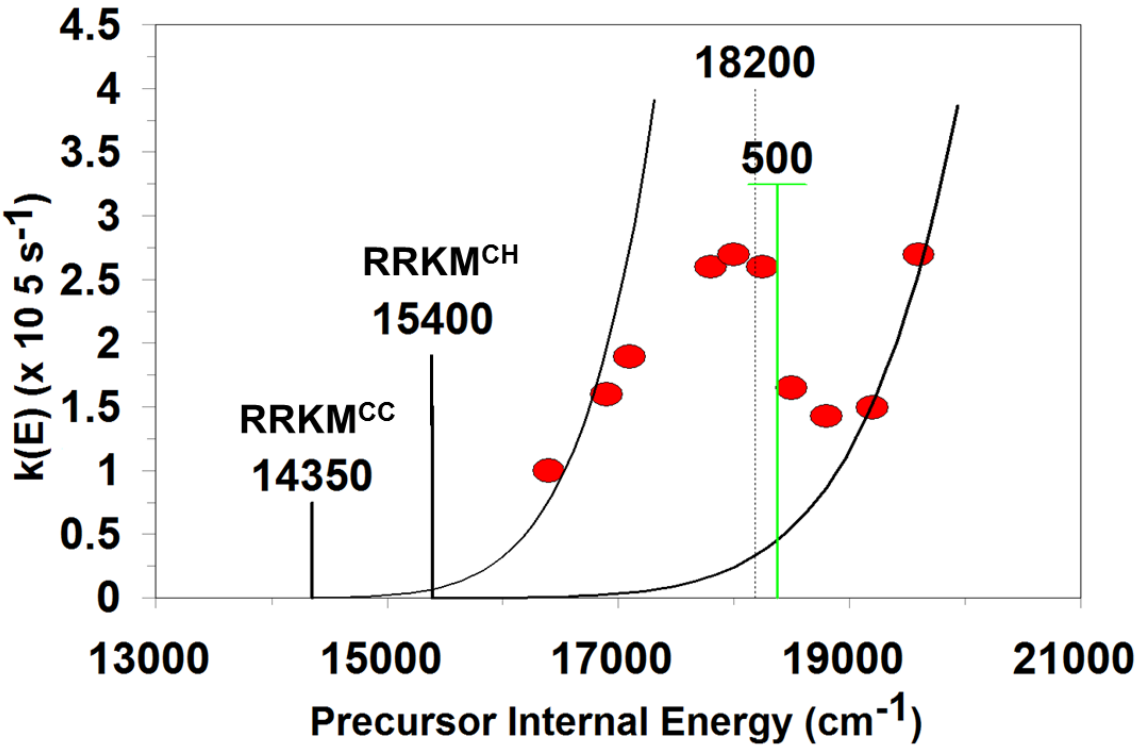

Figure 2.7. Microcanonical rate constants are plotted against internal energy in the Ni^+ assisted decomposition of propionaldehyde. The width demonstrated by the green line estimates the energy resolution of the SPIDRR technique which is related to the thermal population of the prepared molecular beam. Adapted from Ref [26].

At energies below 18,200 cm^{-1} SPIDRR sampled $NiCO^+$ fragments resulting from both C-C and C-H activation. Above this energy, SPIDRR was only able to observe fragments from the slower C-H activation process. The width of this feature (Figure 2.7) can be used to estimate the energy resolution for molecular systems of this size.

The sensitivity of SPIDRR to observe a feature such as this should be limited by the thermal population in the molecular beam. A change of 500 cm^{-1}, illustrated in Figure 2.7, is sufficient to observe a decrease in the extracted rate constant. For this reason, the energy resolution in this experiment is reported to be ±250 cm^{-1}. From this, it is assumed that the energy resolution of similarly sized systems is ± 250 cm^{-1}.

Resonance Enhanced Photodissociation Spectroscopy

The primary function of the SPIDRR instrument is to understand chemical kinetics and dynamics through first order decomposition reactions. The apparatus is also capable of making high resolution spectroscopic measurements using photodissociation techniques. Resonance enhanced photodissociation spectroscopy (REPD) is one such technique. In this spectroscopy, dissociative fragment intensity is monitored as a function of the photodissociation laser wavelength to generate an action spectrum. Action spectroscopy refers to the method of measuring fragments to collect the spectrum of a molecule rather than measuring photon absorption intensity directly.

In REPD, a fragment will only be produced and subsequently detected if the absorbed photon is of the required energy to cause excitation to a state above the dissociation threshold. If the laser energy is not at a resonant energy, no photons are absorbed and subsequently no fragments are produced. As the laser energy becomes degenerate with a transition, dissociative fragments are produced and detected which

increases the signal intensity. Once the laser scans out of resonance with this transition, photons are no longer absorbed, and fragment intensity returns to baseline. The plot of fragment intensity as a function of laser wavelength is referred to as an action spectrum. If laser resolution is sufficient and the spectral features can be resolved, action spectra can be used to measure vibrational and rotational states.

Computational Methods

Potential Energy Surface Calculations

In many cases, the use of computational methods can greatly assist in understanding the mechanism by which chemical reactions occur. In the case of SPIDDR reactions, masses of the products and reactants are known along with the lifetime of the activated species at a given activating photon energy. It is also clear that the reaction barrier must be lower in energy than the activating photon, however it is difficult to elucidate the subtle features of the reaction coordinate. The number of distinct steps of the reaction mechanism and the relative energies of each transition state are valuable pieces of information which can be predicted via computational methods. To develop a more complete understanding of these reactions, we employ ab intio calculations to locate stationary states along the reaction coordinate. In all cases, Gaussian 09 is used for electronic structure calculations.

Potential energy surfaces in the following studies are explored using density functional theory (DFT) to achieve good accuracy without incurring a prohibitive computational cost. When utilizing DFT, a number of considerations must be made when deciding which functional will be employed. The M0-X class of functionals are often

popular for computation on open shell transitional metal complexes but their general performance over a wide range of metal systems is inconsistent.[8] For this reason, heavily parameterized functionals are not considered. Available vibrational scaling factors also need to be available for the given functional based on the need for accurate thermochemical data. More specific information on the computational methods employed for each of these studies can be found in the corresponding chapters.

RRKM Theory

The determination of rate limiting transition states through ab initio calculations gives mechanistic information but also allows the modeling of the microcanonical decomposition rate constant as a function of internal energy using RRKM theory. RRKM theory is formulated as a microcanonical transition state theory and as such is well suited for comparison with SPIDRR microcanonical rate constants. The RRKM rate constant k(E) is given as follows:

$$k(E) = \frac{N^*(E - E_0)}{h\rho(E)}$$

Where the sum of states is given in the numerator and ρ(E) is the density of states. The density of states includes all vibrational degrees of freedom while the sum of states does not include the vibrational mode along which the reaction progresses. The vibrational states are acquired via thermochemical calculations in Gaussian in all cases. Activation through laser absorption deposits energy primarily in excited vibrational modes and as such a treatment of rotational contributions is not included.

A general program was written in Mathematica to calculate RRKM rate constants as a function of reactant internal energy. Calculated rate curves can then be plotted along

with SPIDRR microcanonical rate constants. This allows the determination of activation energies and can also predict the internal energy at which SPIDRR lifetimes will become too short to observe.

CHAPTER THREE

Measurement of Submerged barriers in the Ni^+ Mediated Decomposition of Propanal

Introduction

A submerged barrier is a transition state barrier which exists entirely below the separated reactant limit on a potential energy surface.[27] The ability to lower activation barriers leading to products is a hallmark of catalytic function. In some cases, this energy lowering can result in a reaction coordinate which is composed entirely of submerged barriers.[1,28-30] Building an understanding of these reactions is of great interest in catalytic research because of the high catalytic efficiency of such a reaction. Gas phase ion molecule experiments provide a fundamental understanding of the kinetic and dynamic process which govern catalytic systems in an environment free from the numerous variables present in condensed phase chemistry.[2,5,6]

The importance of this endeavor has resulted in a range of experimental ion molecule mass spectrometry based techniques. Guided ion beam techniques specifically have been successful in measuring a variety of chemical properties utilizing bimolecular collisions to determine zero kelvin bond dissociation energies using the collisional cross section.[31] Both threshold collisional activation (TCA) and kinetic energy release distributions (KERD) have extended the use of GIB to unimolecular decomposition.[6,32-34] Figure 3.1 shows the energy regimes in which bimolecular collisional studies operate compared to unimolecular techniques such as TCA and KERD. SPIDRR makes direct measurements of unimolecular decay rates in the same energy regime as TCA and KERD

but has several fundamental differences.[15,16,35-37] SPIDRR cools the reactant species through a supersonic expansion then induces decomposition through photon absorption. The activating photon energy approximates the internal energy of the reacting species. SPIDRR then initiates decomposition at well resolved precursor internal energies. SPIDRR also samples product fragments in a manner that results in increased sensitivity for notoriously low intensity signal in cation studies. The results of the following experiment indicate that the Ni^+ induced decarbonylation reaction with propanal can be made selective based on the activation energy available to the system.

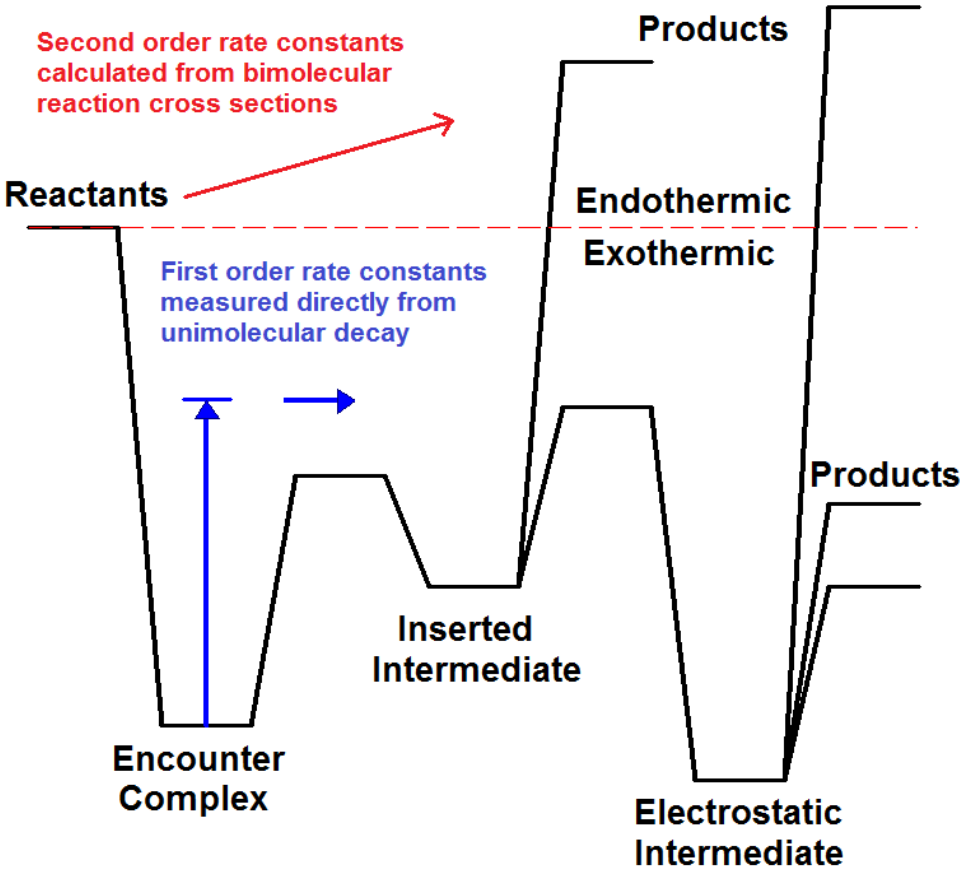

Figure 3.1. A model potential energy surface showing comparing the energy range available to bimolecular collisional studies versus techniques such as SPDRR, TCA and GIB. Adapted from Ref [26]

Results

The results in this study are comprised of a collaborative effort between experiment and theory. The submerged barriers have been measured experimentally while ab initio calculations were employed to investigate the mechanisms associated with each reaction coordinate. SPIDRR measurements on the Ni^+(propanal) precursor molecule resulted in decomposition to only one observed fragment, Ni^+(CO). Monitoring the temporal response of the fragment intensity at various activating photon energies results in the waveforms shown by Figure 3.3. The experimental data points are shown by the dots and the solid lines are exponential fits to each waveform. The waveforms are shown in increasing energy from bottom to top with extracted rate constants listed in the top left corner of each panel. A total of ten extracted rate constants from 16,000 - 20,000 cm^{-1} are reported in Figure 3.2 as $k(E)_{obs}$ where E is approximated by the activating photon energy. The observed rate limiting rate constants are plotted against precursor internal energy in Figure 3.4.

Cluster Internal Energy (cm^{-1})	Observed k(E) ($x10^5\ s^{-1}$)
16,400	1
16,900	1.6
17,100	1.9
17,800	2.6
18,000	2.7
18,250	2.6
18,500	1.7
18,800	1.4
19,200	1.6
19,600	2.7

Figure 3.2. Rate constants extracted using single exponential fits for the Ni+ mediated decarbonylation of propanal. All errors are less than 10% as determined by linear regression. Adapted from Ref [26]

A potential energy surface for the Ni^+ assisted decomposition of propanal was calculated at the UCCSD(T)/def2-TZVP//PBEPBE/cc-VDZ level of theory. The calculations were initially tested by the calculating the vibrational energy (2159 cm^{-1}) and bond dissociation energy (192 kJ/mol) for $Ni^+(CO)$. This is in good agreement with the literature values (2176 cm^{-1}, 178 ± 11 kJ/mol).[38-40] The calculated surface shown in Figure 3.3 depicts two parallel pathways leading to $Ni^+(CO)$ formation through initial insertion into either a C-H or C-C bond. C-H insertion through $TS1^{CH}$ is initially lower in energy than C-C activation.

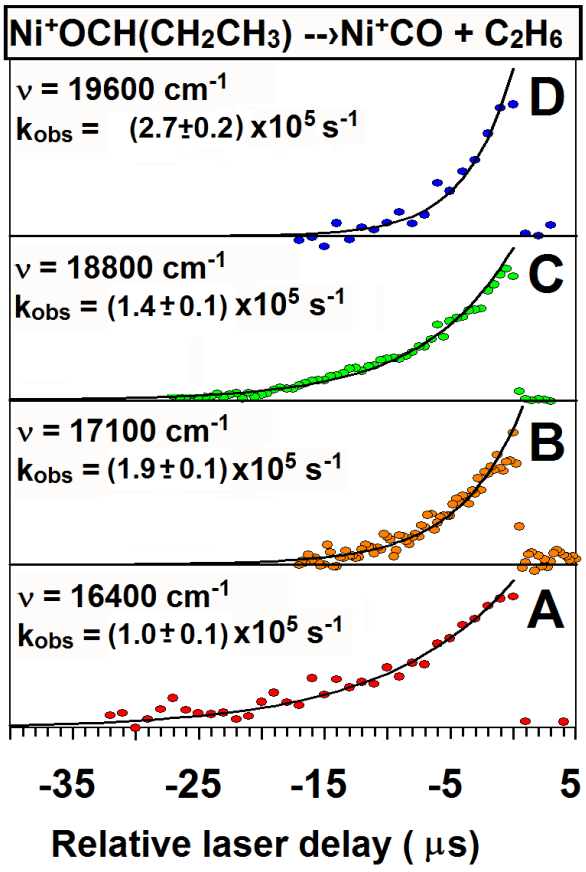

Figure 3.3. SPIDRR waveforms for the Ni^+ induced decarbonylation of propanal at 4 activating photon energies. The black traces are single exponential decay functions fit to the waveforms to yield the observed rate constants (k_{obs}) reported in the corner of each panel. Adapted from Ref [26].

Subsequent rearrangement in both process lead to a rate limiting transition state in TS3. At this point however, $TS3^{CC}$ is 1000 cm^{-1} lower in energy than $TS3^{CH}$. This means that insertion into a C-C bond results in the lowest energy pathway to products. After TS3, the two paths converge to a common intermediate and yield the same products. Insertion into the C-C bond provides the lowest energy reaction pathway despite an energetically more demanding first step. Despite the energetic demands of both C-C and C-H bond activation, it is the subsequent rearrangement in both cases that determine the activation energy of the reactions.

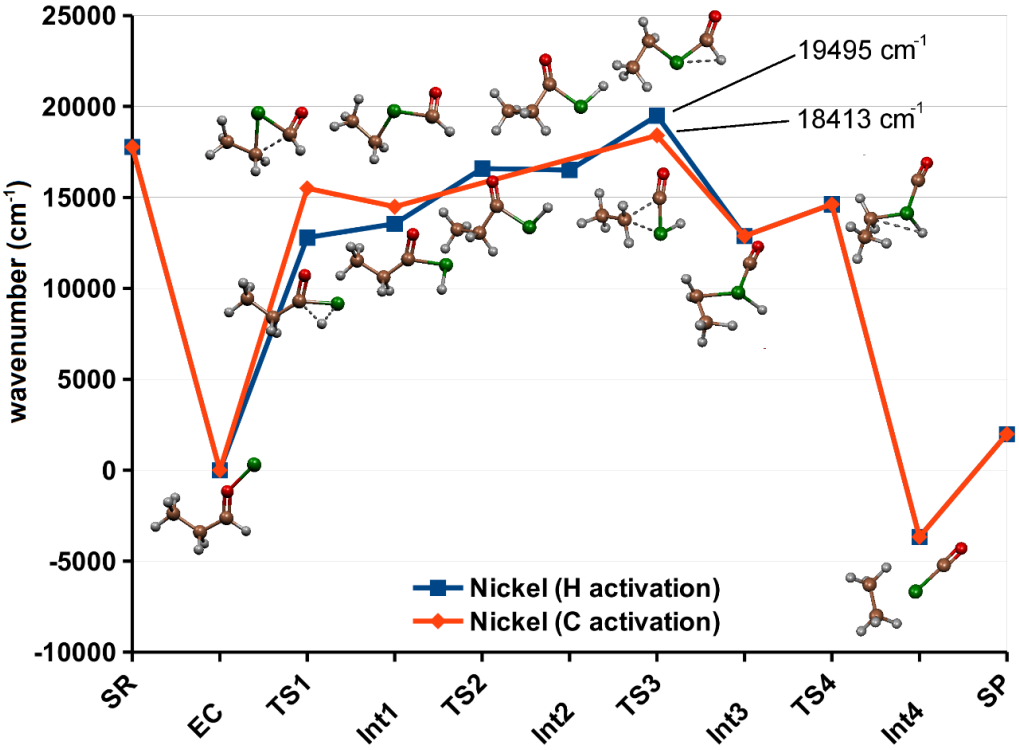

Figure 3.4. The potential energy surface calculated at the UCCSD(T)/def2-VZP//PBEPBE/cc-VPTZ level of theory. Two parallel pathways are identified which correspond to C-C and C-H activation. Further rearrangement of either insertion species leads to a global maximum at TS3. Both reaction coordinates rejoin at Int3 before yield the same products. Adapted from Ref [26].

Discussion

The plot in Figure 3.5 shows that the observed decarbonylation reaction has an unusual energy dependence. In the case that the activating photon is a good approximation of the precursor internal energy, RRKM theory should predict how the extracted unimolecular rate constant scales with energy. Initially, the reaction rate constant increases in accord with RRKM. However, there is a clear break from this trend at 17,000 cm^{-1}. The rate constant then decreases at 18,200 cm^{-1} and does not increase again until 19,200 cm^{-1}. It is then assumed that the observed rate constants must not result from a single unimolecular decay process.

A previously reported study on the Ni^+ assisted demethanation of acetaldehyde provides insight as to what may cause the unusual energy dependence of the observed rate constant. In that case, the reaction occurred on parallel competitive reaction coordinates proceeding via C-H activation/methyl migration or C-C activation/hydrogen atom isomerization. The high-energy C-H insertion process didn't occur below 17,200 cm^{-1}. Due to the functional similarities between the acetaldehyde and propanal molecules, it is proposed that a similar process causes the deviation from the expected $k(E)_{obs}$ energy dependence in Figure 3.5. A simple kinetic model (Scheme 1) is used to account for parallel competition of two oxidative addition/reductive elimination pathways. The differential rate equations resulting from that model were then integrated to yield the following solutions:

$$EC_t = EC_0 e^{-k't}$$

$$Int\ 1_t^{CC} = \frac{k_1 EC_0}{k_3 - k'}(e^{-k't} - e^{-k_3 t})$$

$$Int\ 1_t^{CH} = \frac{k_2 EC_0}{k_4 - k'}(e^{-k't} - e^{-k_4 t})$$

$$Ni^+CO_t = EC_0 - EC_t - Int1_t^{CC} - Int1_t^{CH}$$

Where EC_0 is the activated precursor population and $k' = (k_1 + k_2)$. The solutions were then input into a computer program which accounts for the SPIDRR sampling method. This program was used to assess the validity of our hypothesis that the reaction must proceed on two parallel competitive reaction coordinates by attempting to qualitatively reproduce the data presented in Figure 3.3. Simulations only matched the experimental waveforms at each energy in the case that k_3 and k_4 rate limit the reaction. Furthermore, the relative magnitudes of the rate constants from this model agree with what is predicted by the calculated potential energy surface.

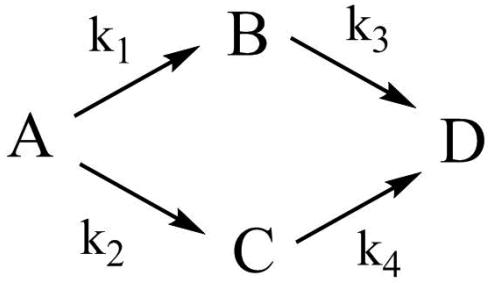

Scheme 1

With strong qualitative agreement between theory and experiment, we once again turn to ab initio calculations to further interpret the data set. Using the vibrational data from the $TS3^{CC}$, we fit an RRKM curve to the first three rate constants in Figure 3.5. Overlap with the observed rate constants was optimized by changing the activation requirements of the reaction. An activation energy of 14,350 cm^{-1} yielded the best fit. Despite this, there is still the clear deviation from this curve at energies greater than

17,100 cm^{-1}. If we extrapolate the $RRKM^{CC}$ curve to the observable SPIDRR detection limit, we realize that the instrument becomes blind to the C-C insertion process at an energy roughly equal to 18,200 cm^{-1}. This detection limit is shown in Figure 3.5 with the dashed line. This lines up with the point at which the observed decarbonylation rate constant drops significantly. We then conclude that both processes are observed below this energy. At energies much greater than 18,200 cm^{-1}, the C-C activation pathway proceeds at a rate that is outside the SPIDRR observable range. The extracted rate constants above this point then result strictly from C-H activation of propanal. $TS3^{CH}$ was then used to generate an $RRKM^{CH}$ curve fit to the last two rates in Figure 3.5. This curve predicts that C-H insertion pathway has an activation energy of 15,400 cm^{-1}.

Error in the calculated activation energies is initially determined by determining the minimum and maximum energies which still allow overlap with the corresponding rate constants. This results in an error of ± 200 cm^{-1}, which seems quite modest considering the inherent error which may exist in the computation of vibrational energies as well as the somewhat sparse dataset used to fit the RRKM curves. For this reason, the activation energies are reported more realistically as 14,350 ± 600 cm^{-1} and 15,400 ± 600 cm^{-1} for C-C and C-H activation respectively the resulting difference between these energies is 1050 ± 850 cm^{-1} which is very good agreement with the computationally predicted relative energy difference between $TS3^{CC}$ and $TS3^{CH}$.

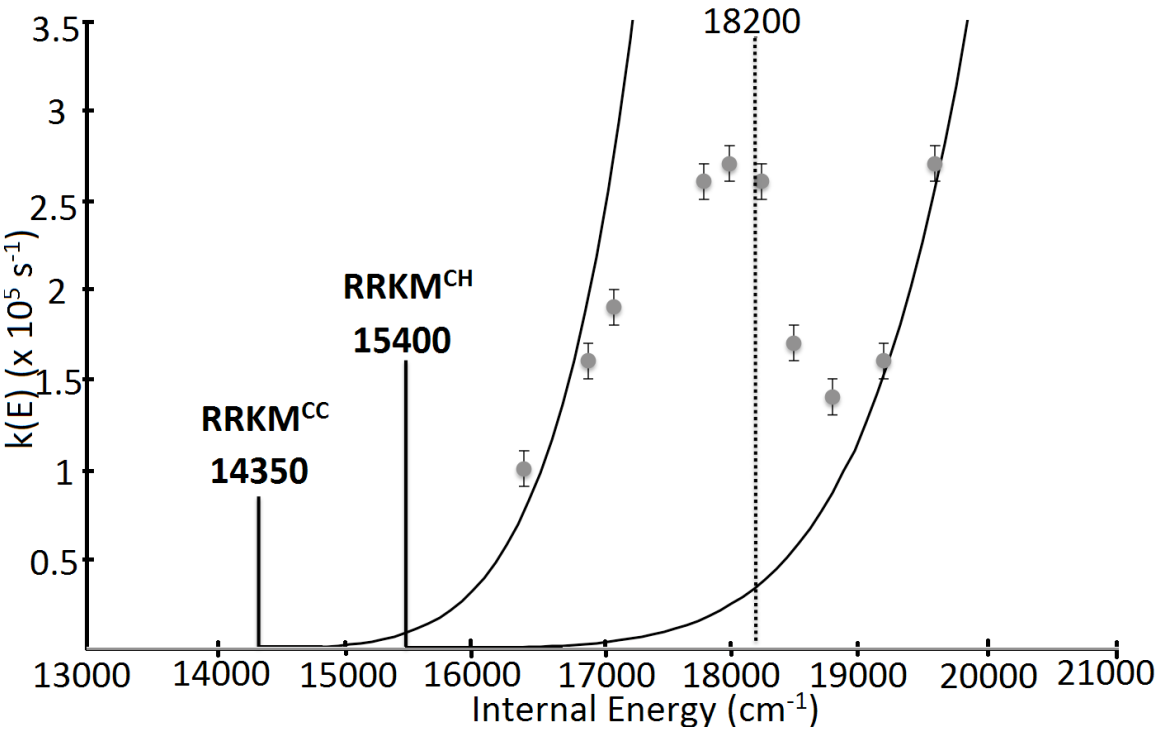

Figure 3.5. SPIDRR extracted rate constants plotted as a function of activation photon energy for the Ni+ assisted decarbonylation of propanal. The dashed line shows the upper limit of SPIDRR detection extracted from $RRKM^{CC}$. Adapted from Ref [26].

Conclusions

SPIDRR measurements were employed to study the temporal dependence of the Ni^+ decarbonylation of propanal. An unexpected energy dependence was observed when the microcanonical rate limiting rate constants were plotted as a function of activating photon energy. The use of a simple kinetic model was used to indicate that parallel competitive pathways were responsible for the observed behavior. Computational studies (UCCSD(T)/def2-TZVP//PBEPBE/cc-VPTZ) in good relative agreement with this model were used to investigate the mechanism of each reaction coordinate. The calculated potential predicted that Ni^+ insertion σ into a C-H bond would initially require less energy but would ultimately become the higher energy process by 1082 cm^{-1}. Vibrational

energies for the computed rate limiting transition states were used to generate RRKM rate curves to model the extracted rate constants. $RRKM^{CC}$ indicated that SPIDRR should be blind to decarbonylation via C-C insertion above 18,200 cm^{-1}. $RRKM^{CH}$ and $RRKM^{CC}$ were then used to determine the activation energies for each process and showed excellent agreement with the computed rate limiting transition states with a difference in activation energies of (1050 ± 850 cm^{-1}). This study shows the ability to utilize high energy resolution to make accurate quantitative measurements of rate limiting transition state barriers which lie submerged with respect to the separated reactant limit.

CHAPTER FOUR

Three Reaction Channels with Signature Proton Transfers in the Ni(I) Catalyzed Decomposition of Ethyl Acetate

Introduction

Nickel catalysis has gained tremendous interest in the last decade.[41-43] The ability of this metal center to change its oxidation state, and its location in the periodic table, topping the group 10, alongside palladium and platinum, confers this metal a broad range of catalytic capabilities. Nickel has been found to catalyze effciently almost any flavor of modern organometallic process we can think of: C-H activation processes,[44-49] carboxylations,[50,51] transamidation and amide alkylation reactions,[52,53] additions to unsaturated compounds,[54,55] cross-coupling reactions,[56-63] photoredox chemistry,[64-68] β-hydride eliminations,[50,57] bimetallic catalysis,[69] etc.

When developing and optimizing homogeneous metal catalytic processes a number of environmental variables are often explored in an attempt to optimize the reaction conditions towards a higher yield, milder conditions and lower number and proportion of undesired byproducts. These environmental variables are common regardless the kind of reaction to be catalyzed and the metal employed in the catalysis:

1. Solvation very often has a severe impact on the yield and/or product distribution of these reactions.[70-73]

2. Ligands coordinating the metal are also fundamental to achieve the desired reaction with good yields and selectivity.[74-79]
3. It is also quite common that counterions play a non-negligible role in homogeneous metal catalysis.[80-87]
4. Less often additives to homogeneous metal catalyzed reactions are also employed. These additives range from external acids to semi-metal or metal complexes which are added to the reaction mixture. The effect of these additives is also remarkable.[79]

We therefore have to conclude in that so-called metal catalysis is much more than that. Actually, the catalytic activity of the metal center is strongly modulated by environmental effects and, for this reason, the real role of the metal is, to some extent, obscured by these environmental effects. Disclosing the idiosyncratic role of the metal center in organometallic catalysis seems however fundamental for the rational development of new, more efficient catalysts. To do that, we need to probe the catalytic effect of exclusively the metal center, devoid of other contributions common in homogeneous conditions (from the solvation sphere, ligands, etc.). This is a fundamental question where computational chemistry can provide very accurate and detailed insights. However, experimental evidence for the simulated reactivity is essential to support our conclusions. Experimental gas phase organometallic catalysis is a rather difficult task, but it can be achieved with the appropriate tools. For instance, some early[88-90] and remarkable advances[2,91-93] in the field of mechanistic studies have been accomplished by a few groups. Regarding the transition metal activation of esters in the gas phase, the first experiments with simple esters were performed in the 1980's (using Cu(I))[5] whereas the

most recent advances involve complex reactivity, like cross-coupling reactions,[94] and reveal the role of ligands in the absence of other environmental effects.[95] To allow for experimental exploration of this kind of reactions, we have built an apparatus to directly measure the kinetics of metal mediated decomposition reactions in gas phase (see Methods section for details). The single photon initiated dissociative rearrangement reaction (SPIDRR) technique forms reactants into a binary, jet-cooled cluster under supersonic conditions. The system is then energized through absorption of a single visible laser photon and the temporal dependence of the subsequent rearrangement and dissociation is monitored in a custom time of flight mass spectrometer. Analysis of these data yields the rate constant for the rate-determining step of each reaction at the activating photon energy. These rate constants provide mechanistic and dynamic details of the reaction.[35,36]

Our goal is to provide accurate data on the catalytic behavior of bare metals with simple substrates such that an intimate knowledge on the actual catalytic capabilities of transition metals can be determined. This inherent catalytic power, once explored for a range of metals and substrates, should provide us with highly detailed information that can be exploited towards a rational design of new catalysts via fine tuning of the aforementioned environmental add-ons (ligands, counterions, solvent, etc). We have recently been able to determine the reaction mechanism and the kinetics of the Ni(I)-catalyzed decomposition reaction of propionaldehyde.[26] In a logic step forward, in this project we have increased the complexity of the substrate and explored the Ni(I) mediated decomposition of ethyl acetate in the gas phase. Solution phase studies on the effect of Ni(I) catalysts onto esters reveal that this functional group is not prone to suffer

any transformation with the metal in this oxidation state. The only chemistry we could find relating homogeneous catalysis of Ni(I) species and esters is the electroreduction of bromo derivatives, where the ester group is actually unaffected, except for a reduction at its α-carbon.[96-98] In contrast, the ethyl acetate substrate has shown a rather interesting and complex mechanistic manifold in the gas phase. This not only provides valuable information on the catalytic abilities of the bare metal, but also provides an excellent proof of concept regarding the synergy between experimental and computational chemistry to approach these studies.

Results and Discussion

Within the SPIDDR technique we employ two methods to determine fragment masses (see the Methods section for details). In the first, source conditions are modified (vaporization laser timing, fluence, pulse valve timing, etc.) to dissociate the precursor into fragments that are cooled in supersonic expansion and collected as a mass spectrum through the TOF (Figure 4.1). The second utilizes a kinetic energy filter (or hemispherical sector) to transmit photodissociated fragments to the detector as the potential difference across the sector halves is scanned. The benefit to the former is that the primary mass resolution of the instrument is superior (single amu) and fragment masses are more accurately assigned. The latter allows unambiguous identification of the precursor mass from which fragments are formed. Together, these methods indicate that the Ni^+(AcOEt) precursor photodissociates into five different fragment masses. These masses correspond to Ni^+ bound to acetic acid, ethanol, acetaldehyde, ketene, and ethene.

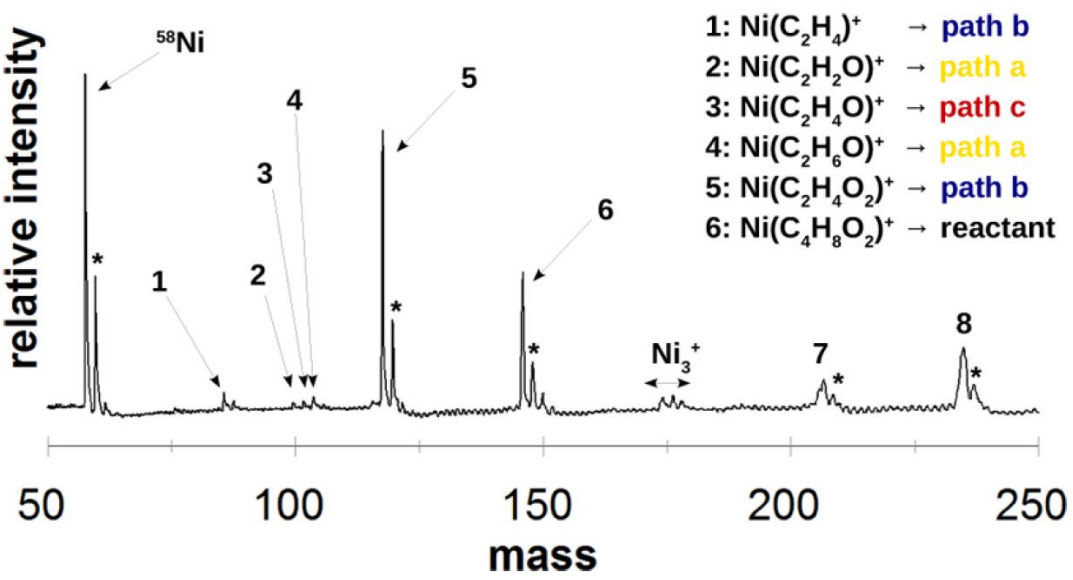

Figure 4.1. Mass spectrometry results obtained for the Ni(I) mediated degradation of ethyl acetate. Key intermediates are labeled, and the corresponding degradation pathways identified in the legend (color code consistent with that used in Figure 4.5). Isotopic peaks due to ^{60}Ni (about 25% abundance) are marked with * symbols. High mass peaks 7 and 8 are due to further complexation of the encounter complex, $Ni^+(AcOEt)(AcOH)$ and $Ni^+(AcOEt)_2$, respectively.

Figure 4.2 shows the temporal dependence of four of the five fragments monitored at an activating photon energy of 15,800 cm^{-1}. The fifth exit channel, loss of $Ni^+(C_2H_5OH)$, is low intensity and could not be satisfactorily resolved from the more intense loss of $Ni^+(C_2H_4O)$ channel. The resultant waveform of each fragment has been normalized and fit to a single exponential shown as the solid curve in each trace. Microcanonical rate constants extracted from each fit are also displayed with their associated errors. Each rate constant represents the rate limiting step within the mechanism. Although there is incomplete overlap between the error limits of each measurement, the rate constants are similar enough to confirm a very close kinetic competition between the three exit channels.

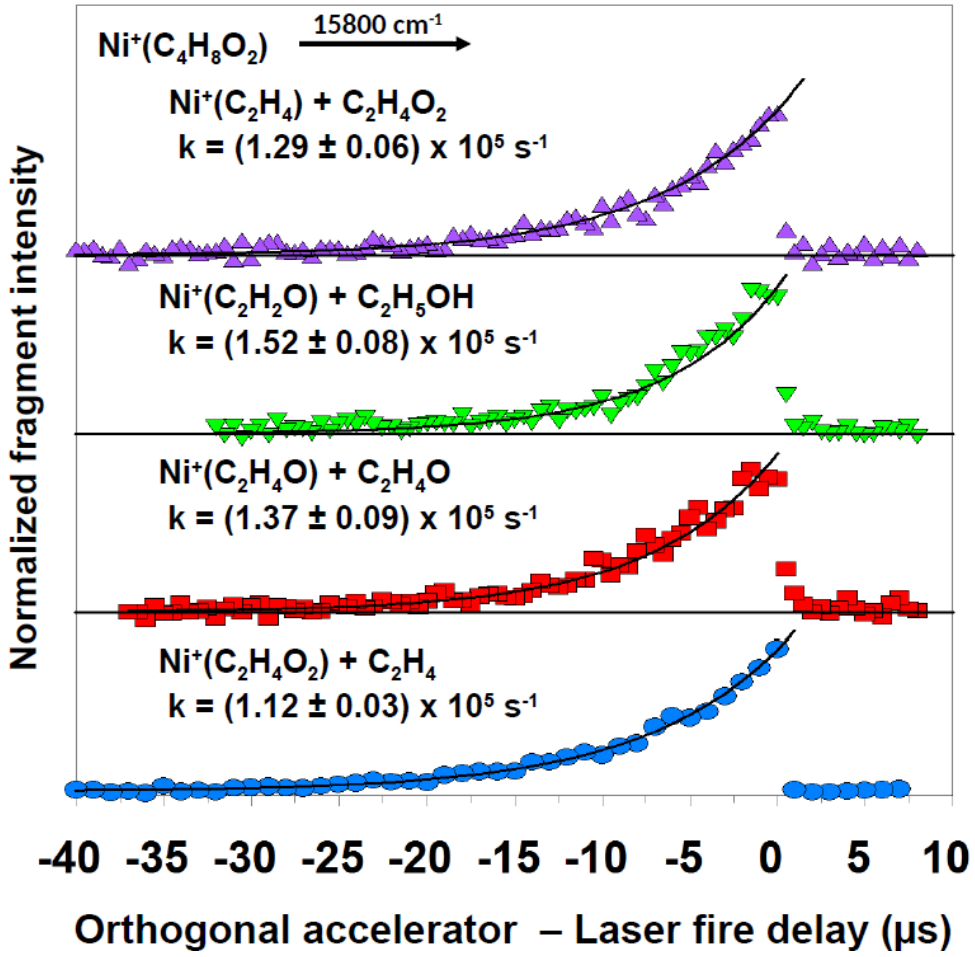

Figure 4.2. Kinetic data from the decomposition of Ni^+(AcOEt) at an activating photon energy of 15,800 cm^{-1} (45.2 kcal/mol).

Figure 4.3 shows a similar treatment for three of the have observed exit channels using an activating photon energy of 18,000 cm^{-1}. As previously, fragment intensity measurements are normalized and indicated as symbols in each trace whereas the single exponential fit is provided as a solid curve through the symbols. As expected, the value of each rate constant increased with increased photon energy compared to those presented in Figure 4.2.

The mass spectral results of Figure 4.1 and the SPIDRR results of Figures 4.2 and 4.3 provide elements of the Ni^+(AcOEt) dissociative mechanism. It can be inferred that

there are three competitive pathways to product formation and each of these has energy activation requirements below the lowest activating photon energy, 15,800 cm^{-1} (45.2 kcal/mol), used in this study. One of these pathways eliminates either neutral acetic acid or ethene, the second terminates in the production of two equivalents of acetaldehyde, while the third produces either neutral ketene or ethanol. Furthermore, the combined intensity of the $Ni^+(CH_3COOH)$ and $Ni^+(C_2H_4)$ fragments transmitted through the sector dominate the remaining exit channels suggesting that the preferred dissociative pathway eliminates these fragments and therefore has the lowest energy barriers.

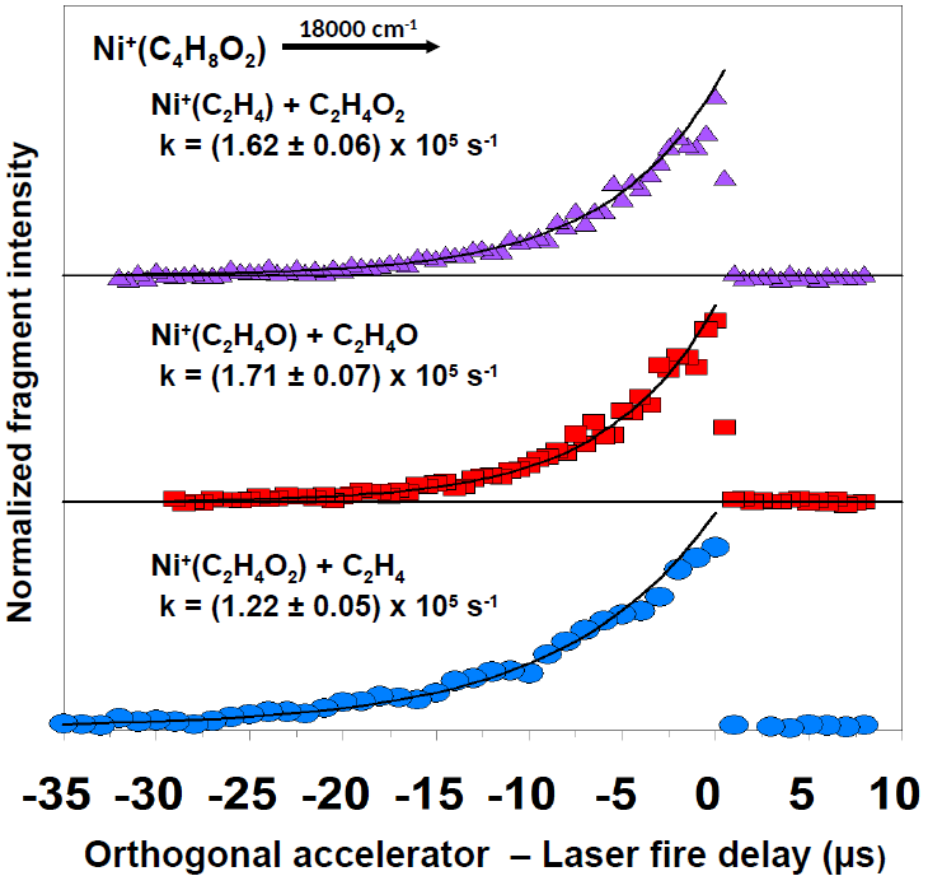

Figure 4.3. Kinetic data from the decomposition of $Ni^+(AcOEt)$ at an activating photon energy of 18,000 cm^{-1} (51.5 kcal/mol).

With this information we decided to carry out a computational exploration of the gas phase potential energy surface for the rearrangements of ethyl acetate mediated by

Ni(I) which confirmed the unanticipated complex mechanistic manifold. The organic substrate is first coordinated to the metal center through one of the lone pairs at the carbonyl oxygen atom, leading to two possible isomers of the encounter complex (ECE and ECZ, see Figure 4.4). The ECE isomer is poised to Ni-mediated C-C activation whereas the Z one is ready to activate the C-O bond. The C-C bond can be cleaved via a transition state with moderate energy requirements (28.3 kcal/mol), however, the resulting methyl-nickel complex however is rather unstable (17.6 kcal/mol with respect to ECZ) and it is therefore expected to revert to ECE.

The C-O activation can occur at both the Csp^2-O (TS1a) and the $C_{sp}{}^3$-O (TS1b) sides of the carboxylic oxygen (see Figure 4.4). TS1a requires 25.6 kcal/mol of energy to furnish the acylmethoxynickel intermediate Min1a. From this key intermediate the mechanism further bifurcates. A stepwise inner sphere hydrogen transfer involving a nickel hydride intermediate, Min2a,[99] furnishes a ketenylethanol nickel complex (Min3a) with a rate limiting step requiring 29.5 kcal/mol (Figure 4.4). Min3a was confirmed to be ~10 kcal/mol more stable with the ketene ligand attached to Ni via the carbon atom (as illustrated in Figure 4.4 instead of using the oxygen atom. interestingly, this bonding mode implies a Ni-C=C bond angle of 85.5 degrees, strongly suggesting a bonding interaction between the metal center and the cumulene carbon atom. A topological analysis of the electron density of Min3a using QTAIM theory revealed no bond critical point between Ni and the cumulene carbon (see the Supporting Information) but according to the geometry at least an agostic interaction must be present. An alternative outer sphere H-migration from the alkoxy to the acyl moiety in Min1a yields a

diacetaldehyde nickel complex (Min2c) through a transition state with slightly higher energy requirements (34.0 kcal/mol).

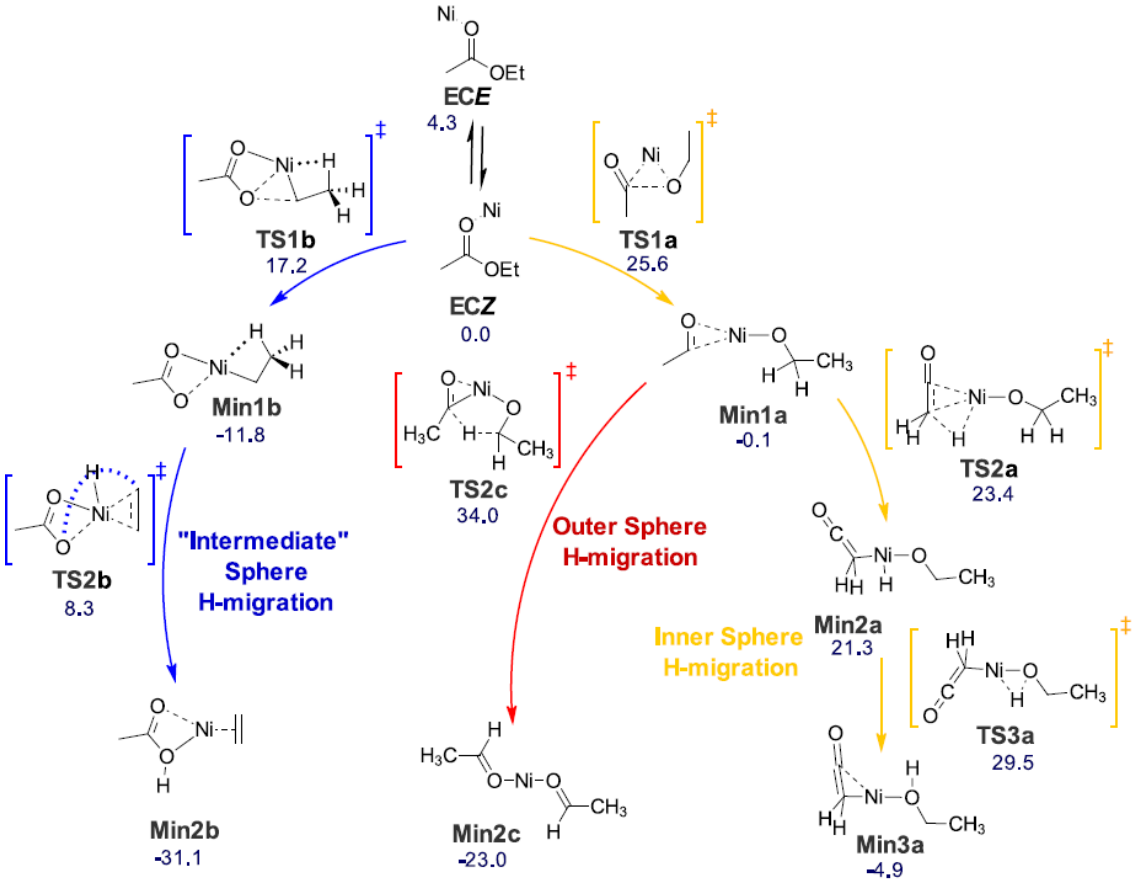

Figure 4.4. Mechanistic manifold for the rearrangement of ethyl acetate in the gas phase mediated by Ni(I) computed at the UPBEPBE/cc-pVTZ level (relative energies in kcal/mol).

Alternatively, activation of the ethyl acetate at the C_{sp}^3-O bond (TS1b) provides Min1b. This is an ethylnickel complex intermediate with a rather evident agostic interaction. Inspection of the structure of Min1b offers diagnostic parameters, namely an elongated C-H bond (1.2 Å), a very small Ni-C-H angle (77.8 degrees), coplanarity of the Ni-C-C-H scaffold and a relatively short Ni-H distance (1.7 Å). With this structure in mind we tried to locate the product of the β-elimination process, but all our attempts were

unsuccessful. Intriguingly, a transition state was located where a hydrogen atom located on the nickel atom is transferred to the acetate ligand, hence justifying the formation of Min2b. In this scenario a detailed exploration of the potential energy surface in the region between Min1b and Min2b was necessary to understand the chemistry operating along this reaction pathway (see Figure 4.5). Such exploration provided a striking combination of a β-elimination and migration onto the acetate moiety in a single step. A shoulder at the very beginning of the reaction (Figure 4.5, left) is associated with a short phase in which the β-elimination occurs, requiring about 17 kcal/mol. The structure of the complex at the inflection point features an isolated hydrogen atom on the nickel atom (see the molecular representation at the bottom of Figure 4.5). After this, the energy keeps increasing until the transition state is reached (22 kcal/mol with respect to Min1b). The geometry of this transition state and its normal mode associated to an imaginary frequency indicates that the hydrogen is already migrating towards the acetate ligand. Indeed, a subsequent and long downhill path follows in which the hydrogen atom wanders on top of the nickel atom until it reaches the acetate moiety and the latter relaxes conformationally upon protonation. The overall motion of the hydrogen atom in this step resembles that of a leapfrog game. The hydrogen atom vaults over the nickel center and this metal shows a dual role in such process, one as the barrier to be overcome to get to the acetate from the alkyl ligand and second as the point of support to achieve it. It can also be related to an incomplete orbital-like or planetary motion that has been suggested by Ugalde and Lledós in independent research.[100,101]

Figure 4.5 provides the variation of NBO charges along this step (between Min1b and Min2b), which allows us to dissect the mechanism in some chemically meaningful

phases. In the early stages of this step the migrating hydrogen atom gains considerable electron density at the expense of the carbon atom to which it is attached (C_β in Figure 4.5). The nickel center also gains some negative charge, although not as significantly. The migration occurs swiftly at around -4 $amu^{1/2}$ bohr and the charge transfer trend changes. Once the hydrogen atom is bound to nickel it starts to transfer density to it until it becomes clearly electron deficient (almost 0.5 e at 2 $amu^{1/2}$Bohr after the transition state). At this point, the hydrogen atom is fairly cationic in nature, and it is ready to protonate the acetate ligand; this occurs between 2 and 3 $amu^{1/2}$Bohr. The rest of the profile in this step is due to conformational relaxation of the proton on the acetic acid and to the acetic acid readjusting its position with respect to nickel, since it changes from a chelating ligand onto a monodentate one. This step is also quite interesting from the perspective of the analysis of the oxidation state at the nickel center. In the mechanistic manifold presented here all the intermediate structures feature Ni(III) species whereas the starting encounter complex and the final products are Ni(I) compounds. In this respect pathway b in Figure 4.4 involves a β-hydride elimination from the alkyl side, then the hydride wanders on top of the nickel center and loses electron density as it approaches the acetate ligand at the opposite side of the complex. In this process the initial hydride is transformed into a proton that neutralizes the acetate ligand and nickel accepts two electrons transported by this hydride, recovering the initial oxidation state, Ni(I).

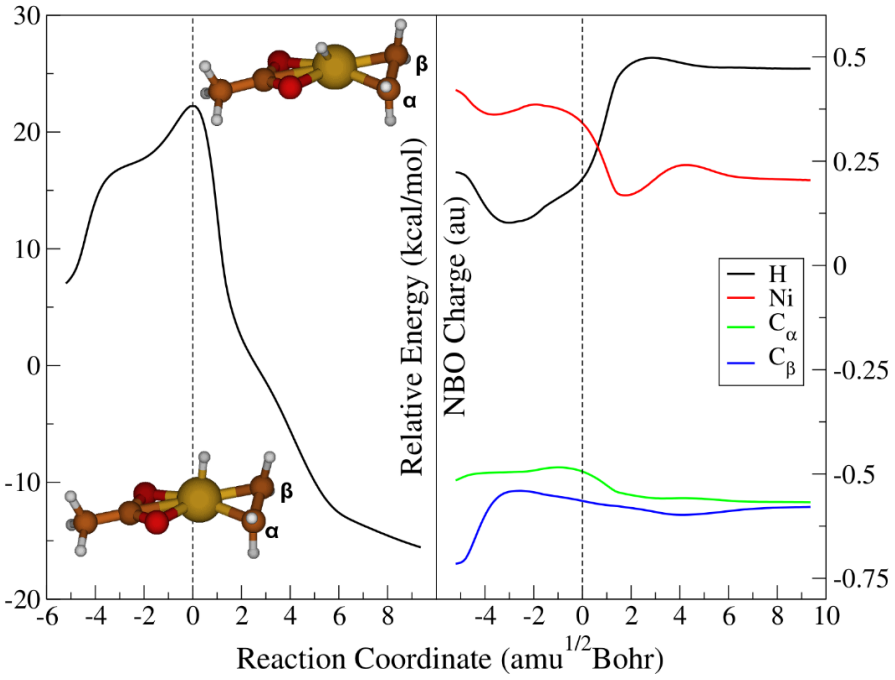

Figure 4.5. Reaction profile (left) and NBO charges (right) along the reaction for the β-elimination step in Min1b. The molecular structure at the top corresponds to the transition state whereas the one at the bottom corresponds to the inflection point earlier in the reaction profile.

Conclusions

In summary, the combined computational and experimental exploration of the decomposition reaction of ethyl acetate mediated by Ni(I) in the gas phase reveals an intricate reaction manifold that contrasts with the chemical inertness of this pair of reagents in condensed phase. Ni(I) can, devoid of environmental effects, activate C-C and C-O bonds, the latter is however the only yielding products due to the thermal instability of the intermediates formed upon C-C activation. Despite this selectivity for the C-O bond activation, the mechanistic scenario is far from simple. Three reaction pathways have been found computationally and confirmed to be operative and in close competition through gas phase SPIDRR experiments. Kinetic analysis and computation also agree in describing the most competitive mechanism branch in the manifold. The C-O activation

is significantly more favorable on the ether side, leaving the carboxyl group intact and furnishing acetic acid and ethylene through a peculiar hydrogen atom transfer that resembles a leapfrog motion. The C-O activation on the acyl side provides an initial intermediate where the mechanism bifurcates. One branch involves an outer sphere H migration to afford two acetaldehyde units whereas the other branch proceeds through an inner sphere migration to yield ketene and ethanol as final products. Agostic interactions are present at two branches: those furnishing acetic acid/ethylene and ketene/ethanol. In the former case the agostic interaction seems to be a deciding factor for the activation mode, since it significantly weakens the H-C bond facilitating the cleavage and eventual H-transfer between ligands.

Theoretical Methods

Throughout this work the Konh-Sham formulation of the density functional theory was employed.[102,103] The parameter free functional from Perdew, Burke and Hernzerhof (PBE)[104] was used along with the correlation consistent triple-ζ quality cc-pVTZ basis set.[105,106] This density functional has been tested in previous work and provided reliable results for Ni(I) chemistry.[26] The wavefunction stability for each optimized structure has also been checked at this level of theory.[107] Analysis of the normal modes obtained via diagonalization of the Hessian matrix was used to confirm the topological nature of each stationary point. Normal mode analysis and thermochemistry was obtained applying the rigid rotor and harmonic oscillator models.

On an earlier study on gas phase activation of simple organic compounds with Ni(I) Armentrout reported spin crossings between the doublet and the quartet state.[108] We therefore computed vertical excitation energies to the quartet state through single point

calculations at each stationary point of the energy profile. The doublet-quartet energy gap found for this mechanism ranges between a minimum of 40 and a maximum of 90 kcal/mol (see Figure 4.6), strongly suggesting that the reaction operates adiabatically on the doublet surface of the Ni(I) complexes. It is worth noticing that Armentrout located spin crossings for very unstable intermediates on the ground state surface (~57 kcal/mol above separate reactants), a situation that is not reproduced for the activation of ethyl acetate (all the intermediates and transition states described in this work lie at least 30 kcal/mol below the energy of the separated reactants). This can help rationalize why spin crossings may be key to explain one reaction whereas they are not found in the other.

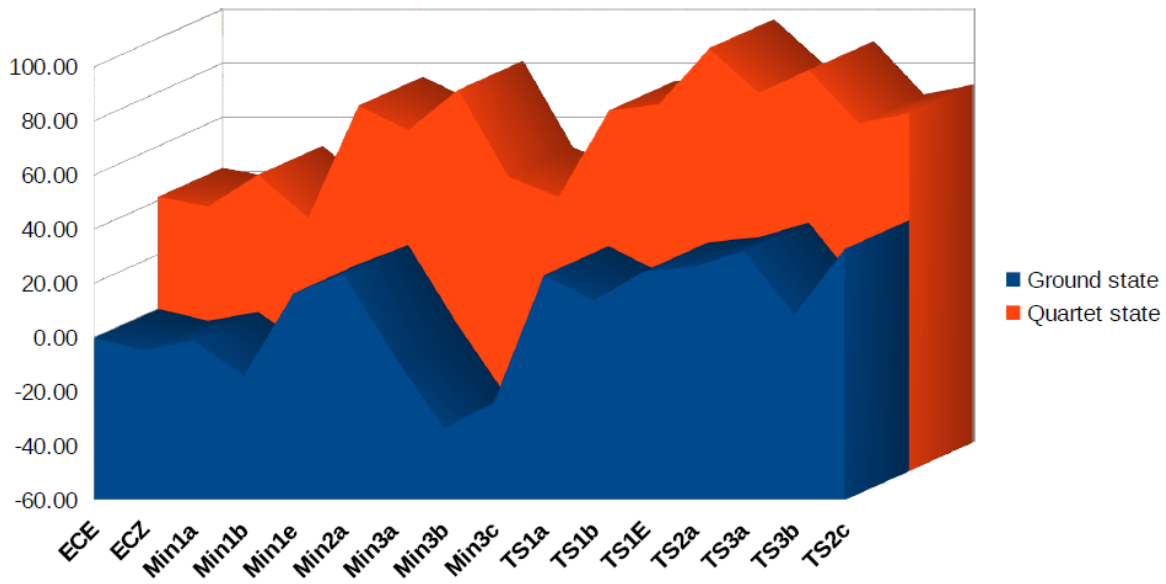

Figure 4.6. Doublet (ground state) relative energies vs. quartet vertical excitations for all the structures included in this work.

UCCSD(T) and ROCCSD(T) calculations with the same triple-ζ basis set were run in order to obtain the best possible representation of the electronic energies. Large T1 diagnostic values and T2 cluster amplitudes however suggested that these results may be

unreliable and were therefore discarded. The DFT results are more robust with respect to multireference character when these calculations are appropriately carried out.[109-111] All density functional theory and coupled cluster calculations performed in this work have been carried out with the Gaussian 09 program.[112] The topological analysis of the electron density for Min3a was performed with the AimALL package.[113]

CHAPTER FIVE

Mechanistic Intricacies of the Ni(I) Mediated Decomposition of Diethyl Ether in the Absence of Environment Effects

Introduction

In most, if not all applications, the catalytic function of the metal is accompanied by a number of environmental effects which are considered consubstantial to the process of transition metal catalytic action. These are, among others, ligands,[74-79] counterions,[81-87] solvent molecules,[70-73] additives,[79] and so on. It is however our interest to dissect and identify the catalytic effect of the metal center alone, devoid of any environmental effect.[19] The study of these isolated systems will not only facilitate a more detailed understanding of the unique role metal catalysts plays but also through comparative analysis determine what supplemental function the surrounding environment may have. Such a goal is ambitious given the number of unknown variables, but it is nevertheless key to many aspects of chemistry given the relevance of metal catalysis in a wide range of society-impacting industrial processes. We are currently focused on nickel catalysis, since it has gained tremendous interest in the last decade.[41-43] This is a versatile and highly reactive transition metal that has been found to catalyze a plethora of different reactions: C—H activation processes,[44, 49] carboxylations,[50,51] transamidation and amide alkylation reactions,[52,53] additions to unsaturated compounds,[54,55] cross-coupling reactions,[56–63] photoredox chemistry,[64–68] β hydride eliminations,[50,57] bimetallic catalysis,[69] etc. We have recently found that Ni(I) decomposes ethyl acetate through a rather complex reaction manifold in the absence of any environmental agent (the reaction

is activated in the gas phase in a high vacuum chamber, see below for details).[114] Three product channels were identified experimentally, their kinetics obtained, and a cogent and compatible mechanistic manifold was obtained through molecular simulation. In this mechanistic exploration a rather peculiar hydrogen transfer step was observed. A hydride was cleaved from one ligand, this fragment would then demonstrate an orbit like motion on the surface of the metal center while losing electron density (as in a high friction motion between two macroscopic objects of different hardness). This orbit motion ended when the hydrogen atom had virtually lost the two electrons that escorted it from the starting cleavage point. As a proton, it was added to a distant ligand featuring an available lone pair (see Figure 5.1). During its transit the hydride was therefore converted into a proton at the expense of the nickel center, that was reduced from Ni(III) to Ni(I).

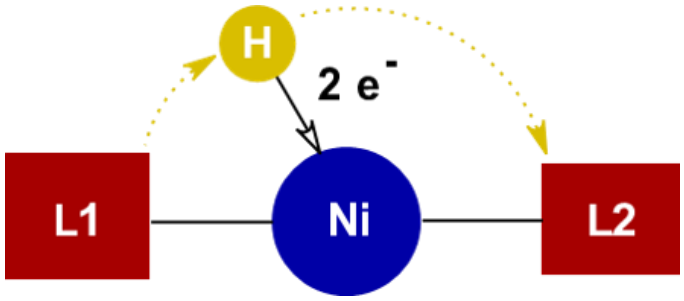

Figure 5.1. Schematic of the orbit-like hydride transfer observed in preceding work.

In the current study we are considering the decomposition of a functionally simpler substrate, diethyl ether (Et_2O). We have however found mechanistic features that are similar to those observed in the more reactive ethyl acetate. In particular, another non-least motion[49] orbit-like hydrogen transfer with concomitant metal reduction has been found. Given the rather different reactivity profile of both substrates (diethyl ether and ethyl acetate) these results may suggest that the leap-frog hydrogen migration is a more

general mechanism than we anticipated and, perhaps, it could be relatively common at least in Ni(I) chemistry.

Results and Discussion

Figure 5.2 shows a time of flight mass spectrum for the generation of the $Ni^+(OEt)_2$ clusters. Mass spectral peaks that contain Ni^+ are identifiable based on the observation of a low intensity ^{60}Ni (~25% natural abundance) peak following the major peak. The first peak in the mass spectrum is that of bare Ni^+. $Ni^+(Et_2O)$ and $Ni^+(Et_2O)_2$ have arrival times of 28 μs and 39 μs respectively. These assignments are verified through linear regression analysis. The results of the regression analysis can then be used to predict the masses for unidentified signals. Mass assignments of 73 amu and 104 are then made for the peaks at 15 and 22 μs. We can tentatively identify mass 104 as $Ni^+(CO)$. Peaks that arrive between the bare cation and the n = 1 cluster often indicate species that result from fragmentation of the n= 1 cluster.

Three fragmentation signals with observable SPIDRR decomposition rates have been identified resulting from the photo initiation rearrangement decomposition of $Ni^+(Et_2O)$. They have been identified as $Ni^+(EtOH)$, $Ni^+(C_2H_4)$ and the oxocarbenium cation $C_4H_9O^+$ which forms when a hydride is lost from diethyl either. The three decomposition fragments observed from the laser induced rearrangement of $Ni^+(OEt)_2$ are seen at sector transmission voltages of 530 V, 440 V and 375 V which correspond to masses 104 amu, 86 amu and 73 amu, respectively. The lighter peak, with an odd-valued mass (73 amu) and intensity that dominates the mass spectrum, does not correspond to any stable organic molecule bound to Ni^+. Moreover, the following minor peaks (Figure 5.2) are not consistent with an assignment of the nickel 60 isotope and quite likely are

caused by detector saturation and a slow recovery rate (commonly called ringing). Thus, we assign this mass peak as C4H9O+, the oxocarbenium cation. We therefore conclude that laser induced dissociation results in the following decomposition reactions.

1) $Ni^{+}(OEt)_2 \rightarrow Ni^{+}(EtOH) + C_2H_4$

2) $Ni^{+}(OEt)_2 \rightarrow Ni^{+}(C_2H_4) + EtOH$

3) $Ni^{+}(OEt)_2 \rightarrow NiH + C_4H_9O^{+}$

The laser induced fragmentation intensities for each observed reaction product are shown in Figure 5.3. In this case the activation laser timing is fixed to produce the maximum amount of daughter fragments while the potential difference across the hemispherical sector is scanned to identify all possible decomposition fragments. The lowest voltage transmission is that of $C_4H_9O^+$ which has a much lower relative intensity when compared to the relative intensities in the mass spectrum. However, the relative intensities of the $Ni^+(C_2H_4)$ and Ni^+(EtOH) fragments remain the same with respect to each other. This unusual behavior is also reflected when examining the kinetics of each decomposition fragment.

The temporal dependence of each reaction has been determined by monitoring the intensity of the charge carrying product relative to the reaction initiation time (triggering of the photoinitiation laser). Figure 5.4 shows SPIDRR waveforms for all three decomposition reactions initiated at a common photon energy of 16,000 cm^{-1} along with extracted rate limiting rate constants for each process. The top two panels indicate that reactions (1) and (2) proceed at a common rate. This makes sense when considering that both Ni^+(EtOH) and $Ni^+(C_2H_4)$ likely proceed via Ni^+ insertion into a C-O bond followed by hydrogen migration from the terminal methyl group to the oxygen atom. In this case,

Ni^+ insertion and subsequent rearrangement is should control the rate of reaction for both (1) and (2) while adiabatic bond scission of the fragment cluster bonds controls the relative branching between the two processes.

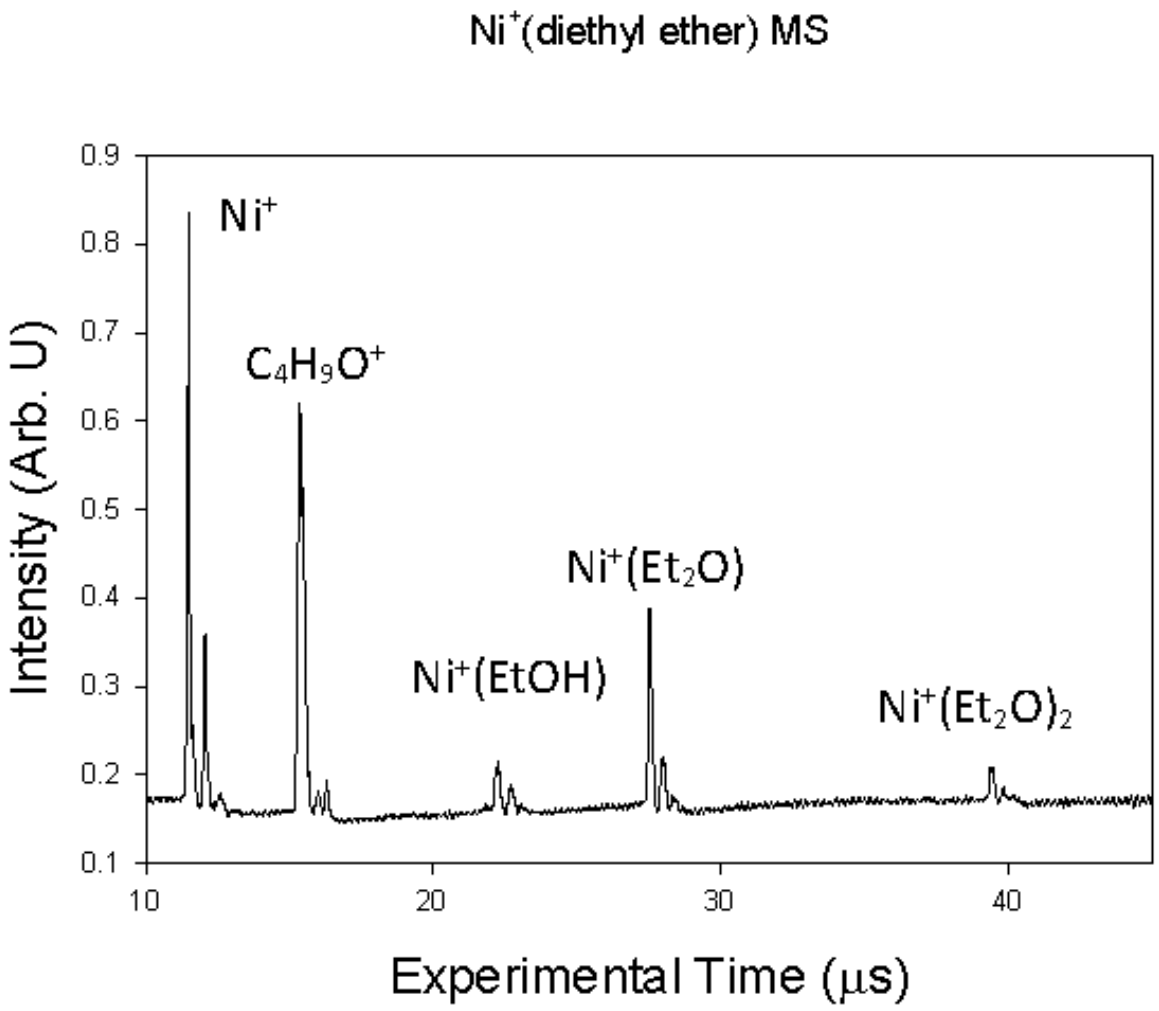

Figure 5.2. The Time of Flight Mass Spectrum for the generation of $Ni^+[(OEt)_2]_n$ clusters. The small peaks on the right-hand side of each Nickel containing species is resultant from clustering with the ^{60}Ni isotope. Detector saturation from the high intensity oxocarbenium fragment causes the isotopic ratios to be poorly reproduced.

It is clear from the lower panel of Figure 5.4 that reaction (3) proceeds at a significantly different rate compared to (1) and (2). This implies the reaction pathway leading to formation of $C_4H_9O^+$ is not rate limited in the same manner as the other two

channels. The comparatively fast reaction rate suggests that the process has either a very low activation barrier or the process itself is quite facile. In either case it would be expected that such a fast process would result in a much higher observed fragment intensity. However, the rate of formation of $C_4H_9O^+$ is sufficiently high such that SPIDRR becomes less sensitive to this process. As more of the reaction occurs during the acceleration event, the technique becomes blind to an increasing number of fragments.

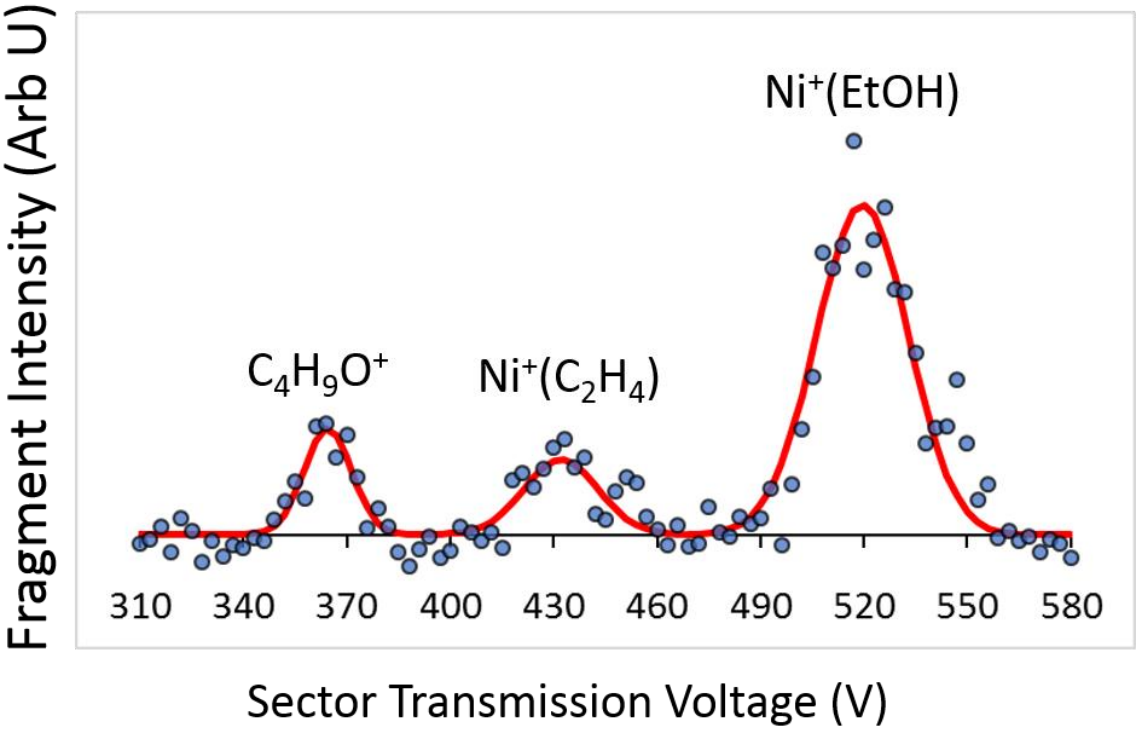

Figure 5.3. A scan of the hemispherical sector transmission voltage at fixed laser activation time. This shows relative fragmentation intensities of the observed decomposition fragments. Though Ni^+(EtOH) production is far more intense, sufficient signal was generated to measure microcanonical rate constants for $C_4H_9O^+$ and Ni^+(EtOH) formation.

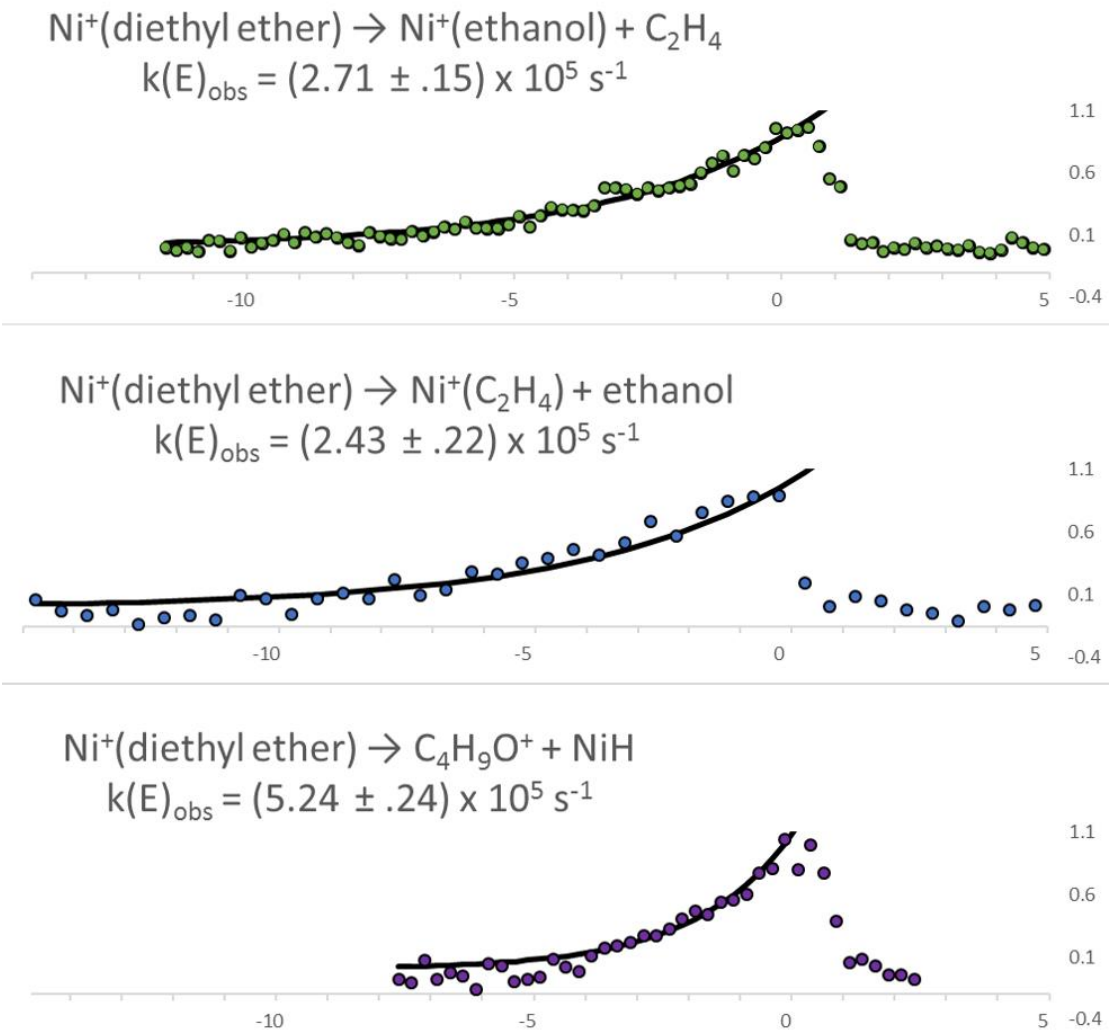

Figure 5.4. SPIDRR waveforms and observed microcanonical rate constants for the three reaction paths in the Ni^+ assisted decomposition of diethyl ether at common activation energy of 16,000 cm^{-1}. Normalized fragment intensity is plotted with respect to the relative delay of the activation laser (τ). Each waveform is normalized to the fragment intensity at time zero. The top panel refers to reaction (1), the middle panel to reaction (2) and the bottom panel to reaction (3).

A potential energy surface for these reactions was calculated in order to further investigate the reaction mechanism. Reactions (1) and (2) indeed progress via Ni^+ insertion into a C-O bond before hydrogen migration leads to the observed products. The higher observed intensity of the Ni^+(EtOH) fragment compared with that of the

$Ni^+(C_2H_4)$ fragment seems to correlate well with the relative thermodynamic stability of these exit channels (see Figure 5.5). A simple process was also found by which hydride transfer to the nickel cation occurs right from the formation of the Ni^+-diethyl ether encounter complex (hence competing with the insertion described above), leading to the observed oxocarbenium ion. The slightly faster kinetics measured for the latter process is also in agreement with the computed energy profile since the activation energy of this process is lower despite producing the least stable product (42.4 vs. 41.8 kcal/mol energy barriers for the formation of EtOH and the oxocarbenium products, respectively). This is the first time a bare charged organic fragment has been observed in a SPIDRR measurement. This is likely owed to the fact that all previously reported substrates contained a ketone functional group which would become extremely unstable following loss of a hydride. For the sake of completeness, we also computed the reverse hydrogen transfer between the two fragments formed after insertion. This reverse transfer would produce acetaldehyde and ethane, instead of ethanol and ethene. The fact that these products are not observed in the SPIDRR experiment relates well with the high activation energy computed for this transfer (55.8 kcal/mol).

Previous SPIDRR investigations on the Ni(I) mediated decomposition of ethyl acetate showed that these complexes exhibit a wealth of hydrogen migration chemistry.[114] Interestingly the three possible products described in Figure 5.5 also depend on three hydrogen migration steps. For this reason, we turned once again to computational methods to further investigate the nature of these unique processes (see Figure 5.6). The formation of the kinetically favored oxocarbenium ion occurs via a β-elimination process that yields a nickel hydride. This is therefore a simple inner-sphere hydrogen migration.

The formation of the kinetically unfavored and unobserved acetaldehyde product occurs through an outer-sphere hydrogen shift (i.e. involving only the two organic fragments). Finally, the formation of ethyl alcohol and ethene involves a large-scale hydrogen migration that closely resembles the leapfrog process that we have recently described.[114] In this occasion the two organic fragments (ethoxy and ethyl) are located very distant from each other (an anti relative position) and stay in that configuration during the entire migration. An α-hydride is cleaved from the alkyl moiety and follows a half-orbit motion around the nickel center. In this transit it loses two electrons and ends, as a proton, neutralizing the ethoxy fragment. In the course of this migration therefore the Ni(III) center is reduced back to the starting Ni(I) state.

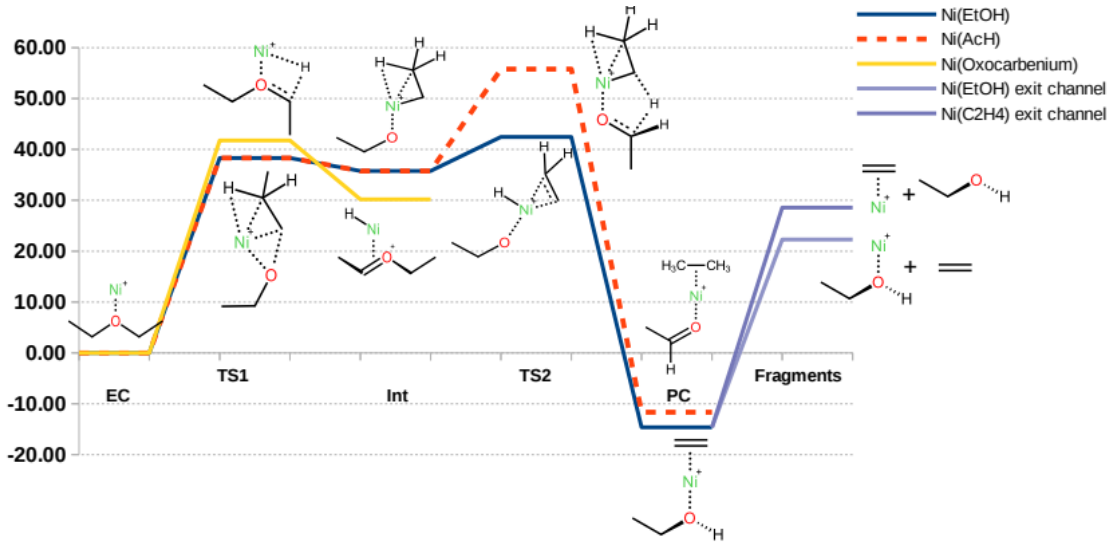

Figure 5.5. Energy profiles for the different pathways considered in the Ni-mediated decomposition of ethyl acetate computed at the MRMP/CC-pVDZ//PBE/CC-pVDZ level.

It is noteworthy to mention that the MRMP methodology employed and discussed in detail in the computational section is clearly justified in terms of the electronic configuration of some of the intermediates and products found along the mechanism

described above. Usually transition states, where the electron density is more delocalized, and the chemical bonds are stretched, are candidates to show multireference character. This was the case also in the Ni-mediated decomposition of ethyl acetate. However, in this study even some of the products show some multireference character, which happens less frequently. The singly occupied molecular orbitals (SOMO) for products **C** (observed experimentally) and **D** (not observed) are drastically different. In the former the unpaired electron is located in a d_z^2 orbital at the nickel center, which is oriented perpendicular to the molecular plane, however, in the latter, the SOMO lies in the molecular plane and features a $d_{x^2-y^2}$ shape (see Figure 5.7).

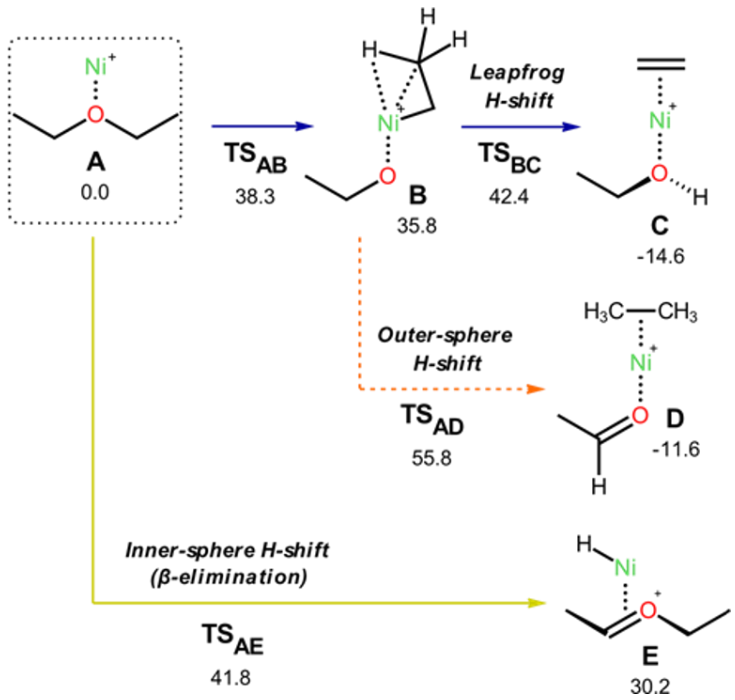

Figure 5.6. Schematic representation of the reaction mechanism corresponding to the profiles provided in Figure 5.5.

These results help explain the complexity of the Ni(I)-mediated chemistry even when very simple ligands are being transformed. Relatively delicate changes in the nature

of the ligands translate into drastic changes in the electronic structure of the metal center, which, as a consequence, catalyze radically different processes. And this can be illustrated even at one of the simplest chemical reaction, the hydrogen migration.

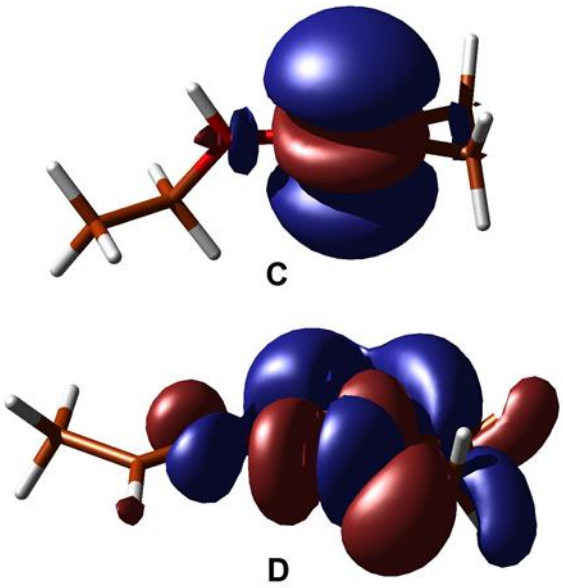

Figure 5.7. Single occupied molecular orbital (SOMO) for product **C** (top) and **D** (bottom).

Conclusions

The SPIDRR technique was used to examine the gas phase reactivity of the Ni^+ mediated decomposition of diethyl ether. Rate limiting rate constants have been determined for three fragmentation channels. Two of the observed products, $Ni^+(EtOH)$ and $Ni^+(C_2H_4)$, are formed through a common rate limiting step. The final product was the unexpected oxocarbenium cation, $C_4H_9O^+$, which was formed at a comparatively fast rate despite its relative thermodynamic instability compared to the other products. Despite reported successes in describing the SPIDRR results of Ni+ based chemistry, previously used levels of theory proved incapable of describing the multireference

character of the reaction intermediates and transition states. For this reason, MRMP/cc-pVDZ//PBE/cc-pVDZ was employed to evaluate the reaction coordinate. This theory describes a series of hydrogen migration events that lead to the observed reaction products. Another leap frog like orbiting hydrogen transition state was observed. This in combination with the previously reported outer sphere migration seen in the Ni+ mediated decomposition of ethyl acetate indicates that the process may be a theme in Ni+ activation of small organic fragments. This study also demonstrates the importance of accurately describing hydrogen migration events to the understanding the dynamics of Ni^+ chemistry.

Computational Methods

Throughout this work the Konh-Sham formulation of the density functional theory was employed.[102,103] The parameter free functional from Perdew, Burke and Ernzerhof (PBE)[104] was used along with the correlation consistent double-ζ quality cc-pVDZ basis set.[105,106] This density functional has been tested in previous work and provided reliable results for Ni(I) chemistry.[114] The wavefunction stability for each optimized structure has also been checked at this level of theory.[107] Analysis of the normal modes obtained via diagonalization of the Hessian matrix was used to confirm the topological nature of each stationary point. Normal mode analysis and thermochemistry was obtained applying the rigid rotor and harmonic oscillator models.

Given the multireference character found in some structures involving Ni(I) catalysis we decided to employ methodology that can accurately describe non-dynamic correlation. CASSCF wavefunctions can describe appropriately this multireference character, but they only include a limited and undetermined amount of non-dynamic

correlation. Given the importance of dynamic correlation in electronic structure calculations, a balanced amount of both is desirable. To consider both electronic components at a reasonable computational cost we included the treatment of dynamic correlation in the multireference scheme via perturbational theory, MRMP, as implemented by Nakano.[115,116] Single point calculations at PBE/CC-pVDZ geometries were performed at the MRMP(5,5)/CC-pVDZ. The resulting level of theory is usually noted as MRMP(5,5)/CC-pVDZ//PBE/CC-pVDZ. This strategy relies on the fact that density functional theory geometries are often accurate even when the electronic structure of the species under study exceed the capability of this single determinant method. We have already employed this approach successfully for organic molecules with strong diradical character.[117]

CHAPTER SIX

Chemical Dynamics in the Co^+ Mediated Decomposition of the Acetaldehyde Molecule

Introduction

Many previously reported SPIDRR studies have focused on Ni^+ mediated decomposition.[15,16,26,36,37,114] Interesting dynamic processes facilitated by the nickel cation have been discovered through the course of these studies, but it is of great interest to extend the power of SPIDRR studies to reactions involving other transition metal cations. One previous SPIDRR publication focused on the Co^+ assisted decomposition of the acetone molecule.[35] This study reported microcanonical decomposition rates at various laser activation energies for both acetone and its d_6 labeled isotopologue. Furthermore, comparisons were made with the unimolecular decay dynamics of previously studied Ni^+(acetone).[35] The laser induced decomposition of Co^+(acetone) was uniformly faster than that of Ni^+(acetone).[35] The cobalt species also exhibited a rather modest kinetic isotope effect (KIE) of 1.5 upon deuterium labeling of the organic compared to the large KIE of 5 reported for Ni^+(acetone) decomposition. Finally, it was suggested that spin inversions along the reaction coordinate may play a role in Co^+ mediated decomposition owing to its relatively dense electronic structure at energies accessible to the photoactivated species.

A continued study of cobalt cation reactivity offers the opportunity for direct comparison with multiple Ni^+ based decomposition reactions, while simultaneously investigating the role dense electronic structure may play in SPIDRR kinetics and

dynamics. Acetaldehyde (AcAld) was chosen due to its relative simplicity. Though it is structurally smaller than the previously investigated acetone molecule, it is functionally more complex in that metal insertion may occur through C-C or C-H activation. A SPIDRR study has also been reported for the Ni^+ assisted decomposition of acetaldehyde which will allow a comparison of the reactivity between the two transition metal cations.[37]

Results and Discussion

The time of flight mass spectrum for cluster formation of Co^+(AcAld) is shown in Figure 6.1. The earliest and most intense peak is that of the bare cobalt cation. Following this, is a small peak at mass 87 which is the decomposition product Co^+(CO). This peak likely results from decomposition rearrangement in the high energy laser vaporization plume that occurs just before the supersonic cooling event. The peaks at masses 103 and 147 correspond to Co^+(AcAld) and $Co^+(AcAld)_2$ respectively. Only a single decomposition fragment is observed following laser activation of the Co^+(AcAld) precursor. The fragment transmits to the detector when the sector is tuned to 550 V which corresponds to a mass of 87 amu. This is consistent with the TOFMS peak Co^+(CO). Based on the decomposition of Co^+(AcAld) into a single observed reaction product, the following reactions are proposed:

$$Co^+(AcAld) \rightarrow Co^+(CO) + CH_4$$

$$Co^+(AcAld) \rightarrow Co^+(CH_4) + CO$$

The $Co^+(CH_4)$ fragment is not observed. This could be based on the thermodynamic stability of the Co^+(CO) fragment. The results of initial kinetic experiments are shown by the three waveforms in Figure 6.2. Each waveform results

from the formation of $Co^+(CO)$ at different activating photon energies. Over this energy range, 16,000 – 15,700 cm^{-1}, the waveforms are well modeled by a single exponential decay function. This indicates that at each energy, the reaction proceeds through a single rate limiting transition state. In this case, both C-C and C-H activation must lead to a common rate limiting step or the observed products result from a single insertion event.

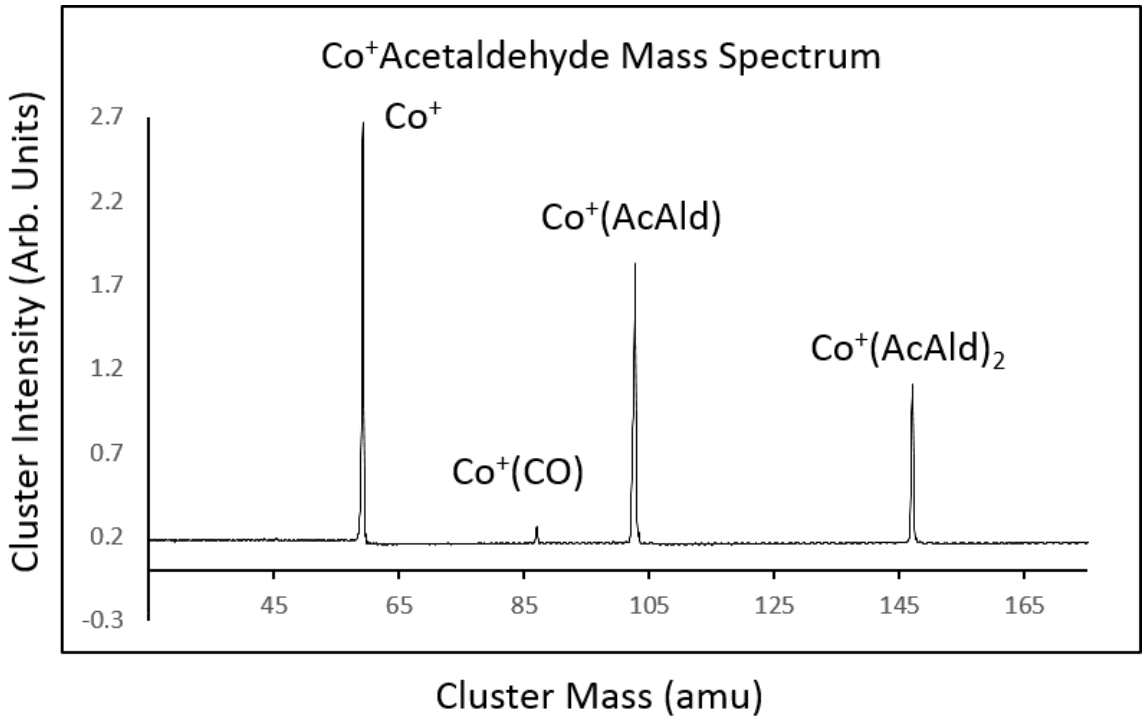

Figure 6.1. The Time of Flight mass spectrum for the formation of Co^+(acetaldehyde) clusters.

Despite lower signal to noise during the collection of decomposition kinetics at 16,000 cm^{-1}, analysis shows that each change in activating photon energy results in a distinctly different observed microcanonical rate constant. Furthermore, the observed rate constant decreases as a function of activating photon energy. This is the expected behavior predicted by RRKM theory and as such it is of interest to determine if RRKM theory can well describe the energy dependence of the observed rate constants. A

Mathematica program was used to compute RRKM rate constants. Ab initio calculations were performed at the UwB97xD/Def2SVPP level of theory and will be discussed later. Normal modes and electronic energies for the calculated stationary states were used as the input deck for RRKM calculation. A comparison of the RRKM prediction with experimentally determined rate constants is shown in Figure 6.3. The RRKM rates are in good agreement with experimental observation.

An attempt was made to measure rate constants of the reaction at higher energies, however dissociation rearrangement fragments were not observed above the reported energy of 16,000 cm^{-1}. Based on the RRKM prediction, we do not expect the SPIDRR apparatus to be sensitive to reaction rate constants at energies above 16,500 cm^{-1}. Near this energy the reaction is expected to occur almost entirely in the ~3 μs flight time through the OA. SPIDRR will then not be able to detect these fragments.

An earlier SPIDRR investigation successfully used RRKM theory to predict the activation energies of two parallel competitive reaction pathways. The good agreement with RRKM in the current study prompted comparison of the reaction rate constants at low energies to benchmark the theory near the activation energy. The next available low energy laser dye (LDS 698) successfully produced detectable decomposition fragments at 14,700 cm^{-1}. The resultant waveforms are presented in Figure 6.4. There is a large increase in the lifetime of the activated precursor reflected by the much longer scan length. The purple data was taken from the upper panel of Figure 6.4 and shows a nearly four-fold increase in the time required for fragment production to terminate.

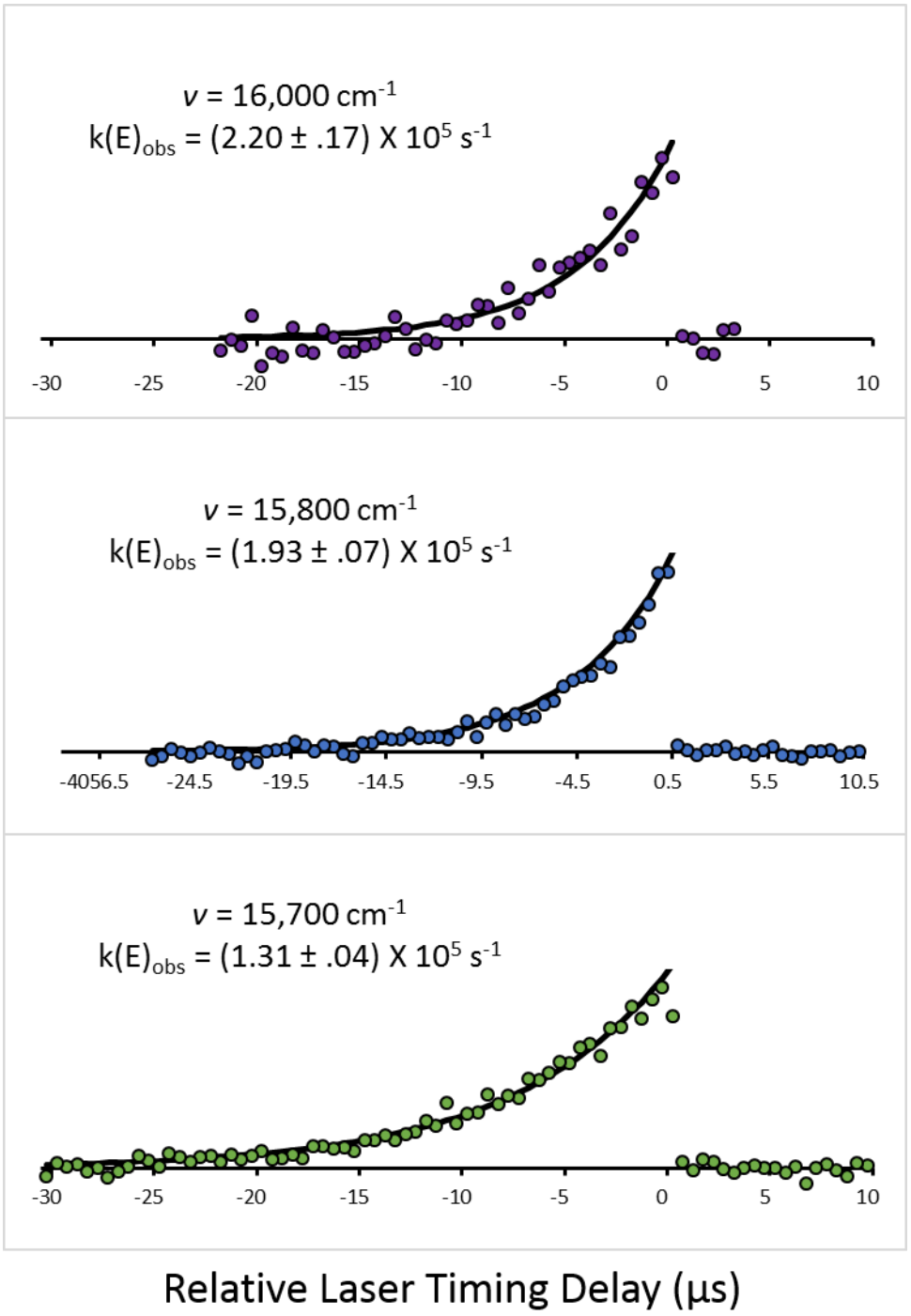

Figure 6.2. SPIDRR kinetic waveforms for the $Co^{+}(CO)$ decomposition fragment at three different activating photon energies. All waveforms have been normalized to maximum signal intensity for comparison. Reported microcanonical rate constants are in the left corner of each panel beneath the corresponding laser photon energy. Time is reported in the relative laser timing delay (τ).

The bottom two panels also deviate significantly from single exponential behavior. The reported rates for these waveforms were extracted using a sum of two exponential decay functions., this means that the decomposition fragments observed at this energy do not proceed through a single rate limiting transition state. All extracted microcanonical rate constants are reported in Figure 6.7. The biexponetial fit is convenient for the purposes of comparison with the data above 15,700 cm^{-1}.

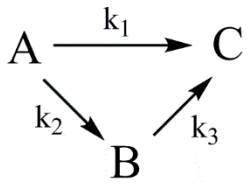

Scheme 1

The more complex waveform then requires the development of a kinetic model in order to determine rate constants. A simple case reaction mechanism (Scheme 1) was built to allow more flexibility but still retain the physical meaning of extracted rate constants. Using this mechanism, a series of differential rate equations were developed. The solutions to the equations shown below were written into a python program (see appendix) which accounts for the sampling method of the SPIDRR apparatus. The SPIDRR waveforms were then fit using this program.

$$A(t) = e^{-(k_1+k_2)t}$$

$$B(t) = \frac{k_1 A_0}{k_3 - (k_1 + k_2)}\left(\frac{e^{-(k_1+k_2)t}}{k_1 + k_2} - \frac{e^{-k_3 t}}{k_3}\right)$$

$$C(t) = \frac{k_1 k_3 A_0}{k_3(k_1 + k_2)}\left(\frac{e^{-k_3 t}}{k_3} - \frac{e^{-(k_1+k_2)t}}{k_1 + k_2}\right) - \frac{k_1 A_0}{k_1 + k_2} e^{-(k_1+k_2)t} - \frac{k_1 k_3 A_0}{k_3(k_1 + k_2)} - \frac{k_1 A_0}{k_1 + k_2}$$

The results of the kinetic model applied to the SPIDRR waveforms at an activating photon energy of 14,700 cm^{-1} is shown in Figure 6.5. The bottom panel shows the time dependence of each intermediate in the mechanism. The upper panel shows the time dependence of the product C(*t*) as sampled by the SPIDRR technique and fit to the experimental data. The result is two rate constants k_1 and k_2 which are somewhat competitive.

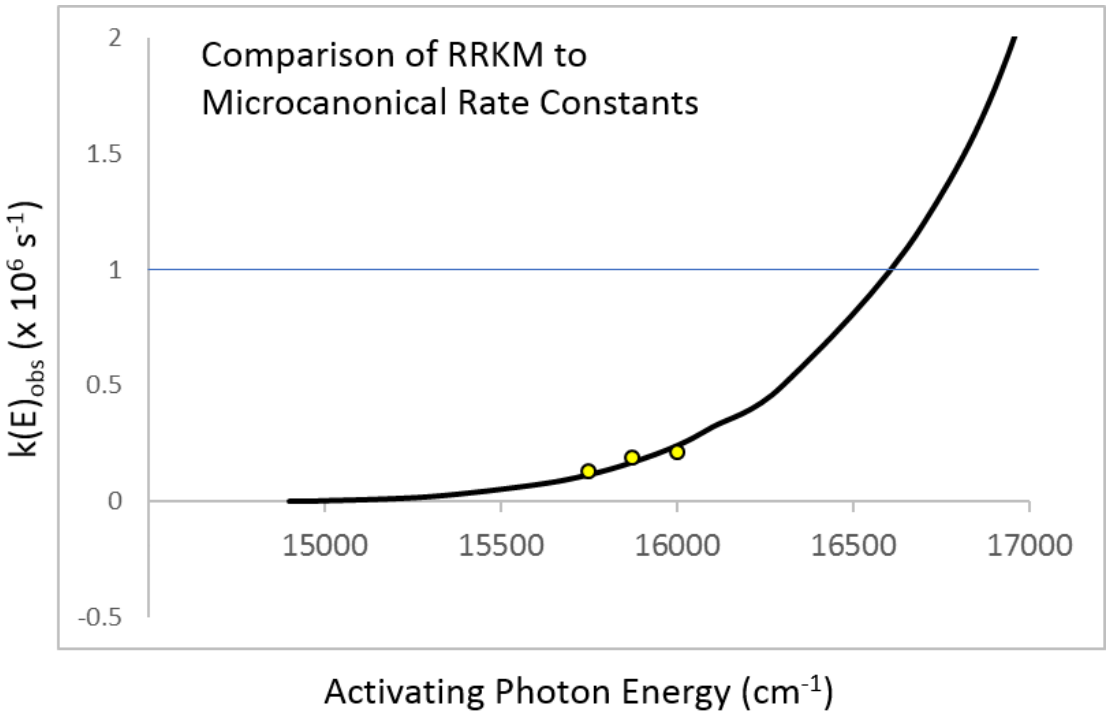

Figure 6.3. A plot of the experimentally determined microcanonical rate constants with the RRKM theory prediction of how the rate constant scales with internal energy. The yellow points are the three rate constants reported in each panel of Figure 6.2, the black trace is the RRKM prediction and the blue line marks the upper limit at which SPIDRR can measure rate constants.

A(*t*) shown in red, decays rapidly and is completely depleted within the first 30 μs of the reaction. When proceeding via k_1, A(*t*) quickly forms products which corresponds to the steep and immediate increase in the population of C(*t*). The slow build up and subsequent decay of B(*t*) then results in the long tail of the waveform.

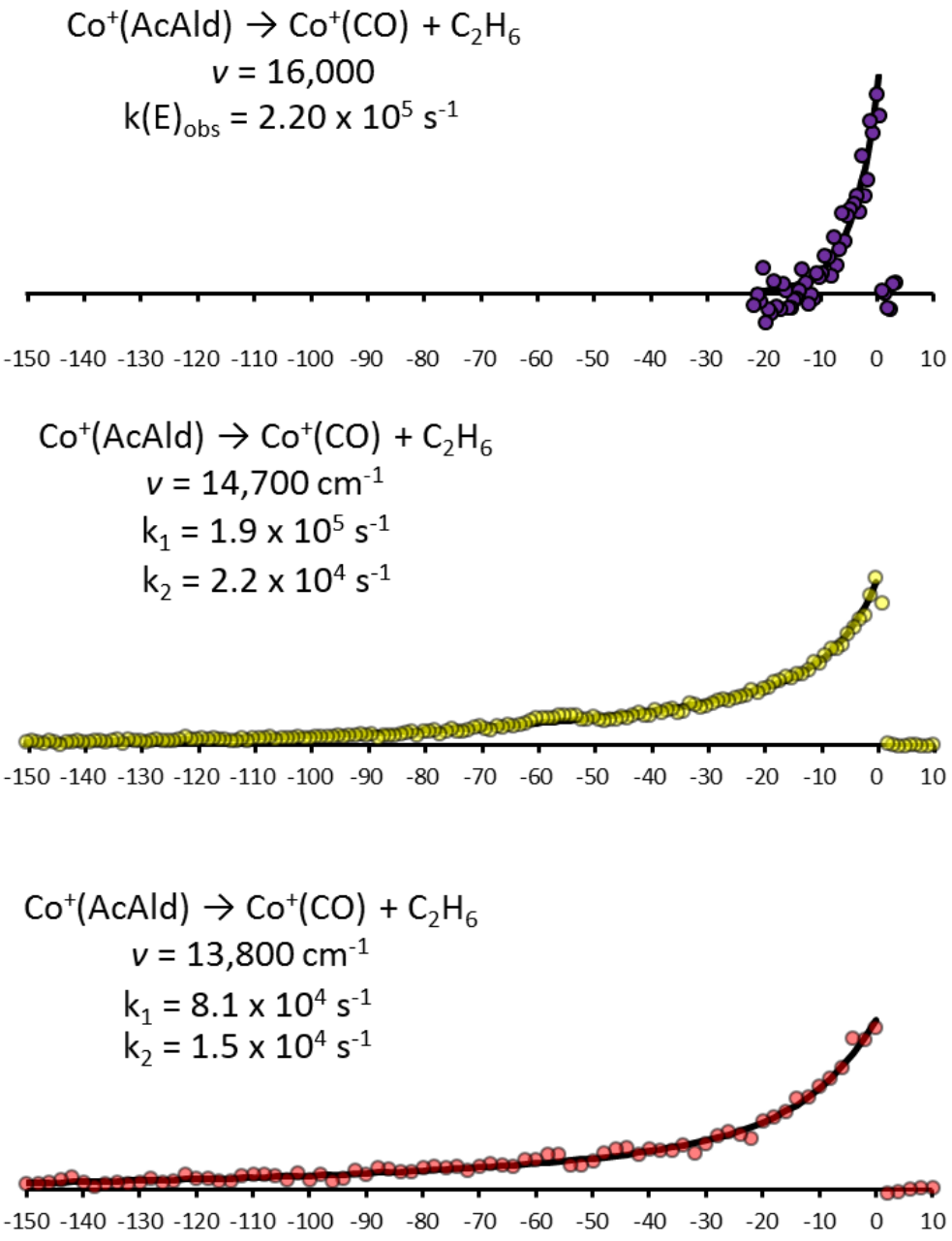

Figure 6.4. SPIDRR waveforms for the production of $Co^+(CO)$ at 16,000 cm^{-1}, 14,700 cm^{-1}, 13,800 cm^{-1}. The upper panel shows the previously measured waveform at 16,000 cm^{-1}. This shows large increase in the activated precursor lifetime at lower energies. Both the middle and lower waveforms show a deviation from single exponential behavior. Both Waveforms have been fit to a biexponetial function. Extracted rates constants are shown in the left corners.

This simple kinetic model does a good job of fitting the data and revealing what type of chemical mechanism may result in the observed behavior. Here it becomes obvious that two competitive pathways are required to produce the biexponential shape. Furthermore, the large difference in lifetimes of the two pathways results from one process being rather facile while the other proceeds through a high energy transition state barrier or requires multiple competitive rearrangement steps to reach products.

It should be noted that a feature is observed at approximately 55 μs which has not been accounted for by the model. It has been observed at various activating photon energies between 15,000 cm^{-1} and 13,800 cm^{-1} and during multiple experimental days both before and after alignment of the activation laser. This subtle feature can only be resolved when exceptional signal to noise is achieved and likely results from the unique reaction dynamics of the system. Though no obvious energy dependence is observed, the slow portion of the scan also does not change appreciably over the measured energy range. In order to reproduce this behavior, a more rigorous kinetic model will likely need to be applied.

As previously stated, initial calculations were performed in order to help understand the dynamics of this system. Initially, calculations were performed to provide the necessary vibrational data to use to carry out RRKM calculations. The surface calculated for this study shown in Figure 6.6. The potential surface is unable to explain the experimental data. Calculations indicate that formation of the observed $Co^+(CO)$ species should not occur via C-H activation. Instead, this activation pathway progresses to an intermediate which leads back to the encounter complex geometry.

Dynamic trajectory calculations indicated that a small portion of highly energized precursors may be able to reach products from this intermediate. However, this would only lead to a small fraction of products proceeding through this secondary path. Were this to occur, the relative intensities of fast and slow portions of the waveform would be very different.

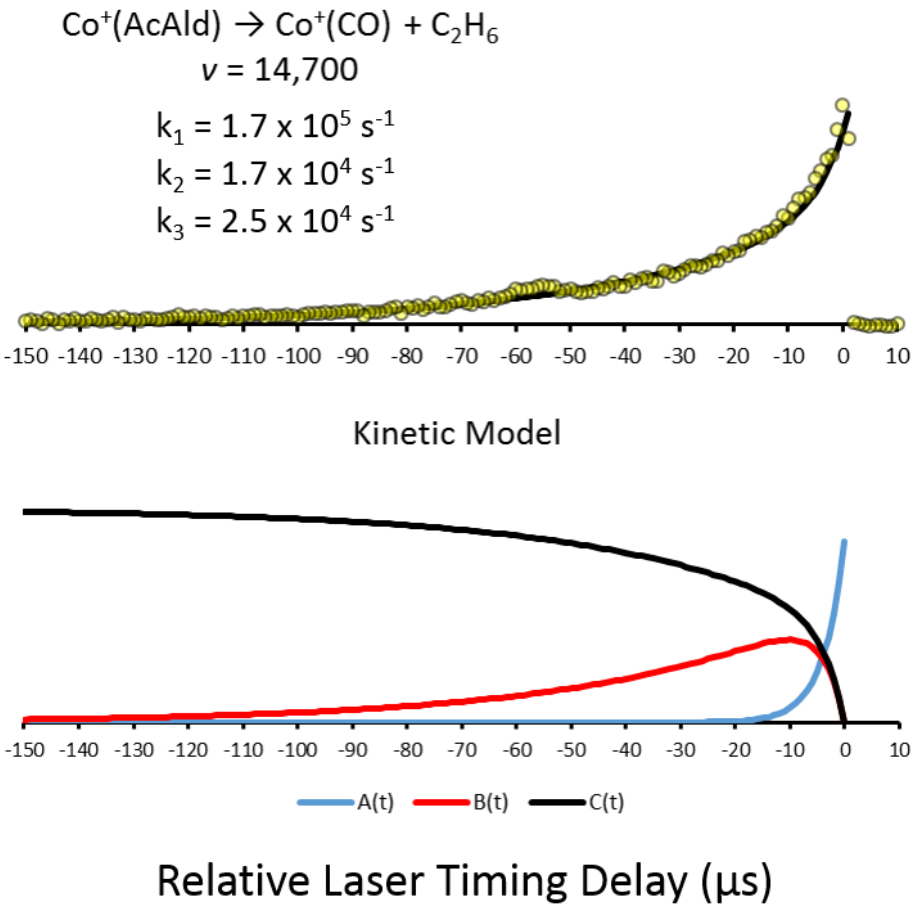

Figure 6.5. The simple kinetic model shown in Scheme 1 applied to the Co^+(AcAld) SPIDRR wave form at an activating photon energy of 14,700 cm^{-1}. The lower panel shows the time dependent population of the activated precursor A (red), the intermediate B (blue) and the product C (black). The upper panel shows the fit of C(t) the SPIDRR waveform when it is constructed to reflect sampling by the SPIDRR apparatus.

Both surfaces also predict rearrangement barriers in excess of 19,000 cm^{-1}. This is well above the photon energies used in this study and shows that these theoretical

methods are not sufficient to describe the absolute rate limiting barrier height for this decomposition reaction. It has been shown previously however that relative energetics and nuclear configurations may still be adequate despite inconsistencies with the activation requirements.[26]

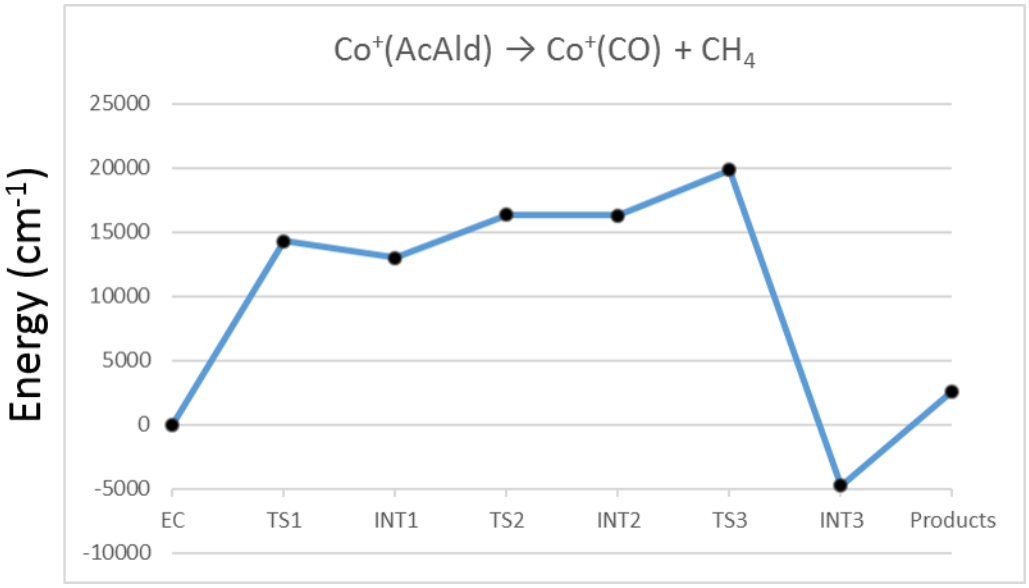

Figure 6.6 The potential energy surface for $Co^+(AcAld) \rightarrow Co^+(CO) + CH_4$ proceeding through C-C activation calculated with DFT UwB97xD/Def2SVPP. The calculations in this study are in good agreement with those reported by Zhao and co-workers. Also consistent with these results was the inability to locate a transition state leading to the observed products via C-H activation. EC denotes the encounter complex cluster, while TS and INT respectively represent various transition states and intermediates along the reaction coordinate.

An examination of the predicted rate limiting transition state reveals an orbiting hydrogen migration similar to that reported in the Ni^+ assisted decomposition of ethyl acetate. This large hydrogen motion makes tunneling a possible candidate to explain the energy invariant slow process observed at energies below 15,700 cm^{-1}. A comparison of $Co^+(AcAld)$ with its d_4 labeled isotopologue would determine if this is the case. If the slow decay process results from a hydrogen tunneling event, the deuterium labeled

species would either cause a drastic kinetic isotope effect or completely prevent the reaction proceeding through this pathway. This explanation however does not account for the fast process described by the kinetic model used in Figure 6.5. It is tempting to ascribe this simply to a hydrogen atom traversing the classical rearrangement barrier. However, if the activated precursor has sufficient energy to surmount the classical activation barrier, tunneling contributions should be negligible.

	k	k_1	k_2
16,000 cm^{-1}	22	-	-
15,800 cm^{-1}	19.3	-	-
15,700 cm^{-1}	13.1	-	-
14,700 cm^{-1}	-	19	2.2
14,500 cm^{-1}	-	15	1.9
13,800 cm^{-1}	-	8.1	1.5

Figure 6.7. Rate constants (x 10^4 s^{-1}) for the Co^+ assisted decomposition of acetaldehyde. Rate constants from 16,000 cm^{-1} to 15,700 cm^{-1} are extracted using a single exponential fit. Rate constants from 14,700 cm^{-1} to 13,800 cm^{-1} are extracted using a biexponential function.

Future analysis of this decomposition reaction should also include a theoretical investigation of the quintet excited state surface. As stated previously, the relative density of available excited electronic states could allow activated precursors to proceed on an excited surface before returning to the ground state and reaching products. The higher spin configuration of the quintet surface may result in lower energy rearrangement barriers accessible via spin inversion through the course of reaction. In this case, reaction

involving a spin inversion to the quintet surface may be competitive with the reaction proceeding only along the ground state triplet surface. Parallel competitive reaction coordinates leading to the same products may explain the biexponential behavior seen in the SPIDRR waveforms.

Conclusions

A unique SPIDRR kinetic signature has been observed at lower activating energies for the Cobalt(I) assisted decomposition of acetaldehyde. The extracted rate constants are listed in Figure 6.7. If RRKM well describes the energy dependence of the microcanonical rate constant at energies above 15,700 cm^{-1}. It is difficult to assess the validity of RRKM below this energy based on the biexponential character of the waveforms below this energy. Though k_1 appears to scale with the calculated RRKM fit of k, the reaction is still observed well below the activation energy predicted by RRKM. Only one transition state has been located which leads to the observed products. This makes it difficult to make RRKM predictions based on k_2. The development of a simple kinetic model shows that the complex nature of the observed waveform is results from competitive activation of two parallel reaction pathways. One of these pathways will be facile and short lived while the other results in a build and subsequently slow decay of at least one intermediate species. A hydrogen tunneling event may result in the long-lived decay process. Measuring the decay kinetics for Co^+(d_4-AcAld) will indicate if this is the case. Parallel competitive reaction pathways may also result from spin crossings on to the quintet electronic surface through the course of the reaction. This possibility was previously suggested in a SPIDRR study of Co^+(acetone) decomposition. Continued

theoretical investigation of the quintet surface is required to determine if this process is likely to occur.

CHAPTER SEVEN

Investigation of TiO^+ as an Isoelectronic Mimic of the Nickel(I) Cation

Introduction

Late transition metals catalyze chemical reactions of invaluable economic and environmental importance. Of particular significance is the platinum group metals which find use in pollution control devices (catalytic converters), fuel cells, and anti-cancer drugs.[118-122] Figure 7.1 provides the percent relative crustal abundances of the period 6 transition metals.[123-125] The early metals in this group, primarily hafnium, tantalum, and tungsten; are in far greater abundance within earth's crust than their heavier counterparts, constituting more than 90% of the available group 6 transition metals.

The hypothesis driving this research is that molecular clusters displaying similar electronic structures to the group 10 atomic transition metals will react in similar fashion, thereby serving as potential replacements. Desired catalytic properties may be attained by combinations of atoms that, when bonded together, acquire an isoelectronic distribution with the precious metal active site. This concept can be extended to tailoring desired properties into a catalyst by modifying the cluster composition (and consequently its electronic structure) with the goal of using such clusters as building blocks to generate nanoscale sized catalysts. Such a premise has been clearly demonstrated by the Castleman group in their photo-electron and reactivity studies of anionic cluster molecules such as TiO^-, WC^- , ZrO^-, and ZrO_2^- which are respectively mimics to Ni^- , Pt^- , Pd^- , and PdO^- ; and are so-called "superatoms."[126-129]

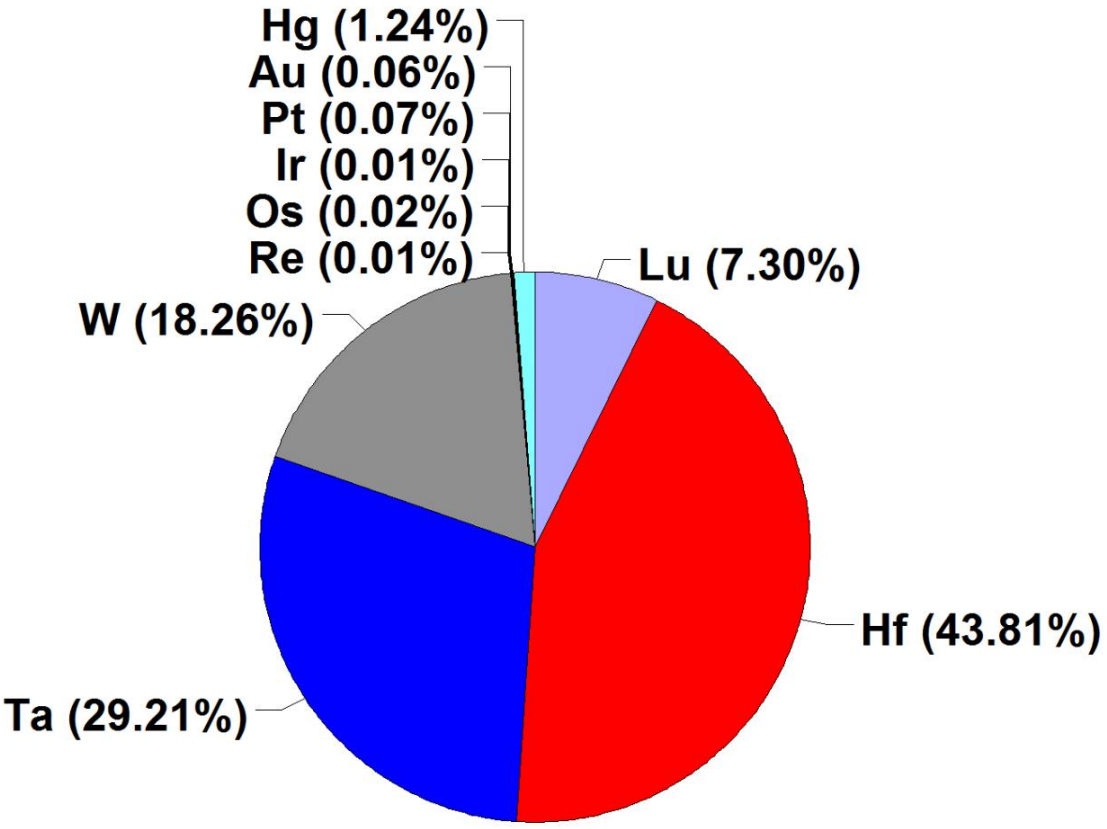

Figure 7.1. Percent relative abundances of period 6 transition metals in Earth's crust. The summed total of these elements is 6.85 ppm by mass.

Experimental

TiO^+ is being studied for the comparison to existing data for Ni^+, its late transition metal counterpart. The high bond energy of TiO^+ (6.88 eV) makes study via photodissociative methods difficult. The electronic structure therefore investigated with resonance-enhanced photodissociation (REPD) using a minimally invasive tagging atom, Ar. A similar study by Metz proved successful by tagging with TiO^+ with CO_2.[130] The weaker binding interaction of argon versus CO_2 should have cause a smaller pertubation on the electronic structure of TiO^+ and allow for an analysis that more closely resembles the electronic structure of TiO^+. $TiO^+(Ar)$ is generated by seeding a helium carrier gas with N_2O passing the gas over a laser ablated titanium rod to form TiO. Argon is added to

produce the tagged species. The molecules are skimmed after supersonic expansion yielding a cold molecular beam. A YAG pumped dye laser is frequency scanned to initiate photodissociation. Simultaneous monitoring of the TiO^+ fragment generates an action spectrum.

Results

Previous experiments have shown 3% N_2O to be sufficient for the production of TiO^+. A mixture of 3%, Ar, 3% N_2O and 94% He resulted in the top panel of Figure 7.2. N_2O and Argon concentrations were reduced to minimize titanium formation of TiO_2^+ and maximize TiO^+(Ar) production respectively. The bottom panel in Figure 7.2 shows TiO^+(Ar) generation under optimal conditions. It is important to note that formation of larger clusters has been reduced, the ratio of TiO^+ to TiO_2^+ has changed and generation of TiO^+(Ar) has increased.

A portion of the REPD spectra has been measured for $^{47}TiO^+$(Ar), ^{48}TiO+(Ar), and $^{49}TiO^+$(Ar). Low signal to noise makes assignment challenging, however there appear to be 4-5 peaks. The two largest of these show clear isotopic shifts. The spacing between major peaks in these spectra is approximately 975 cm^{-1} apart. This energy spacing agrees well with the Ti-O^+ stretching assignment reported by Metz's study of $TiO^+(CO_2)$.[130] A more resolved photodissociation spectrum was used for a tentative assignment of a low frequency TiO^+-L rock (58 cm^{-1}) and stretch (120 cm^{-1}).

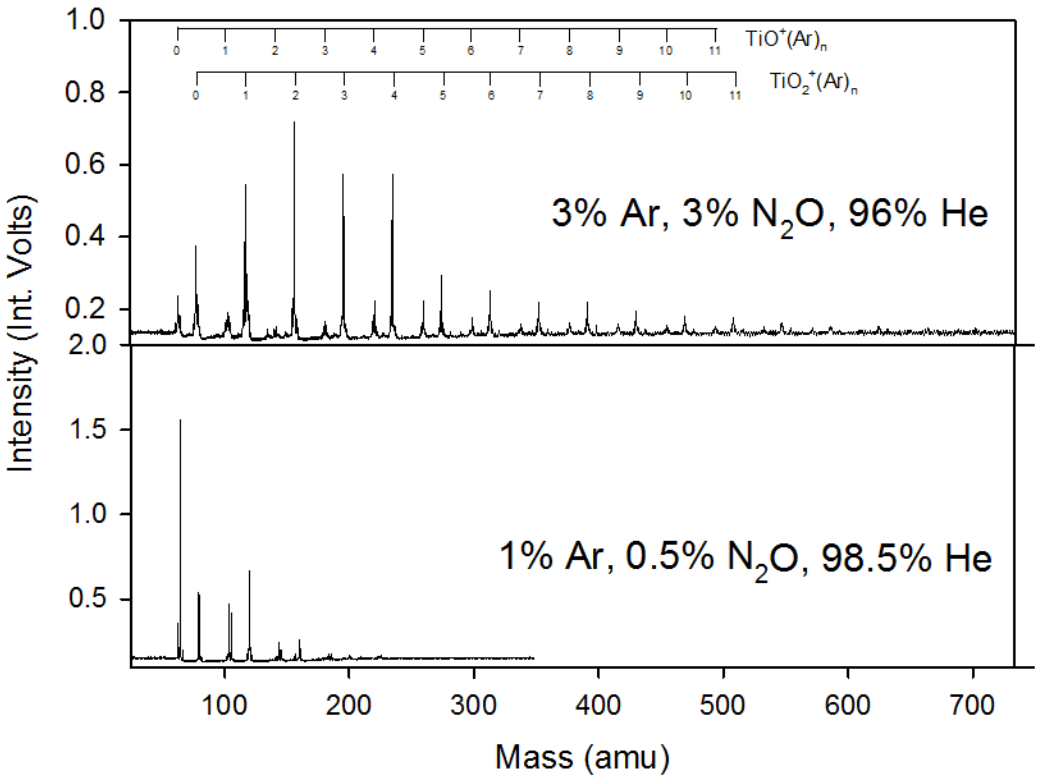

Figure 7.2. Two Time of Flight Mass spectra corresponding to the generation of Argon tagged TiO^+ clusters. The upper panel shows initial experiments using 3 percent Argon which yield argon tagged species up n=17. The lower panel shows an optimized mixture using only 1 percent argon. Formation of relatively more TiO^+ compared to TiO_2^+ was achieved by lowering the N_2O concentration.

Simultaneous measurement of the ^{47}Ti and ^{49}Ti isotopomers are used to assign vibrational quantum numbers. The rather small isotopic shift of the band at 655 nm suggests this is the TiO^+ chromophore electronic origin. A tentative assignment of $v'(TiO^+) = 0$ and 1 is indicated in Figure 7.3. These assignments are also supported by preliminary time dependent density functional theory calculations. These results are shown in Figure 7.4.

Figure 7.5 shows the mass spectra acquired corresponding to generation of the TiO^+(acetone) cluster. The helium expansion gas is doped with three percent N_2O to facilitate the formation of TiO^+ over the bare titanium cation.

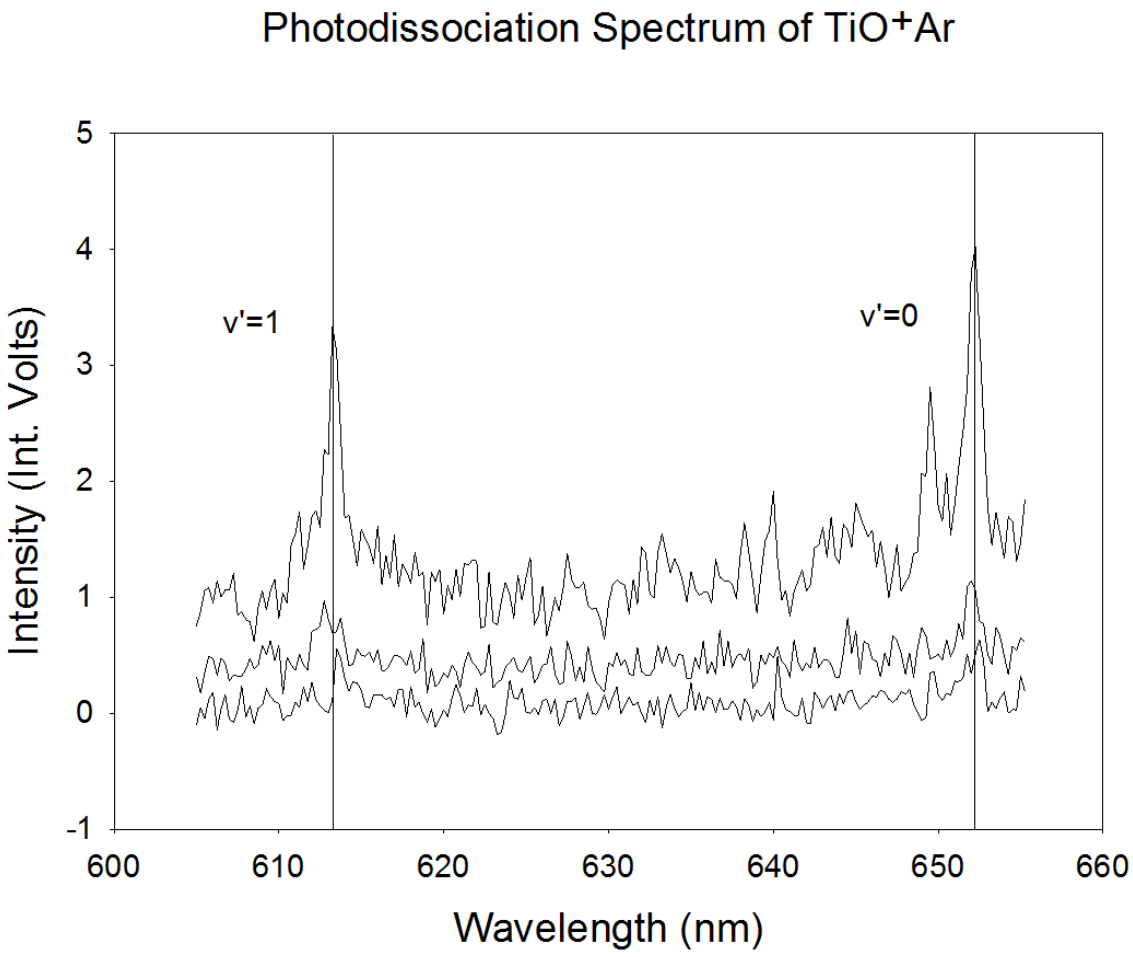

Figure 7.3. A portion of the REPD spectra for three isotopes of $TiO^+(Ar)$.

	Ti-O stretch	TiO-L Stretch	TiO-L rock
$TiO^+(CO_2)$[a]	950 cm^{-1}	186 cm^{-1}	45 cm^{-1}
$TiO^+(Ar)$[b]	975 cm^{-1}	129 cm^{-1}	58 cm^{-1}

Figure 7.4. Comparison of $TiO^+(CO_2)$ vibrational motion energies with tentative $TiO^+(Ar)$ energies. (a- Ref [130]. b- This work).

Figure 7.7 shows a comparison of acetone decomposition mediated by Ni^+ in the top panel and the proposed superatom analogue TiO^+ in the lower panel. The extracted rate constants from each fit are displayed in Figure 7.6. The two reactions clearly proceed

at different rates while also having very different characteristic decay waveforms. Though this makes it difficult to compare the isoelectronic pair, it is unsurprising given that each reaction decomposes into distinctly different products.

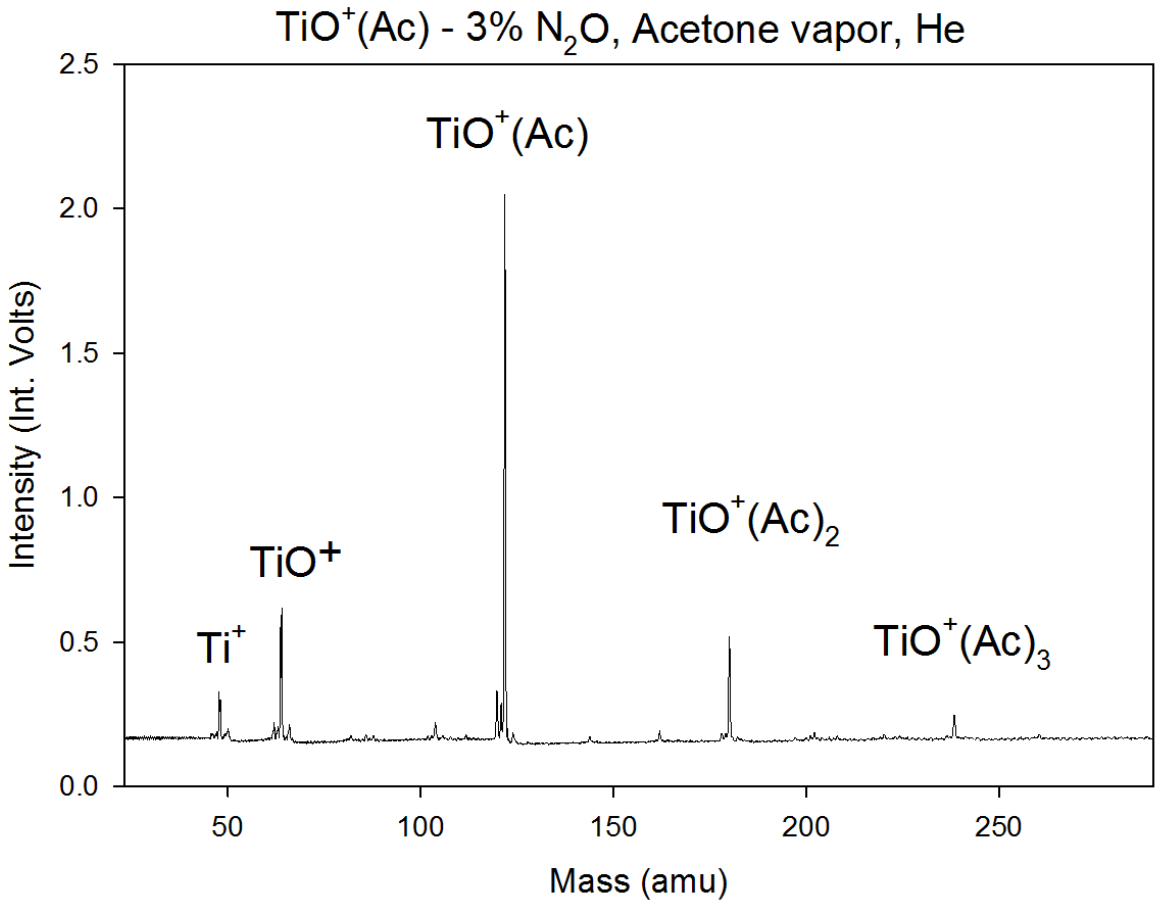

Figure 7.5. Mass spectrum for the generation of TiO^+(Acetone).

The reported microcanonical rate constant for Ni^+(acetone) decomposition at this energy is (1.13 ± .05) x 10^5 s^{-1}.[16] A slower extracted rate constant of (5.5 ± .4) x 10^4 s^{-1} for TiO^+ mediated decomposition initially appears to be quite slow considering that TiO^+ → TiO_2^+ should only require a simple oxygen abstraction.

	Internal Energy	Rate Constant
$Ni^+(Ac)^a$	18,800 cm^{-1}	11.7 ± 0.8
$TiO^+(Ac)^b$	18,800 cm^{-1}	5.5 ± 0.4

Figure 7.6.Rate constants (x 10^4 s^{-1}) for $Ni^+(Ac)$ and $TiO^+(Ac)$ at comparable internal energy. (a- Ref [15]. b-This work).

Closer inspection of the reaction products reveals that a more complex mechanism is likely responsible. To form the propene fragment, the carbon oxygen double bond must be broken, a hydrogen migration must occur from a methyl group onto the central carbon atom while a carbon carbon double bond is formed in the process. The rate limiting behavior then is not simply a result of direct oxygen abstraction, but a multi-step rearrangement process to generate thermodynamically stable products. A study of d_6 acetone will indicate where the rate limiting step occurs. A large kinetic isotope effect would suggest that the hydrogen migration event is responsible for the slow decay. However, no observation of a kinetic isotope effect would suggest that the breaking of the C=O bond controls the reaction rate.

Continued Work

The electronic spectrum of neon in a optogalvanic lamp has been taken in tandem with the REPD spectrum in order to calibrate the energies of observed $TiO^+(Ar)$ transitions. The lower energy side of the collected spectrum must be investigated to ensure the predicted peak at 655nm is the band origin. The high energy side will be

examined to ensure the entire spectrum is gathered. Spectra with better signal to noise will be generated following concentration optimization of the doped carrier gas.

Dependence of the TiO^+(Ac) rate constant with respect to internal energy will be determined by monitoring the kinetics over a range of laser frequencies. This will allow a more through comparison between the rare metal ion and its superatom analogue.

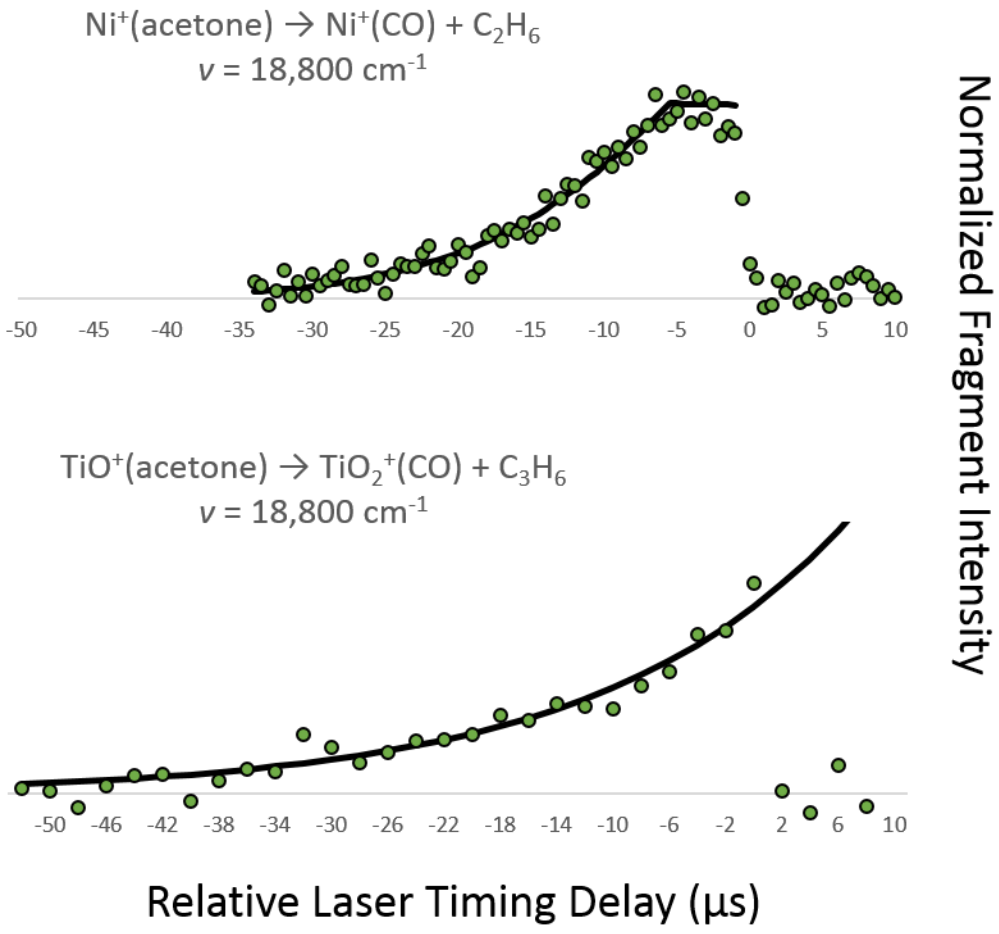

Figure 7.7. Ni^+(acetone) decomposition into Ni^+(CO) in the upper panel is compared with production of TiO_2^+ daughter from TiO^+(Acetone) in the lower panel, both at activating photon energies of 18,800 cm^{-1}. The different decomposition products indicate that each species occur via different mechanisms, preventing a direct comparison.

CHAPTER EIGHT

Conclusions

SPIDRR has been used to examine the kinetic dependence and dynamic behavior of multiple transition metal cations on several functionally different organic fragments. In the Ni^+ assisted decomposition of propionaldehyde, the use of SPIDRR in concert with RRKM and DFT was used to explain a unique energy dependence of the rate limiting microcanonical rate constant through the progression of two parallel competitive reaction pathways. This allowed threshold energies of 14,350 ± 600 cm^{-1} and 15,400 ± 600 cm^{-1} to be determined for C-C and C-H bond activation respectively. UCCSD(T)/def2-TZVP//PBEPBE/cc-VDZ was used to calculate the potential energy surface for the reaction. Despite the disagreement on the absolute energy of the rate limiting barriers, good agreement was found with the relative energies between C-C and C-H activation. The rate limiting steps were identified in each case to be addition to the second sigma bond following initial activation of either the C-C or C-H bonds.

The Ni^+ mediated decomposition of ethyl acetate revealed a complex reaction manifold. Though activation was only predicted to occur through C-O bond insertion, five different exit channels were detected via SPIDRR. The extracted microcanonical rate constants for each exit channel show a close kinetic competition between the fragments. Product branching indicates that insertion into the C-O bond nearest the ketone should provide the lowest energy path to product formation which agrees with theory. This reaction pathway also revealed a unique hydrogen transfer step in which the hydrogen

atom appears to “leap” over the nickel center while in the process losing electron density. Theory also predicts that each reaction must proceed through a hydrogen transfer step before reaching products.

SPIDRR measurements were also used to report rate limiting microcanonical rate constants for three exit channels in the Ni^+ mediated decomposition of diethyl ether at 16,000 cm^{-1}. Strong agreement of the extracted rate constants for two of these channels revealed that production of Ni^+(ethanol) and Ni^+(ethene) proceed through a common rate limiting step. The third decomposition fragment was determined to be the bare oxocarbenium fragment $C_4H_9O^+$. Though the fragment is relatively unstable from a thermodynamic perspective, the reaction occurs quickly through activation of a C-H bond directly from the encounter complex geometry. Previously used theoretical methods failed to describe the experimental results leading to the use of MRMP/CC-pVDZ//PBE/CC-pVDZ. This level of theory revealed another “leap frog” type motion of a hydrogen atom in the predicted rate limiting transition state. This indicates that such a hydrogen migration could be a theme in nickel mediated chemistry of small organics.

SPIDRR measurements were then used to explore the chemical kinetics and dynamics of other transition metal cations. Preliminary studies on the Co^+ assisted decomposition of acetaldehyde show interesting behavior at activation energies lower than 15,000 cm^{-1}. Above this, we observe waveforms with a single exponential dependence that are well modeled by RRKM theory. However, measurements below this show a clear bimodal distribution which can be modeled using a simple kinetic model that contains parallel competitive pathways. Theoretical calculations in this study and those previously reported failed to locate two unique transition states which lead to the

observed product. For this reason, it is proposed that the qualitative shape of the observed waveforms below 15,000 cm^{-1} may result from spin inversion to an excited quintet electronic state through the course of the reaction.

Finally, preliminary investigations were also made on the TiO^+, the isolectronic mimic of Ni^+. A portion of the TiO^+(Ar) REPD spectrum was recorded. The use of argon as a tagging species resulted in tentative vibrational assignments which are in good agreement with time dependent density functional theory calculations as well as a CO_2 tagged REPD spectrum previously reported by Metz. Initial kinetic studies were also performed on TiO^+(acetone) for comparison with the SPIDRR studies of Ni^+(acetone). The decomposition of each molecule into distinctly different products makes a direct comparison difficult. However, TiO^+ mediated decomposition of acetone revealed a previously unobserved loss of oxygen from a ketone functionality. The long dissociative rearrangement lifetime of the reaction suggests the simple oxygen abstraction is not at play and the reaction results from a more complex rearrangement process.

The variety in both organic functionality and metal cation species in the above studies is evidence of the broad capabilities of the SPIDRR apparatus. The novel technique has been used to accomplish the difficult task of making quantitative and qualitative measurements of submerged barriers on a potential energy surface. The combination of SPIDRR measurements and theoretical methods revealed complex reaction dynamics occurring through seemingly simple decomposition reactions. Finally, the wealth of data produced by the SPIDRR apparatus was used to evaluate which theoretical methods could correctly model the reaction dynamics of small yet computationally complex molecules. Owing to a high-energy resolution and unique

sampling method, SPIDRR has shown itself to be a valuable compliment to many existing techniques aimed at a better understanding of transition metal catalysis. Though gas phase ion molecule reactions may not reveal exact mechanistic details seen in bulk phase reactions, they often uncover important dynamic themes which govern the development of future catalysts. A continued use of this novel gas phase method will no doubt prove to be invaluable in constructing a complete understanding of these experimentally tractable models for bulk phase catalysis.

APPENDIX

APPENDIX

Python Codes used for Data Analysis

The following codes were written to create to expedite the analysis of common data produced through the course of SPIDRR experimentation.

Single Exponential Fitting Function

```
import numpy as np
import matplotlib.pyplot as plt
import scipy as sp
import scipy.stats as st
import os.path as path

'''Raw data file and scan wavelength are prompted'''

filename = input ('please input the filename')
raw = np.genfromtxt(filename)
wavelength = input('Please Enter the laser wavelength for this scan')
'''The user will input the data channel of interest for the scan'''

ch = int(input('What data channel would you like to analyze?')) + 3

array = np.loadtxt(filename, delimiter = '\t', usecols = (2,ch))

sv = raw[15,1]

print(array)

'''
An array of that channel will be plotted so the user can define the baseline
range via mouse click
'''
'''Mouse click to store coordinantes'''

def onclick(event):
    global ix,iy
    ix,iy = event.xdata, event.ydata
```

```
    '''Assign global variable to access outside of function'''

    global bcoord
    bcoord.append((ix,iy))

    '''Disconnect after two clicks'''

    if len(bcoord) == 2:
        fig.canvas.mpl_disconnect(bid)
        plt.close(1)
    return

fig = plt.figure(1)
ax1 = plt.subplot2grid((1,1), (0,0))


ax1.plot(array[:,0], array[:,1] * (-1), ) #label = 'SV =' + str(sv))
#for label in ax1.xaxis.get_ticklabels():
#    label.set_rotation(45)


ax1.grid = True
#ax1.xaxis.label.set_color('c')
#ax1.yaxis.label.set_color('c')
#ax1.set_yticks([0,5,10,15])


plt.xlabel('Experimental Time')
plt.ylabel('Integrated Counts')
plt.legend()
plt.title(str(filename) + ' SV= ' + str(sv) + str(wavelength) + ' nm')
#plt.subplots_adjust(left = 0.09, bottom = 0.16, right = 0.94, top = 0.95,
#          wspace = 0.2, hspace = 0)


bcoord = []

'''Call click function'''
bid = fig.canvas.mpl_connect('button_press_event', onclick)

plt.show(1)

bxy = (np.column_stack((np.asarray(bcoord[0]) , np.asarray(bcoord[1]))))[0,:]

print(bxy)
```

```
bx1 = np.argmin((np.abs(array[:,0]-bxy[0])))

bx2 = np.argmin((np.abs(array[:,0]-bxy[1])))

baseline = np.average(array[bx1:bx2,1])


ai = -1*(array[:,1] - baseline)

print(array[bx1:bx2,1])

print(bx1,bx2)

print(baseline)

'''This is the same mouse event code to define the limits for the regression'''

def onclick(event):
    global rx,ry
    rx,ry = event.xdata, event.ydata

    '''Assign global variable to access outside of function'''

    global rcoord
    rcoord.append((rx,ry))

    '''Disconnect after two clicks'''

    if len(rcoord) == 2:
        fig.canvas.mpl_disconnect(rid)
        plt.close(1)
    return

fig = plt.figure(1)
ax1 = plt.subplot2grid((1,1), (0,0))


ax1.plot(array[:,0], array[:,1] * (-1)) #label = 'SV =' + str(int(raw[15,1])))
for label in ax1.xaxis.get_ticklabels():
    label.set_rotation(45)


ax1.grid = True
#ax1.xaxis.label.set_color('c')
#ax1.yaxis.label.set_color('c')
#ax1.set_yticks([0,5,10,15])
```

```
plt.xlabel('Experimental Time')
plt.ylabel('Integrated Counts')
plt.legend()
plt.title(str(filename)+ ' SV= ' + str(sv) + str(wavelength) + ' nm')
#plt.subplots_adjust(left = 0.09, bottom = 0.16, right = 0.94, top = 0.95,
#          wspace = 0.2, hspace = 0)


rcoord = []

'''Call click function'''
rid = fig.canvas.mpl_connect('button_press_event', onclick)

plt.show(1)

rxy = (np.column_stack((np.asarray(rcoord[0]) , np.asarray(rcoord[1]))))[0,:]

print(rxy)

rx1 = np.argmin((np.abs(array[:,0]-rxy[0])))

rx2 = np.argmin((np.abs(array[:,0]-rxy[1])))

at = (array[rx1,0]- array[:,0])*-1

lni = np.ma.log(ai)

print(ai)
print(rx1)
print(rx2)

adjrawint = -1 * (raw[:,ch] - baseline)

print(adjrawint)

linreg = st.linregress(at[rx1:rx2], lni[rx1:rx2])

print(linreg)
print('skjdfhk;bsfhd;hbjjfhb')
clni = linreg[0] * at + linreg[1]
ci = sp.exp(clni)


regplot = np.column_stack([at,lni,clni])
fitplot = np.column_stack([at,ai,ci])
```

```
'''
print(fitplot.shape)
print(path.splitext(fitplot.shape)[0])
'''

print('rate constant =  ' + str(linreg[0]) + '+/-' + str(linreg[4]))
print('r squared =  ' + str(linreg[2]))

'''
plt.figure(1)
plt.subplot(211)
plt.plot(regplot[rx1:rx2,0], regplot[rx1:rx2,1], 'bs')
plt.plot(regplot[rx1:rx2,0], regplot[rx1:rx2,2], 'r', linewidth = 2.0)
plt.xlim(at[rx2] - 2, at[rx1] + 2)
plt.ylabel('Ln Intensity')
plt.title(filename + ' Ch - ' + str(ch - 3) + ' SV - ' + str(sv) + ' ' + wavelength
   + ' nm ')
'''

#plt.subplot(212)
plt.figure(1)
plt.plot(fitplot[:,0], fitplot[:,1], 'o', color = 'blue', markersize = 8)
plt.plot(fitplot[rx1:,0], fitplot[rx1:,2], 'r', linewidth = 4.0, ls = 'dashed')
plt.ylabel('Adj. Intensity', fontsize = 32)
plt.xlabel('Relative Time', fontsize = 32)
plt.title('Ni$^+$Ether -> C$_4$H$_9$O$^+$ \n  Kinetic Scan 625nm', fontsize = 32)
plt.show()

'''
file_base_name = path.splitext(filename)[0]
np.savetxt(file_base_name + '_reg.csv', fitplot, delimiter='  ')
'''
```

```
from scipy.optimize import curve_fit
import sys
import numpy as np
import matplotlib.pyplot as plt
plt.style.use("ggplot")

filename = str (input ('please enter the filename'))
channel = int (input ('what channel would you like to analyze?'))
SV = int (input ('What is the sector voltage of the peak to be fit?'))

'''
try:
   filename = str(sys.argv[1])
except:
   raise AttributeError("Must provide a filename, dummy!")

try:
   SV = int(sys.argv[2])
except:
   SV = 550

'''
# Load data from a file named "data"
array = np.genfromtxt(filename)

# Create x and y data from array slices
x = array[:, 2]
y = array[:, (channel + 3)]

# Define Gaussian function
def gaussian(x,a,x0,sigma):
   return a*np.exp(-(x-x0)**2/(2*sigma**2))

# Fit Gaussian with initialized guess (Amplitude, central SV, width)
guess = [-10, SV, 1]
popt,pcov = curve_fit(gaussian,x,y,p0=guess)

# Plot results
plt.figure(2)
plt.title(r'SV = '+str(popt[1])+r', $\sigma = $'+str(popt[2]) + ', Amp = ' + str(popt[0]))
plt.plot(x, y, color='black', label='Raw')
plt.plot(x, gaussian(x, *popt), color='red', linewidth=3, alpha=0.5, label='Fit')
plt.legend()
plt.show()
```

```
import matplotlib.pyplot as plt
import numpy as np

'''
        LID gaussian fit parameters


        The first term is amplitude, the second is the gaussian x offset and
        the third is the width chi
'''

a = np.asarray((1, 1, 1))
b = np.asarray((1, 1, 1))
c = np.asarray((1, 1, 1))
d = np.asarray((1, 1, 1))
dd = np.asarray((1, 1, 1))

svlid = np.column_stack((a,b,c,d,dd))

lidraw = np.genfromtxt('031718c_SV.txt')
'''
User Must hardcode the gaussian parameters from each peak
into the above and below arrays : a,b,c,d,dd and e,f,g,h,i

The correct file name for the CID baseline is entered into
the cidraw array (line 52)

The correct file name for the lid scan is entered into
the lidraw array (line 20)

The program accomadates up to five peaks. If you have less
 than this simply leave '1' for each pararmeter in both
 the cid and lid peak. This will sum to zero and give you
 a straight line

 At the bottom you will need to chnage the file poutput name in
 line 142 to whatever is appropriate for your use.
'''
print(svlid.shape)
print(svlid)

'''
        CID fit parameters
'''
```

```
e = np.asarray((1, 1, 1))
f = np.asarray((1, 1, 1))
g = np.asarray((1, 1, 1))
h = np.asarray((1, 1, 1))
i = np.asarray((1, 1, 1))

svcid = np.column_stack((e,f,g,h,i))

cidraw = np.genfromtxt('031718d_SV.txt')



print(cidraw.shape)
print(cidraw)

x = cidraw[:, 2]
#y = cidraw[:, 3]

def gaussian(x,a,x0,sigma):
   return a*np.exp(-(x-x0)**2/(2*sigma**2))

#cidfit = gaussian(x,svcid[2,0], svcid[0,0], svcid[1,0])

#lidfit = np.sum([gaussian(x, *svlid[:,i])
#               for i in range(4)], axis = 0)

#cidfit = np.sum([gaussian(x, *svcid[:,i])
#               for i in range(4)], axis = 1)

cg0 = gaussian(x, *svcid[:,0])
cg1 = gaussian(x, *svcid[:,1])
cg2 = gaussian(x, *svcid[:,2])
cg3 = gaussian(x, *svcid[:,3])
cg4 = gaussian(x, *svcid[:,4])

csum = ((cg0 + cg1 + cg2 + cg3 + cg4))

lg0 = gaussian(x, *svlid[:,0])
lg1 = gaussian(x, *svlid[:,1])
lg2 = gaussian(x, *svlid[:,2])
lg3 = gaussian(x, *svlid[:,3])
lg4 = gaussian(x, *svlid[:,4])

lsum = ((lg0 + lg1 + lg2 + lg3 + lg4))

#print(cidfit)
```

```
'''
plt.figure(1)
plt.subplot(211)
plt.plot(lidraw[:,2], lidraw[:,3] * -1, 'o', color = 'blue', markersize = 10)
plt.plot(lidraw[:,2], lsum[:], color = 'r', linewidth = 4.0)
plt.xlim(260, 700)
plt.ylim(-.5,8)
plt.ylabel('LID',fontsize = 40)
plt.text(635,3,'Ni$^+$EtOEt', fontsize = 18)
plt.title('Ni$^+$Diethyl Ether Sector Voltage Scan', fontsize = 40)
'''
plt.figure(1)
plt.subplot(211)
plt.plot(lidraw[:,2], lidraw[:,3] * -1, 'o', color = 'blue', markersize = 10)

''' CID Raw was used for the x axis here because the two scans had different
        starting points which raised erros when ploting
'''
plt.plot(cidraw[:,2], lsum[:], color = 'r', linewidth = 4.0)
plt.xlim(250, 750)
plt.ylim(-.5,10)
plt.ylabel('Laser On',fontsize = 32)
#plt.text(635,3,'Ni$^+$EtOEt', fontsize = 18)
plt.title('Ni$^+$Diethyl Ether Sector Voltage Scan', fontsize = 32)

plt.subplot(212)
plt.plot(cidraw[:,2], cidraw[:,3] * -1, 'o' , color = 'blue', markersize = 10)
plt.plot(cidraw[:,2], csum[:], color ='r', linewidth = 4.0)
plt.ylabel('Laser Off', fontsize = 32)
plt.xlabel('SV', fontsize = 32)
plt.xlim(250, 750)
plt.ylim(-.5,10)
plt.show()

sum = lsum - csum
raw = lidraw[:,3] - cidraw[:,3]

plt.plot(cidraw[:,2], raw[:]*-1, 'o', color = 'blue', markersize = 8)
plt.plot(cidraw[:,2], sum[:], color = 'r', linewidth = 2.5)
plt.xlim(320, 620)
plt.ylim(-1)
plt.xlabel('SV', fontsize = 32)
plt.ylabel('Laser Induced \n Signal', fontsize = 32)
plt.title('Ni$^+$Diethyl Ether Sector Voltage Scan', fontsize = 32)
plt.show()
```

```
output_array = np.column_stack((cidraw[:,2], raw[:]*-1, sum[:]))

np.savetxt('031718cd_lid.txt', output_array, delimiter = '\t')
```

REFERENCES

1. Fechete, I.; Wang, Y.; Védrine, J. C., The past, present and future of heterogeneous catalysis. *Catalysis Today* **2012,** *189* (1), 2-27.

2. Roithová, J.; Schröder, D., Selective Activation of Alkanes by Gas-Phase Metal Ions. *Chemical Reviews* **2010,** *110* (2), 1170-1211.

3. Freiser Ben, S., Special Feature: Tutorial Gas-phase Metal Ion Chemistry. *Journal of Mass Spectrometry* **1996,** *31* (7), 703-715.

4. Armentrout, P. B.; Baer, T., Gas-Phase Ion Dynamics and Chemistry. *The Journal of Physical Chemistry* **1996,** *100* (31), 12866-12877.

5. Eller, K.; Schwarz, H., Organometallic chemistry in the gas phase. *Chemical Reviews* **1991,** *91* (6), 1121-1177.

6. Laskin, J.; Lifshitz, C., Kinetic energy release distributions in mass spectrometry. *Journal of Mass Spectrometry* **2001,** *36* (5), 459-478.

7. Rusu, C. N.; Yates, J. T., Defect Sites on TiO2(110). Detection by O2 Photodesorption. *Langmuir* **1997,** *13* (16), 4311-4316.

8. Liu, C.; Peterson, C.; Wilson, A. K., C–O Bond Cleavage of Dimethyl Ether by Transition Metal Ions: A Systematic Study on Catalytic Properties of Metals and Performance of DFT Functionals. *The Journal of Physical Chemistry A* **2013,** *117* (24), 5140-5148.

9. Freiser, B. S., Selected topics in organometallic ion chemistry. *Accounts of Chemical Research* **1994,** *27* (11), 353-360.

10. Armentrout, P. B., Guided ion beam studies of transition metal–ligand thermochemistry. *International Journal of Mass Spectrometry* **2003,** *227* (3), 289-302.

11. Muntean, F.; Armentrout, P. B., Guided ion beam study of collision-induced dissociation dynamics: integral and differential cross sections. *The Journal of Chemical Physics* **2001,** *115* (3), 1213-1228.

12. Böhme, D. K., Experimental studies of positive ion chemistry with flow-tube mass spectrometry: birth, evolution, and achievements in the 20th century. *International Journal of Mass Spectrometry* **2000,** *200* (1), 97-136.

13. Koyanagi, G. K.; Baranov, V. I.; Tanner, S. D.; Bohme, D. K., An inductively coupled plasma/selected-ion flow tube mass spectrometric study of the chemical resolution of isobaric interferences. *Journal of Analytical Atomic Spectrometry* **2000,** *15* (9), 1207-1210.

14. Hierl, P. M.; Friedman, J. F.; Miller, T. M.; Dotan, I.; Menendez-Barreto, M.; Seeley, J. V.; Williamson, J. S.; Dale, F.; Mundis, P. L.; Morris, R. A.; Paulson, J. F.; Viggiano, A. A., Flowing afterglow apparatus for the study of ion–molecule reactions at high temperatures. *Review of Scientific Instruments* **1996,** *67* (6), 2142-2148.

15. Castleberry, V. A.; Dee, S. J.; Villarroel, O. J.; Laboren, I. E.; Frey, S. E.; Bellert, D. J., The Low-Energy Unimolecular Reaction Rate Constants for the Gas Phase, Ni+-Mediated Dissociation of the C−C σ Bond in Acetone. *The Journal of Physical Chemistry A* **2009,** *113* (39), 10417-10424.

16. Dee, S. J.; Castleberry, V. A.; Villarroel, O. J.; Laboren, I. E.; Frey, S. E.; Ashley, D.; Bellert, D. J., Rate-Limiting Step in the Low-Energy Unimolecular Decomposition Reaction of Ni+•Acetone into Ni+CO + Ethane. *The Journal of Physical Chemistry A* **2009,** *113* (51), 14074-14080.

17. Wiley, W. C.; McLaren, I. H., Time-of-Flight Mass Spectrometer with Improved Resolution. *Review of Scientific Instruments* **1955,** *26* (12), 1150-1157.

18. Duncan, M. A., Invited Review Article: Laser vaporization cluster sources. *Review of Scientific Instruments* **2012,** *83* (4), 041101.

19. M. G. Gutierrez, Z. T., T. Lewis, D. J. Bellert, A Molecular Beam Apparatus for Performing Single Photon Initiated Dissociative Rearrangement Reactions (SPIDRR) with Transition Metal Cation Bound Organic Clusters. *Review of Scientific Instruments* **2018,** *(Accepted for Publication)*.

20. Assmann, M.; Weinacht, T.; Matsika, S., Surface hopping investigation of the relaxation dynamics in radical cations. *The Journal of Chemical Physics* **2016,** *144* (3), 034301.

21. Dunbar, R. C., Kinetics of Thermal Unimolecular Dissociation by Ambient Infrared Radiation. *The Journal of Physical Chemistry* **1994,** *98* (35), 8705-8712.

22. Dunbar, R. C., What are the slowest metastable-ion decompositions? *International Journal of Mass Spectrometry and Ion Processes* **1983,** *54* (1), 109-118.

23. Castleberry, V.; Dee, J.; Villarroel, O.; Laboren, I.; Bellert, D., Two photon resonant excitation of Copper–Rydberg levels. *Physics Letters A* **2008,** *372* (27), 4805-4808.

24. Lu, W. Y.; Wong, T. H.; Sheng, Y.; Lytle, A. T.; Kleiber, P. D., Photodissociation Spectroscopy of Zn+−Methanol. *The Journal of Physical Chemistry A* **2003,** *107* (7), 984-989.

25. Kramida, A. R., Y.; Reader, J.; NIST ASD Team, Natinal Institute of Standards and Technology: NIST Atomic Spectra Database, 2018.

26. Mansell, A.; Theis, Z.; Gutierrez, M. G.; Faza, O. N.; Lopez, C. S.; Bellert, D. J., Submerged Barriers in the Ni+ Assisted Decomposition of Propionaldehyde. *The Journal of Physical Chemistry A* **2016,** *120* (15), 2275-2284.

27. Donahue, N. M., Reaction Barriers: Origin and Evolution. *Chemical Reviews* **2003,** *103* (12), 4593-4604.

28. Schumacher, N.; Boisen, A.; Dahl, S.; Gokhale, A. A.; Kandoi, S.; Grabow, L. C.; Dumesic, J. A.; Mavrikakis, M.; Chorkendorff, I., Trends in low-temperature water–gas shift reactivity on transition metals. *Journal of Catalysis* **2005,** *229* (2), 265-275.

29. Gates, B. C.; Flytzani-Stephanopoulos, M.; Dixon, D. A.; Katz, A., Atomically dispersed supported metal catalysts: perspectives and suggestions for future research. *Catalysis Science & Technology* **2017,** *7* (19), 4259-4275.

30. Zemski, K. A.; Justes, D. R.; Castleman, A. W., Studies of Metal Oxide Clusters: Elucidating Reactive Sites Responsible for the Activity of Transition Metal Oxide Catalysts. *The Journal of Physical Chemistry B* **2002,** *106* (24), 6136-6148.

31. Božović, A.; Feil, S.; Koyanagi Gregory, K.; Viggiano Albert, A.; Zhang, X.; Schlangen, M.; Schwarz, H.; Bohme Diethard, K., Conversion of Methane to Methanol: Nickel, Palladium, and Platinum (d9) Cations as Catalysts for the Oxidation of Methane by Ozone at Room Temperature. *Chemistry – A European Journal* **2010,** *16* (38), 11605-11610.

32. Schultz, R. H.; Armentrout, P. B., Threshold collisional activation of iron cation-propane (Fe.cntdot.C3H8). Probing the potential energy surface. *Journal of the American Chemical Society* **1991,** *113* (2), 729-730.

33. Haynes, C. L.; Armentrout, P. B., Thermochemistry and Structures of CoC3H6+: Metallacycle and Metal-Alkene Isomers. *Organometallics* **1994,** *13* (9), 3480-3490.

34. Haynes, C. L.; Fisher, E. R.; Armentrout, P. B., Probing the [CoC3H8]+ Potential Energy Surface: A Detailed Guided-Ion Beam Study. *The Journal of Physical Chemistry* **1996,** *100* (47), 18300-18316.

35. Villarroel, O. J.; Laboren, I. E.; Bellert, D. J., Co+-Assisted Decomposition of h6-Acetone and d6-Acetone: Acquisition of Reaction Rate Constants and Dynamics of the Dissociative Mechanism. *The Journal of Physical Chemistry A* **2012,** *116* (12), 3081-3088.

36. Laboren, I. E.; Villarroel, O. J.; Dee, S. J.; Castleberry, V. A.; Klausmeyer, K.; Bellert, D. J., Reaction Rate Constants and Mechanistic Detail of the Ni+ + Butanone Reaction. *The Journal of Physical Chemistry A* **2011,** *115* (10), 1810-1820.

37. Dee, S. J.; Castleberry, V. A.; Villarroel, O. J.; Laboren, I. E.; Bellert, D. J., Low-Energy Reaction Rate Constants for the Ni+-Assisted Decomposition of Acetaldehyde: Observation of C−H and C−C Activation. *The Journal of Physical Chemistry A* **2010,** *114* (4), 1783-1789.

38. Liang, B.; Zhou, M.; Andrews, L., Reactions of Laser-Ablated Ni, Pd, and Pt Atoms with Carbon Monoxide: Matrix Infrared Spectra and Density Functional Calculations on M(CO)n (n = 1−4), M(CO)n- (n = 1−3), and M(CO)n+ (n = 1−2), (M = Ni, Pd, Pt). *The Journal of Physical Chemistry A* **2000,** *104* (17), 3905-3914.

39. Distefano, G., Photoionization Study of $Fe(CO)_5$ and $Ni(CO)_4$. *Journal of Research of the National Bureau os Standards* **1970,** *74A* (2), 233-238.

40. Khan, F. A.; Steele, D. L.; Armentrout, P. B., Ligand Effects in Organometallic Thermochemistry: The Sequential Bond Energies of Ni(CO)x+ and Ni(N2)x+ (x = 1-4) and Ni(NO)x+ (x = 1-3). *The Journal of Physical Chemistry* **1995,** *99* (19), 7819-7828.

41. Tasker, S. Z.; Standley, E. A.; Jamison, T. F., Recent advances in homogeneous nickel catalysis. *Nature* **2014,** *509*, 299.

42. SanMartin, R.; Herrero María, T.; Domínguez, E., New Copper, Palladium and Nickel Catalytic Systems: An Evolution towards More Efficient Procedures. *The Chemical Record* **2016,** *16* (3), 1082-1095.

43. Ananikov, V. P., Nickel: The "Spirited Horse" of Transition Metal Catalysis. *ACS Catalysis* **2015,** *5* (3), 1964-1971.

44. Zhou, W.; Zheng, S.; Schultz, J. W.; Rath, N. P.; Mirica, L. M., Aromatic Cyanoalkylation through Double C–H Activation Mediated by Ni(III). *Journal of the American Chemical Society* **2016,** *138* (18), 5777-5780.

45. Joe Candice, L.; Doyle Abigail, G., Direct Acylation of C(sp3)−H Bonds Enabled by Nickel and Photoredox Catalysis. *Angewandte Chemie International Edition* **2016,** *55* (12), 4040-4043.

46. Fernandez-Salas, J. A.; Marelli, E.; Nolan, S. P., Synthesis of (diarylmethyl)amines using Ni-catalyzed arylation of C(sp3)-H bonds. *Chemical Science* **2015,** *6* (8), 4973-4977.

47. Liu, Y.-J.; Zhang, Z.-Z.; Yan, S.-Y.; Liu, Y.-H.; Shi, B.-F., Ni(ii)/BINOL-catalyzed alkenylation of unactivated C(sp3)-H bonds. *Chemical Communications* **2015,** *51* (37), 7899-7902.

48. Ye, X.; Petersen, J. L.; Shi, X., Nickel-catalyzed directed sulfenylation of sp2 and sp3 C-H bonds. *Chemical Communications* **2015,** *51* (37), 7863-7866.

49. Yan, S.-Y.; Liu, Y.-J.; Liu, B.; Liu, Y.-H.; Zhang, Z.-Z.; Shi, B.-F., Nickel-catalyzed direct thiolation of unactivated C(sp3)-H bonds with disulfides. *Chemical Communications* **2015,** *51* (34), 7341-7344.

50. Moragas, T.; Gaydou, M.; Martin, R., Nickel-Catalyzed Carboxylation of Benzylic C−N Bonds with CO2. *Angewandte Chemie International Edition* **2016,** *55* (16), 5053-5057.

51. Wang, X.; Liu, Y.; Martin, R., Ni-Catalyzed Divergent Cyclization/Carboxylation of Unactivated Primary and Secondary Alkyl Halides with CO2. *Journal of the American Chemical Society* **2015,** *137* (20), 6476-6479.

52. Baker, E. L.; Yamano, M. M.; Zhou, Y.; Anthony, S. M.; Garg, N. K., A two-step approach to achieve secondary amide transamidation enabled by nickel catalysis. *Nature Communications* **2016,** *7*, 11554.

53. Simmons, B. J.; Weires, N. A.; Dander, J. E.; Garg, N. K., Nickel-Catalyzed Alkylation of Amide Derivatives. *ACS Catalysis* **2016,** *6* (5), 3176-3179.

54. Lu, X.; Xiao, B.; Zhang, Z.; Gong, T.; Su, W.; Yi, J.; Fu, Y.; Liu, L., Practical carbon–carbon bond formation from olefins through nickel-catalyzed reductive olefin hydrocarbonation. *Nature Communications* **2016,** *7*, 11129.

55. Ritleng, V.; Henrion, M.; Chetcuti, M. J., Nickel N-Heterocyclic Carbene-Catalyzed C–Heteroatom Bond Formation, Reduction, and Oxidation: Reactions and Mechanistic Aspects. *ACS Catalysis* **2016,** *6* (2), 890-906.

56. Shi, S.; Meng, G.; Szostak, M., Synthesis of Biaryls through Nickel-Catalyzed Suzuki–Miyaura Coupling of Amides by Carbon–Nitrogen Bond Cleavage. *Angewandte Chemie International Edition* **2016,** *55* (24), 6959-6963.

57. Liu, X.; Hsiao, C. C.; Kalvet, I.; Leiendecker, M.; Guo, L.; Schoenebeck, F.; Rueping, M., Lewis Acid Assisted Nickel-Catalyzed Cross-Coupling of Aryl Methyl Ethers by C−O Bond-Cleaving Alkylation: Prevention of Undesired β-Hydride Elimination. *Angewandte Chemie International Edition* **2016,** *55* (20), 6093-6098.

58. Heijnen, D.; Gualtierotti, J. B.; Hornillos, V.; Feringa Ben, L., Nickel-Catalyzed Cross-Coupling of Organolithium Reagents with (Hetero)Aryl Electrophiles. *Chemistry – A European Journal* **2015,** *22* (12), 3991-3995.

59. Cornella, J.; Edwards, J. T.; Qin, T.; Kawamura, S.; Wang, J.; Pan, C.-M.; Gianatassio, R.; Schmidt, M.; Eastgate, M. D.; Baran, P. S., Practical Ni-Catalyzed Aryl–Alkyl Cross-Coupling of Secondary Redox-Active Esters. *Journal of the American Chemical Society* **2016,** *138* (7), 2174-2177.

60. Weires, N. A.; Baker, E. L.; Garg, N. K., Nickel-catalysed Suzuki–Miyaura coupling of amides. *Nature Chemistry* **2015,** *8*, 75.

61. Arendt Kevin, M.; Doyle Abigail, G., Dialkyl Ether Formation by Nickel-Catalyzed Cross-Coupling of Acetals and Aryl Iodides. *Angewandte Chemie International Edition* **2015,** *54* (34), 9876-9880.

62. Grigalunas, M.; Ankner, T.; Norrby, P.-O.; Wiest, O.; Helquist, P., Ni-Catalyzed Alkenylation of Ketone Enolates under Mild Conditions: Catalyst Identification and Optimization. *Journal of the American Chemical Society* **2015,** *137* (22), 7019-7022.

63. Schley, N. D.; Fu, G. C., Nickel-Catalyzed Negishi Arylations of Propargylic Bromides: A Mechanistic Investigation. *Journal of the American Chemical Society* **2014,** *136* (47), 16588-16593.

64. Corcoran, E. B.; Pirnot, M. T.; Lin, S.; Dreher, S. D.; DiRocco, D. A.; Davies, I. W.; Buchwald, S. L.; MacMillan, D. W. C., Aryl amination using ligand-free Ni(II) salts and photoredox catalysis. *Science* **2016,** *353* (6296), 279-283.

65. Oderinde, M. S.; Frenette, M.; Robbins, D. W.; Aquila, B.; Johannes, J. W., Photoredox Mediated Nickel Catalyzed Cross-Coupling of Thiols With Aryl and Heteroaryl Iodides via Thiyl Radicals. *Journal of the American Chemical Society* **2016,** *138* (6), 1760-1763.

66. Zuo, Z.; Cong, H.; Li, W.; Choi, J.; Fu, G. C.; MacMillan, D. W. C., Enantioselective Decarboxylative Arylation of α-Amino Acids via the Merger of Photoredox and Nickel Catalysis. *Journal of the American Chemical Society* **2016,** *138* (6), 1832-1835.

67. Murphy, J. J.; Melchiorre, P., Light opens pathways for nickel catalysis. *Nature* **2015,** *524*, 297.

68. Gutierrez, O.; Tellis, J. C.; Primer, D. N.; Molander, G. A.; Kozlowski, M. C., Nickel-Catalyzed Cross-Coupling of Photoredox-Generated Radicals: Uncovering a General Manifold for Stereoconvergence in Nickel-Catalyzed Cross-Couplings. *Journal of the American Chemical Society* **2015,** *137* (15), 4896-4899.

69. Xu, H.; Diccianni, J. B.; Katigbak, J.; Hu, C.; Zhang, Y.; Diao, T., Bimetallic C–C Bond-Forming Reductive Elimination from Nickel. *Journal of the American Chemical Society* **2016,** *138* (14), 4779-4786.

70. Dyson, P. J.; Jessop, P. G., Solvent effects in catalysis: rational improvements of catalysts via manipulation of solvent interactions. *Catalysis Science & Technology* **2016,** *6* (10), 3302-3316.

71. Proutiere, F.; Schoenebeck, F., Solvent Effect on Palladium-Catalyzed Cross-Coupling Reactions and Implications on the Active Catalytic Species. *Angewandte Chemie International Edition* **2011,** *50* (35), 8192-8195.

72. Oderinde, M. S.; Varela-Alvarez, A.; Aquila, B.; Robbins, D. W.; Johannes, J. W., Effects of Molecular Oxygen, Solvent, and Light on Iridium-Photoredox/Nickel Dual-Catalyzed Cross-Coupling Reactions. *The Journal of Organic Chemistry* **2015,** *80* (15), 7642-7651.

73. Wencel-Delord, J.; Colobert, F., A remarkable solvent effect of fluorinated alcohols on transition metal catalysed C-H functionalizations. *Organic Chemistry Frontiers* **2016,** *3* (3), 394-400.

74. Lavoie, C. M.; MacQueen, P. M.; Rotta-Loria, N. L.; Sawatzky, R. S.; Borzenko, A.; Chisholm, A. J.; Hargreaves, B. K. V.; McDonald, R.; Ferguson, M. J.; Stradiotto, M., Challenging nickel-catalysed amine arylations enabled by tailored ancillary ligand design. *Nature Communications* **2016,** *7*, 11073.

75. Phelps, A. M.; Chan, V. S.; Napolitano, J. G.; Krabbe, S. W.; Schomaker, J. M.; Shekhar, S., Ligand-Controlled Synthesis of Azoles via Ir-Catalyzed Reactions of Sulfoxonium Ylides with 2-Amino Heterocycles. *The Journal of Organic Chemistry* **2016,** *81* (10), 4158-4169.

76. Moragas, T.; Cornella, J.; Martin, R., Ligand-Controlled Regiodivergent Ni-Catalyzed Reductive Carboxylation of Allyl Esters with CO2. *Journal of the American Chemical Society* **2014,** *136* (51), 17702-17705.

77. Liu, J.; Liu, Q.; Franke, R.; Jackstell, R.; Beller, M., Ligand-Controlled Palladium-Catalyzed Alkoxycarbonylation of Allenes: Regioselective Synthesis of α,β- and β,γ-Unsaturated Esters. *Journal of the American Chemical Society* **2015,** *137* (26), 8556-8563.

78. Lee, S. R.; Bloom, J. W. G.; Wheeler, S. E.; McNeil, A. J., Accelerating Ni(ii) precatalyst initiation using reactive ligands and its impact on chain-growth polymerizations. *Dalton Transactions* **2013,** *42* (12), 4218-4222.

79. Ligand, Additive, and Solvent Effects in Palladium Catalysis – Mechanistic Studies En Route to Catalyst Design. In *Understanding Organometallic Reaction Mechanisms and Catalysis*.

80. Jia, M.; Bandini, M., Counterion Effects in Homogeneous Gold Catalysis. *ACS Catalysis* **2015,** *5* (3), 1638-1652.

81. Davies, P. W.; Martin, N., Counterion Effects in a Gold-Catalyzed Synthesis of Pyrroles from Alkynyl Aziridines. *Organic Letters* **2009,** *11* (11), 2293-2296.

82. Antoniotti, S.; Dalla, V.; Duñach, E., Metal Triflimidates: Better than Metal Triflates as Catalysts in Organic Synthesis—The Effect of a Highly Delocalized Counteranion. *Angewandte Chemie International Edition* **2010,** *49* (43), 7860-7888.

83. Bandini, M.; Bottoni, A.; Chiarucci, M.; Cera, G.; Miscione, G. P., Mechanistic Insights into Enantioselective Gold-Catalyzed Allylation of Indoles with Alcohols: The Counterion Effect. *Journal of the American Chemical Society* **2012,** *134* (51), 20690-20700.

84. Kim Ji, H.; Park, S. W.; Park Sae, R.; Lee, S.; Kang Eun, J., Counterion-Mediated Hydrogen-Bonding Effects: Mechanistic Study of Gold(I)-Catalyzed Enantioselective Hydroamination of Allenes. *Chemistry – An Asian Journal* **2011,** *6* (8), 1982-1986.

85. Jia, M.; Cera, G.; Perrotta, D.; Monari, M.; Bandini, M., Taming Gold(I)–Counterion Interplay in the De-aromatization of Indoles with Allenamides. *Chemistry – A European Journal* **2014,** *20* (32), 9875-9878.

86. Ciancaleoni, G.; Belpassi, L.; Zuccaccia, D.; Tarantelli, F.; Belanzoni, P., Counterion Effect in the Reaction Mechanism of NHC Gold(I)-Catalyzed Alkoxylation of Alkynes: Computational Insight into Experiment. *ACS Catalysis* **2015,** *5* (2), 803-814.

87. Zhou, T.; Xu, L.; Xia, Y., Noninnocent Counterion Effect on the Rearrangements of Cationic Intermediates in a Gold(I)-Catalyzed Alkenylsilylation Reaction. *Organic Letters* **2013,** *15* (23), 6074-6077.

88. Armentrout, P. B.; Beauchamp, J. L., The chemistry of atomic transition-metal ions: insight into fundamental aspects of organometallic chemistry. *Accounts of Chemical Research* **1989,** *22* (9), 315-321.

89. Rodgers, M. T.; Armentrout, P. B., Noncovalent metal–ligand bond energies as studied by threshold collision-induced dissociation. *Mass Spectrometry Reviews* **2000,** *19* (4), 215-247.

90. Chen, P., Electrospray Ionization Tandem Mass Spectrometry in High-Throughput Screening of Homogeneous Catalysts. *Angewandte Chemie International Edition* **2003,** *42* (25), 2832-2847.

91. Böhme Diethard, K.; Schwarz, H., Gas-Phase Catalysis by Atomic and Cluster Metal Ions: The Ultimate Single-Site Catalysts. *Angewandte Chemie International Edition* **2005,** *44* (16), 2336-2354.

92. Oeschger, R. J.; Ringger, D. H.; Chen, P., Gas-Phase Investigations on the Transmetalation Step in Sonogashira Reactions. *Organometallics* **2015,** *34* (15), 3888-3892.

93. Zhugralin, A. R.; Kobylianskii, I. J.; Chen, P., Experimental Gas-Phase and in Silico Investigation of β-Methyl Elimination from Cationic Palladium Alkyl Species. *Organometallics* **2015,** *34* (7), 1301-1306.

94. O'Hair Richard, A. J., Gas-phase studies of metal catalyzed decarboxylative cross-coupling reactions of esters. In *Pure and Applied Chemistry*, 2015; Vol. 87, p 391.

95. Vikse, K. L.; Khairallah, G. N.; Ariafard, A.; Canty, A. J.; O'Hair, R. A. J., Gas-Phase and Computational Study of Identical Nickel- and Palladium-Mediated Organic Transformations Where Mechanisms Proceeding via MII or MIV Oxidation States Are Determined by Ancillary Ligands. *Journal of the American Chemical Society* **2015,** *137* (42), 13588-13593.

96. Medeiros, M. J.; Neves, C. S. S.; Pereira, A. R.; Duñach, E., Electroreductive intramolecular cyclisation of bromoalkoxylated derivatives catalysed by nickel(I) tetramethylcyclam in "green" media. *Electrochimica Acta* **2011,** *56* (12), 4498-4503.

97. Esteves Ana, P.; Goken Danielle, M.; Klein Lee, J.; Leite Luis, F. M.; Medeiros Maria, J.; Peters Dennis, G., Electroreductive Radical Cyclization of Ethyl 2-Bromo-3-allyloxy- and-3-(propargyloxy)propanoates Catalyzed by (Tetramethylcyclam)nickel(I) Electrogenerated at Carbon Cathodes in Dimethylformamide. *European Journal of Organic Chemistry* **2005,** *2005* (22), 4852-4859.

98. Esteves, A. P.; Goken, D. M.; Klein, L. J.; Lemos, M. A.; Medeiros, M. J.; Peters, D. G., Electroreductive Intramolecular Cyclization of a Bromo Propargyloxy Ester Catalyzed by Nickel(I) Tetramethylcyclam Electrogenerated at Carbon Cathodes in Dimethylformamide. *The Journal of Organic Chemistry* **2003,** *68* (3), 1024-1029.

99. Min2a was conformationally studied in order to see whether a planetary motion could be found for the hydride ligand; however, this motion is coupled with reversion to Min1a. Ketene complexation via its oxygen atom was also considered, but this isomer was found to lie more than 10 kcal/mol higher in energy, and it is therefore noncompetitive for the chemistry under study.

100. Irigoras, A.; Mercero, J. M.; Silanes, I.; Ugalde, J. M., The Ferrocene−Lithium Cation Complex in the Gas Phase. *Journal of the American Chemical Society* **2001,** *123* (21), 5040-5043.

101. Ortuño Manuel, A.; Vidossich, P.; Conejero, S.; Lledós, A., Orbital-Like Motion of Hydride Ligands around Low-Coordinate Metal Centers. *Angewandte Chemie International Edition* **2014,** *53* (51), 14158-14161.

102. Hohenberg, P.; Kohn, W., Inhomogeneous Electron Gas. *Physical Review* **1964,** *136* (3B), B864-B871.

103. Kohn, W.; Sham, L. J., Self-Consistent Equations Including Exchange and Correlation Effects. *Physical Review* **1965,** *140* (4A), A1133-A1138.

104. Hohenberg, P.; Kohn, W., Inhomogeneous Electron Gas. *Physical Review* **1964,** *136* (3B), B864-B871.

105. Dunning, T. H., Gaussian basis sets for use in correlated molecular calculations. I. The atoms boron through neon and hydrogen. *The Journal of Chemical Physics* **1989,** *90* (2), 1007-1023.

106. Dunning, T. H.; Peterson, K. A.; Wilson, A. K., Gaussian basis sets for use in correlated molecular calculations. X. The atoms aluminum through argon revisited. *The Journal of Chemical Physics* **2001,** *114* (21), 9244-9253.

107. Bauernschmitt, R.; Ahlrichs, R., Stability analysis for solutions of the closed shell Kohn–Sham equation. *The Journal of Chemical Physics* **1996,** *104* (22), 9047-9052.

108. Liu, F.; Zhang, X. G.; Armentrout, P. B., Activation of CH4 by gas-phase Ni+ and the thermochemistry of Ni-ligand complexes. *Physical Chemistry Chemical Physics* **2005,** *7* (5), 1054-1064.

109. Cremer, D., Density functional theory: coverage of dynamic and non-dynamic electron correlation effects. *Molecular Physics* **2001,** *99* (23), 1899-1940.

110. Hoffmann, R.; Schleyer, P. v. R.; Schaefer Henry , F., Predicting Molecules—More Realism, Please! *Angewandte Chemie International Edition* **2008,** *47* (38), 7164-7167.

111. López, R. V.; Faza, O. N.; López, C. S., Accounting for Diradical Character through DFT. The Case of Vinyl Allene Oxide Rearrangement. *The Journal of Organic Chemistry* **2015,** *80* (21), 11206-11211.

112. Frisch, M. J. *Gaussian 09 Revision C.1*, Gaussian Inc.: Wallingford CT, 2009.

113. Keith, T. A. *AIMall (version 14.11.23)*, TK Gristmill Software: Overland Park KS, 2014.

114. Silva López, C.; Faza, O. N.; Mansell, A.; Theis, Z.; Bellert, D., Three Reaction Channels with Signature Proton Transfers in the Ni(I)-Catalyzed Decomposition of Ethyl Acetate. *Organometallics* **2017,** *36* (4), 761-766.

115. Nakano, H., Quasidegenerate perturbation theory with multiconfigurational self-consistent-field reference functions. *The Journal of Chemical Physics* **1993,** *99* (10), 7983-7992.

116. Nakano, H., MCSCF reference quasidegenerate perturbation theory with Epstein—Nesbet partitioning. *Chemical Physics Letters* **1993,** *207* (4), 372-378.

117. Golunski, S. E., FINAL ANALYSIS. *Platinum Metals Review* **2007,** *51* (3), 162-162.

118. Maxwell Teague, D.; B. Clougherty, L.; N. Speca, A., *Operation of Platinum-Palladium Catalysts with Leaded Gasoline*. 1975; Vol. 10, p 113-6.

119. Kuo, P. L.; Chen, W. F.; Lin, C. Y., Multichelate-functionalized carbon nanospheres used for immobilizing Pt catalysts for fuel cells. *Journal of Power Sources* **2009,** *194* (1), 234-242.

120. Holme, T.; Zhou, Y.; Pasquarelli, R.; O'Hayre, R., First principles study of doped carbon supports for enhanced platinum catalysts. *Physical Chemistry Chemical Physics* **2010,** *12* (32), 9461-9468.

121. H Einhorn, L., *Treatment of testicular cancer: A new and improved model*. 1990; Vol. 8, p 1777-81.

122. Rosenberg, B.; Vancamp, L.; Trosko, J.; H. Mansour, V., *Platinum Compounds: a New Class of Potent Antitumour Agents*. 1969; Vol. 222, p 385-6.

123. Gerasimovski, V. L., Geochemistry of Rare Earth Elements. *Rare Earth Elements* **1959,** *27*, 27.

124. Goldberg, E. D.; G.O.S, A., Chemistry of Pacific pelagic sediments. *Geochimica et Cosmochimica Acta* **1958,** *13* (2), 153-212.

125. Ronov, A. B.; Yaroshevskiy, A. A.; Migdisov, A. A., CHEMICAL CONSTITUTION OF THE EARTH'S CRUST AND GEOCHEMICAL BALANCE OF THE MAJOR ELEMENTS (PART II). *International Geology Review* **1991,** *33* (11), 1049-1097.

126. Castleman, A. W., From Elements to Clusters: The Periodic Table Revisited. *The Journal of Physical Chemistry Letters* **2011,** *2* (9), 1062-1069.

127. Peppernick, S. J.; Dasitha Gunaratne, K. D.; Castleman, A. W., Towards comprehending the superatomic state of matter. *Chemical Physics Letters* **2010,** *489* (1), 1-11.

128. Peppernick, S. J.; Gunaratne, K. D. D.; Castleman, A. W., Superatom spectroscopy and the electronic state correlation between elements and isoelectronic molecular counterparts. *Proceedings of the National Academy of Sciences* **2010,** *107* (3), 975-980.

129. C Tyo, E.; Nössler, M.; Rabe, S.; L Harmon, C.; Mitric, R.; Bonačić-Koutecký, V.; W Castleman, A., *Exploring similarities in reactivity of superatom species: A combined theoretical and experimental investigation*. 2012; Vol. 14, p 1846-9.

130. Manori Perera, K.; Metz, R., *Photodissociation Spectroscopy and Dissociation Dynamics of TiO+(CO2)*. **2009,** 113, p 6253-6259.

140. Böhme, D. K.; Schwarz, H., *Gas-Phase Catalysis by Atomic and Cluster Metal Ions: The Ultimate Single-Site Catalysts* **2005**, 44, 2336-2354.